Navier-Stokes and Euler Solutions for Lee-Side Flows Over Supersonic Delta Wings

A Correlation With Experiment

S. Naomi McMillin and James L. Thomas
Langley Research Center
Hampton, Virginia

Earll M. Murman
Massachusetts Institute of Technology
Cambridge, Massachusetts

Page intentionally left blank

Contents

Page intentionally left blank

Abstract

An Euler flow solver and a thin-layer Navier-Stokes flow solver have been used to numerically simulate the supersonic lee-side flow fields over delta wings. These lee-side flow fields have been experimentally observed over sharp-leading-edge delta wings through parametric variations in leading-edge sweep, angle of attack, and Mach number. The flow fields over three delta wings with $75°$, $67.5°$, and $60°$ leading-edge sweep were computed over an angle-of-attack range of $4°$ to $20°$ at a Mach number of 2.8. The Euler code and the Navier-Stokes code predict the primary flow structure equally well when the flow is expected to be clearly separated or clearly attached at the leading edge based on the Stanbrook-Squire boundary. The Navier-Stokes code is capable of predicting both the primary and the secondary flow features for the parameter range investigated. For those flow conditions where the Euler code did not predict the correct type of primary flow structure, the Navier-Stokes code illustrated that the flow structure is sensitive to boundary-layer model. In general, the laminar Navier-Stokes solutions agreed better with the experimental data, especially for the lower sweep delta wings. Results from the computational study and a detailed reexamination of the experimental data resulted in a refinement of the flow classifications. This refinement in the flow classification results in the separation bubble with shock flow field as the intermediate flow pattern between separated and attached flows.

Summary

Through previous experimental observation of the lee-side flow of sharp-edged delta wings in supersonic flow, six distinctly different types of flow fields have been identified and classified as a function of angle of attack and Mach number normal to the leading edge. A comparison between the experimental data and computations obtained from an Euler code and a Navier-Stokes code was conducted at a constant Mach number of 2.8. Three leading-edge sweeps, $75°$, $67.5°$, and $60°$, were examined over an angle-of-attack range of $4°$ to $20°$. In the experiment and the computations, span distance was held constant and the Reynolds numbers based on root chord, corresponding to decreasing leading-edge sweep, were 3.7×10^6, 2.4×10^6, and 1.7×10^6, respectively. The Euler code successfully predicts primary flow structures only when the flow conditions normal to the leading edge clearly dictate either the separation or the attachment of the flow at the leading edge based on the Stanbrook-Squire boundary. The Euler code is incapable of predicting secondary flow features. The thin-layer Navier-Stokes computational code successfully predicts the primary and secondary flow structures of the six flow regimes and the effect of varying leading-edge sweep and angle of attack. A comparison of laminar and turbulent Navier-Stokes solutions indicates that the laminar-boundary-layer model is more accurate in predicting the primary and secondary flow features, especially for the lower sweep delta wings, which have lower Reynolds numbers at the trailing edge. In addition, the Navier-Stokes code indicated detailed flow structures not observed in the qualitative experimental data available. The computational study prompted a reexamination of the experimental data such that a refinement of the flow classifications is proposed. Basically, the separation bubble with shock flow field is identified as an intermediate flow pattern between the separated and attached flow regions.

Introduction

The development and experimental validation of advanced aerodynamic computational techniques such as Euler and Navier-Stokes codes will eventually provide aerodynamic design capability heretofore not possible. In the past, aerodynamic design methodology for low supersonic Mach numbers has been limited to a relatively simple flow model. For example, in the 1960's and 1970's, wing designs (ref. 1) for SST or fighter applications were based on solutions to the linearized potential equation and were therefore limited to attached subcritical cross flows. More recent high-lift wing designs (ref. 2) have employed methodology based on solutions of the nonlinear full-potential equations, which can treat mixed subcritical/supercritical attached cross flows and model weak shocks. These designs are still restricted to attached flows because of the irrotational, inviscid assumptions of full-potential theory. Vortex flap wing designs (ref. 3) assume the existence of leading-edge vortices and have employed a methodology based on a combination of linearized potential theory and empirical data. The aerodynamicist prefers not to be limited to a particular type of flow and likes to make optimum use of both attached and separated flows. In order to achieve this, design methodologies and procedures must be based on rather unrestricted aerodynamic computational techniques. Recently reported results (refs. 4–11) indicate that algorithms capable of solving the Euler and Navier-Stokes equations are sufficiently developed and that computer processing speeds have increased enough to begin the necessary calibration process that leads to incorporating Euler and Navier-Stokes solvers into the wing design process.

Several researchers have experimentally investigated and classified the lee-side flow over highly swept wings in supersonic flow. Stanbrook and Squire (ref. 12) classified separated and attached lee-side flow regimes by using the similarity parameters Mach number and angle of attack normal to the leading edge. This work has been extended further by Whitehead et al. (ref. 13), Szodruch and Ganzer (ref. 14), and Miller and Wood (ref. 15). The classification of lee-side flows based on the wind-tunnel experiment reported in reference 15 is presented in figure 1. The flow chart of figure 1(a) classifies the six flow patterns, observed experimentally, as functions of Mach number and angle of attack normal to the leading edge. The hatched lines represent the boundaries between the different flow regions. The central vertical boundary (up to $\alpha_N = 30°$) of figure 1(a) is similar to the classical Stanbrook-Squire boundary between separated and attached flow. The flow types to the left of this boundary are as follows, starting at the bottom of the figure: leading-edge separation bubble with no shock, primary and secondary vortex with no shock, and primary and secondary vortex with shock. The flow types to the right of this central boundary, in the same order, are as follows: shock with no separation, shock-induced separation, and leading-edge separation bubble with shock. Sketches of each flow pattern are presented in figure 1(b). The sketches are based on the vapor-screen photographs obtained in the experimental test.

The purpose of this investigation is to calibrate an existing Navier-Stokes computational code and an existing Euler computational code for sharp-leading-edge delta wing flows at supersonic speeds. The approach is to compare results from these two computational codes with experimental results. The comparisons will be conducted on three delta wings (75°, 67.5°, and 60° leading-edge sweep with span held constant) over an angle-of-attack range of 4° to 20° at a constant Mach number of 2.8. The Reynolds number, based on root chord, varied with leading-edge sweep from 3.7×10^6 for the 75° delta wing to 1.7×10^6 for the 60° delta wing. The effect of the boundary-layer model (laminar or turbulent) on the Navier-Stokes computations will also be examined.

Symbols

c root chord, in.

C_p surface pressure coefficient

F parameter used within the turbulence model in determining the length scales and thus the eddy viscosity

M free-stream Mach number

M_N Mach number normal to the leading edge, $M \cos \Lambda_{LE}(1 + \sin^2 \alpha \tan^2 \Lambda_{LE})^{1/2}$

p_o free-stream total pressure

$p_{o,l}$ local total pressure

r leading-edge radius in the cross-flow plane, in.

Re   Reynolds number

s distance along a ray extending normal from the surface, in.

x longitudinal position from wing apex

y spanwise position from wing centerline

z vertical position from wing upper surface

α angle of attack, deg

α_N angle of attack normal to the leading edge, $\tan^{-1}(\tan \alpha / \cos \Lambda_{LE})$, deg

Δs distance from the surface of the wing to the first grid point, in.

Λ leading-edge sweep, deg

Subscripts:

LE   leading edge of the wing

max   maximum of a function

TE   trailing edge of the wing

Flow structure abbreviations:

CS   cross-flow shock

CV   core of the vortex

FS   feeding sheet of a vortex

R   reattachment of the flow to the surface

S   separation of the flow from the surface

SIS   shock-induced separation

Flow structure subscripts:

LE   localized at leading edge

p   primary

s   secondary

si   shock-induced

sm   smooth

t   tertiary

Experimental Test

The experimental data used extensively throughout this investigation were obtained in a wind-tunnel

experiment (ref. 15) conducted in the NASA Langley Unitary Plan Wind Tunnel (UPWT) on four delta-wing models that varied in leading-edge sweep ($\Lambda = 75°$, $67.5°$, $60°$, and $52.5°$) as shown in figure 2. Each model had a total span of 12 in. and a thickness of 0.3 in. at the trailing edge. The upper surface of each model was flat, and the leading edge was made sharp ($10°$ wedge angle on the lower surface, measured normal to the leading edge). According to the guidelines set forth in reference 16, transition strips composed of No. 60 carborundum grit were sprinkled on the upper surface 0.2 in. behind the model leading edge (measured normal to the leading edge) in an attempt to ensure turbulent boundary-layer flow over the model at attached flow conditions. The four models were each tested at $M = 1.7$, 2.0, 2.4, and 2.8 over an angle-of-attack range of $0°$–$20°$ and at a Reynolds number of 2.0×10^6/ft, which corresponds to a Reynolds number range based on root chord of 3.7×10^6 to 1.3×10^6.

Each model was instrumented with a spanwise row of pressure orifices 1 in. forward of the trailing edge. In addition to the surface pressure data obtained near the trailing edge, three types of flow visualization data were obtained. Vapor-screen photographs provided qualitative information on the flow field above the leeward side of the wing. Oil-flow and tuft photographs provided information on the flow characteristics on the model surface. Based on these results, Miller and Wood (ref. 15) classified the flow into six distinct types, and a chart was developed that defines the flow type as a function of Mach number and angle of attack normal to the leading edge. This chart is shown in figure 1(a).

Computational Study

Computational Algorithms

Navier-Stokes solver. The Navier-Stokes code of reference 4 was selected for this investigation because it had been used previously to predict leeside flows over delta wings for a few selected cases. The computational method used in the Navier-Stokes code has been discussed in detail in references 4 and 17 through 21. The three-dimensional, time-dependent, compressible Navier-Stokes equations are transformed to a generalized coordinate system. The thin-layer approximations are then applied to the equations. The equations are in conservation form and are solved with a finite volume approach. The convective and pressure terms are differenced with the upwind-biased flux-difference splitting approach of Roe (ref. 18), whereas the shear stress and heat-transfer terms are centrally differenced. For the present investigation, the convective and pressure terms are differenced using a third-order interpolation of the primitive variables to the cell interfaces. The shear stress and heat-transfer terms are differenced with second-order accuracy, and the global accuracy is second order. The upwind-biased spatial-differencing scheme is very similar to that in reference 4, except that flux-difference rather than flux-vector splitting is used for the convective and pressure terms. The flux-difference splitting approach includes information about all differing waves by which adjacent cells interact and is demonstrated in reference 20 to be more accurate than the flux-vector splitting approach in the boundary-layer region.

The time-differencing algorithm used in the Navier-Stokes code is a spatially split approximate-factorization method. It is difficult to linearize exactly the residual terms arising with Roe's flux-difference splitting approach, and an approximate linearization is used. The resulting implicit discretization is conservative in time and is, in practice, similar to that used in reference 21, corresponding to a first-order flux-vector splitting linearization in time.

The turbulent-boundary-layer calculations are made with an isotropic, algebraic, two-layer, eddy-viscosity model developed by Baldwin and Lomax (ref. 22). The model includes the modifications incorporated by Degani and Schiff (ref. 23) necessary to ensure that in the presence of vortical flows the viscous length scales are determined by the boundary layer on the body or wing. The model was used by Newsome and Adams (ref. 24) in the accurate prediction of elliptical missile body flows at large angles of attack and yaw. However, the turbulent-boundary-layer model does not directly account for many effects such as compressibility, nonequilibrium, rotation, free-stream turbulence, relaminarization of the boundary layer, or the location of boundary-layer transition.

Euler solver. The Euler code of reference 5 was selected for comparison with the Navier-Stokes code, as it has previously been used to predict lee-side flows over delta wings for a few selected cases. The computational method used in the Euler code has been discussed in detail in several references (see refs. 5, 25, and 26). The full three-dimensional unsteady Euler equations are transformed to a conical coordinate system. A finite volume method is used to discretize the equations in conservative form, and a four-stage Runge-Kutta method is used to integrate pseudo-unsteady equations to achieve steady-state solutions. Boundary conditions enforce tangential flow at the

body surface and free-stream conditions on the outer boundary, which is outside the bow shock.

The Euler equations themselves contain no dissipation, and the centered spatial differences are not dissipative to lowest order. Artificial damping or viscosity is required to damp out high-frequency modes of the discrete equations and to capture shocks. Blended fourth- and second-difference dissipation terms are added to the discretized inviscid equations for these two purposes, respectively.

For a sharp-edged geometry like that considered here, a Kutta condition provides the mechanism for locating the point at which the flow separates from the wing to form a primary vortex. In the calculations, the Kutta condition is enforced implicitly by the artificial damping. Because the separation point is determined by the geometry, its position is insensitive to the magnitude of both physical and numerical viscosity for the Reynolds numbers of interest. The artificial viscosity also provides a mechanism for creating losses. Computations and analyses have shown that the levels of these losses are not sensitive to the levels of damping (refs. 25 and 27).

Computational Test Matrix

The lee-side surface of a flat delta wing is geometrically conical, and experimental data (ref. 28) have shown the lee-side flow to develop conically for the Mach number and angle-of-attack range of this investigation. Three-dimensional Navier-Stokes solutions were obtained for selected cases to computationally investigate the validity of the conical assumption for sharp-leading-edge delta wings in supersonic flow. Based on these results, it was determined that conical solutions would adequately represent the flows being investigated. The assumption of conical flows significantly reduced the required computational resources and made possible the examination of a large number of cases.

In order to calibrate the Navier-Stokes and Euler codes with the existing experimental data, a systematic approach was taken in selecting cases from figure 1(a). This computational test matrix is shown in figure 3. For all cases in the computational matrix, free-stream Mach number was held constant at 2.8, with leading-edge sweep and/or angle of attack varying. This approach yielded 15 cases that covered the 6 flow types of interest.

As discussed above, the models had grit located 0.2 in. behind the leading edge in an attempt to ensure fully turbulent boundary-layer flow over the wind-tunnel model at attached leading-edge flow conditions. However, a question arises as to the state of the boundary layer for the flow separating at the leading edge, reattaching near the centerline, and

flowing outward on the wing under a primary vortex. Thus Navier-Stokes solutions were obtained with both a laminar and a turbulent boundary-layer model for the separated flow cases. Because of the effects of boundary-layer model observed for separated flow, it was decided also to investigate computationally the effect of boundary-layer model on the attached flow cases.

Computational Solutions

Conical Navier-Stokes and conical Euler solutions were obtained at each of the points on the computational test matrix shown in figure 3. Three-dimensional Navier-Stokes solutions were obtained on the 75°, 67.5°, and 60° delta wings at $\alpha = 8°$. Navier-Stokes solutions were obtained with both a laminar- and a turbulent-boundary-layer model. A Navier-Stokes solution with a laminar-boundary-layer model is referred to hereafter as a laminar Navier-Stokes solution. Likewise, a Navier-Stokes solution with a turbulent boundary-layer model is referred to as a turbulent Navier-Stokes solution. A discussion of the turbulence model and various parameters associated with the use of that model is contained in appendix A.

The cross-sectional geometry at the trailing edge of the configuration is used for all the conical solutions. The conical self-similarity assumption implies that this section is extended conically forward to the apex and aft to infinity. The three-dimensional solutions were obtained by modeling the surface of the wind-tunnel models. This approach included modeling the nonconical nature of the lower surface. The Reynolds number is based on root chord and is referred to as the trailing-edge Reynolds number.

Grids. The grids used with the Navier-Stokes code were generated numerically using the code of reference 29, which is based on the elliptic grid generation method of reference 30. Each grid associated with a conical Navier-Stokes solution consisted of 75 radial and 151 circumferential (75×151) points. Figure 4 illustrates a sample grid used in a conical Navier-Stokes solution. This grid is located at the trailing edge of the geometry and is in the y-z plane. The radial grid point stretching distribution was exponential at the body, with a smooth transition to a milder geometric stretching in the outer portion of the grid.

In reference 31, it was determined that the type of grid spacing through the boundary layer could have a significant impact on the Navier-Stokes results. For example, for a turbulent boundary layer, a stretched grid that clustered points near the surface yielded more accurate results than a uniform

4

grid. The opposite trend was found to exist for a laminar boundary layer. Hence, for the purposes of this investigation, both grids are stretched, with the grid for a turbulent Navier-Stokes solution being more stretched than that of a laminar Navier-Stokes solution. Figure 5 illustrates the difference in the two grids. The turbulent-spacing grid for each geometry had a minimum spacing, $\Delta s/c$, of 0.00003 at the wall, where c is the root chord of the wing. This minimum spacing was based on the criterion of having 1–2 points in the viscous sublayer. The laminar-spacing grid had $\Delta s/c = 0.00005$ for the 75° delta wing and $\Delta s/c = 0.0001$ for the 67.5° and 60° delta wings. These values were based on the criterion of having 15–20 points in the boundary layer. Also to be noted from figure 5 is that the leading edge was slightly rounded, with a leading-edge radius of $r/c = 0.00002$. This modification to the geometry allowed a smoother grid about the leading edge to be achieved for use in the Navier-Stokes code. The span of the modified cross section was 99.9 percent of that of the original span.

The three-dimensional grids were generated by stacking y-z planar grids down the length of the wing. Presented in figure 6 is the grid for the 75° delta wing. The grid had 12 x-stations down the length of the wing, as shown in figure 6(a). Figure 6(b) presents the surface geometry at each of the 12 x-stations and illustrates the nonconical nature of the lower surface. A y-z planar grid was generated at each of the x-stations in the same fashion as the conical grids were. The grid spacing used for the conical grid of the 75° delta wing was also used for the trailing-edge planar grid. The grid spacing was scaled appropriately for the planar grids forward of the trailing edge. Each planar grid had 66 points in the radial direction and 151 points in the circumferential direction. Shown in figure 6(c) is an oblique view of the three-dimensional grid.

The same approach was taken in generating the three-dimensional grids for the 67.5° and 60° delta wings. The size of these grids was $12 \times 70 \times 151$ points.

Each of the grids used in obtaining the conical Euler solutions consisted of 128 radial and 128 circumferential (128×128) points. Figure 7 illustrates a sample grid. The Euler grids were generated using a code developed at the Massachusetts Institute of Technology based on the elliptic grid generation method of reference 29, with modifications to enforce conditions on grid aspect ratio rather than normal spacing at the body and outer boundaries.

Convergence characteristics. For the conical solutions obtained by the Navier-Stokes code, a single

array of cross-flow volumes is constructed such that the inflow and outflow planes are scaled by a conical transformation. At each iteration, the inflow conditions are updated with the results of the previous iteration until convergence occurs. The solutions in all cases were impulsively started from free-stream initial conditions. Boundary conditions consisted of reflection conditions in the cross-flow symmetry plane, no-slip adiabatic wall temperature conditions on the body surface, and free-stream conditions on the outer boundary.

The three-dimensional Navier-Stokes solutions were obtained by first attaining conical solutions on the y-z planar grids at the $x/c = 0.1$ and $x/c = 1.0$ stations. These conical solutions were then used to interpolate flow field properties for the other 10 planar grids. This interpolated three-dimensional solution was then used as a first guess in the three-dimensional solution.

Converged laminar and turbulent Navier-Stokes solutions were obtained for the 15 conical cases and the 3 three-dimensional cases by using the Navier-Stokes code and the appropriate grid. However, a converged conical laminar Navier-Stokes solution could not be obtained on the conical laminar-spacing grid for the $\Lambda = 75°$, $\alpha = 4°$, $M = 2.8$ case. This case was repeated on the conical turbulent-spacing grid and a converged laminar Navier-Stokes solution was obtained. Also, a converged conical turbulent Navier-Stokes solution could only be obtained for the $\Lambda = 67.5°$, $\alpha = 20°$, $M = 2.8$ case by reducing a gradient comparison parameter in the minimum-modulus limiter employed on the spatial differencing scheme. A detailed discussion on the minimum-modulus limiter can be found in reference 19.

A typical problem in obtaining the Navier-Stokes solutions was that the residual entered into a limit-cycle oscillation although flow field quantities (e.g., total pressure) and integrated force coefficients (e.g., lift coefficient) had reached an acceptable convergence. This characteristic has been associated with the minimum-modulus limiter used in the spatial differencing scheme (ref. 19). Although not presented here, solutions were also obtained with the flux-vector splitting algorithm with only small differences noted from the solutions presented here using the flux-difference splitting method. This observation indicates that the truncation error levels are small.

In obtaining the conical Euler solutions, calculations were first obtained on coarser grids and then interpolated for use as initial conditions on the 128×128 grids. The solutions were run for 500 iterations on these grids. All cases except the $\Lambda = 67.5°$, $\alpha = 16°$, $M = 2.8$ case converged to an acceptable steady state. The general features and force

5

coefficients for this case appeared satisfactory, but the residual did not reach a steady-state level.

Shown in the following chart are sample run times for the three types of solutions obtained (the times are in minutes on the CRAY Y-MP machine):

Type of solution	Run time, min
Euler	3
Conical Navier-Stokes	20
Three-dimensional Navier-Stokes	240

Experimental and Computational Flow Features

The flow features as observed in the experimental and computational data are discussed in detail here. Examined throughout this section is the $\Lambda = 75°$, $\alpha = 16°$, $M = 2.8$ case. The computational data presented are those of the conical Navier-Stokes solution with a laminar-boundary-layer model for the sample case.

Figure 8 is the vapor-screen photograph for the sample case ($\Lambda = 75°$, $\alpha = 16°$, $M = 2.8$). The flow structure consists of a primary vortex separating at the leading edge, with a cross-flow shock occurring at the top edge of the primary vortex. A secondary vortex is demonstrated to form beneath the primary vortex. These flow structures are clearly labeled in the figure.

Color contour plots of the computational data are presented in figure 9. Figure 9(a) presents the total pressure ratio data ($p_{o,l}/p_o$), and figure 9(b) presents the cross-flow Mach number data. The definition of cross-flow Mach number is the same as total Mach number except the radial component of the flow has been subtracted from each of the velocity components. The radial component of the flow is that which lies along a ray from the apex. The structures observed in the vapor-screen photograph (fig. 8) are also evident and labeled in the color contour data. However, in comparing the color contour data with the vapor-screen photograph it is evident that the total pressure ratio data best represent the vortical structures as they appear in the vapor-screen photograph. The cross-flow Mach number data best represent the cross-flow shock systems as they appear in the vapor-screen photograph. As shown in figure 9, the computational solution predicted the formation of a cross-flow shock between the primary vortex and the feeding sheet of the secondary vortex. This flow structure is not evident in the vapor-screen photograph.

Line contour plots of the total pressure ratio and cross-flow Mach number data are presented in figures 10(a) and (b). The cross-flow velocity vectors are presented in figure 10(c). The flow structures discussed above are also evident in this presentation format. However, in the velocity vector data there is evidence of a tertiary vortex beneath the secondary vortex. This flow structure is not evident in the contour data or the vapor-screen photograph.

Figure 11 is the oil-flow photograph for the sample case ($\Lambda = 75°$, $\alpha = 16°$, $M = 2.8$). Labeled are the separation lines of the secondary and tertiary vortices discussed above. The reattachment lines of these vortices are not clear in the oil-flow photograph. The particle traces of the computational solution at the first grid point above the surface are presented in figure 12. This form of data is regarded as a numerical equivalent to the oil-flow photographs obtained experimentally. The computational solution was obtained on the trailing-edge cross-sectional geometry and was conical. Therefore, the particle trace data were derived by imposing the computational solution at each cross section of a three-dimensional wing. Converging particle traces denote separation lines, whereas diverging particle traces denote reattachment lines. The particle trace data demonstrate not only the separation lines of the secondary and tertiary vortices but also the reattachment lines of those vortices not readily evident in the oil-flow photograph.

Results and Discussion

Comparison of Three-Dimensional and Conical Navier-Stokes Solutions

A comparison of the three-dimensional and conical solutions obtained with the Navier-Stokes code is presented here. The effect of boundary-layer model will also be examined. The three cases examined were the 75°, 67.5°, and 60° delta wings at $\alpha = 8°$ and $M = 2.8$. An extensive discussion of the 75° delta wing data is presented here. Appendix B contains the computational data for the 67.5° and 60° delta wings. The computational data are presented here in the form of total pressure ratio ($p_{o,l}/p_o$) contours, particle trace data, and surface pressure data.

Presented in figure 13 are the data from the three-dimensional laminar Navier-Stokes solution for the 75° delta wing at $\alpha = 8°$. Figure 13(a) presents the total pressure ratio contour data of the solution at $x/c = 0.2$, 0.5, and 1.0, whereas figure 13(b) presents the particle trace data at the first grid point above the surface. Figure 13(c) presents the surface pressure data at $x/c = 0.2$, 0.5, and 1.0. The y and z coordinates at each station have been nondimensionalized by the local semispan (y_{LE}).

The data for $x/c = 1.0$ (the trailing edge) of figure 13(a) illustrate a flow that separates at the leading edge to form a primary vortex, with a secondary vortex occurring beneath the primary vortex. Another vortex is seen to occur inboard of this secondary vortex and is referred to here as a second secondary vortex, as it has the same sense of vorticity as the first secondary vortex. A tertiary vortex as defined in the literature would have a rotation opposite to that of the secondary vortex. The particle trace data illustrate not only these two secondary separations but also a tertiary vortex separating beneath each of the secondary vortices. The tertiary vortices are not evident in the contour data of figure 13(a) but are evident in velocity vectors not presented here. The data of figures 13(a) and (b) illustrate that the secondary and tertiary vortices strengthen as the trailing edge is approached (corresponding to a increase in local Reynolds number), such that the number of separations increase. However, the primary vortex is seen to grow essentially conically from the apex to the trailing edge.

The surface pressure data of figure 13(c) show that surface pressure distribution on the lower surface is markedly different for each of the three x-stations presented; this corresponds to the different geometry at these x-stations. However, the upper surface distributions do not vary greatly between the x-stations. The sharp decrease in pressure evident on the upper surface occurs over an interval of $y/y_{LE} = 0.4$–0.5. Note in the particle trace data of figure 13(b) that this pressure decrease falls between the primary reattachment line ($y/y_{LE} = 0.35$) and the first secondary separation line ($y/y_{LE} = 0.55$). Thus, the sharp decrease in pressure is due to the edge of the vortex. These data illustrate that the primary vortex moves slightly outboard as the trailing edge is approached. The surface pressure data also reflect the increase in the number and strength of secondary and tertiary vortices as the trailing edge is approached.

For the above solution, as the trailing edge is approached the local Reynolds number (based on chord length) increases. Presented in figure 14 are conical laminar Navier-Stokes solutions at Reynolds numbers of 0.5×10^6, 1.0×10^6, and 3.73×10^6, which roughly correspond in magnitude to the local Reynolds numbers at $x/c = 0.2$, 0.5, and 1.0 for the three-dimensional laminar Navier-Stokes solution. The contour and particle trace data of figures 14(a) and (b) show an increase in the extent of secondary and tertiary separation with an increase in Reynolds number, as observed in the three-dimensional data. The data of figures 14(a) and (b) also show that the general size of the primary vortex

is essentially unchanged with an increase of Reynolds number. The surface pressure data of figure 14(c) illustrate that the primary vortex moves slightly outboard with an increase in Reynolds number.

Presented in figure 15 are the data from the three-dimensional turbulent Navier-Stokes solution for the 75° delta wing at $\alpha = 8°$. The data for $x/c = 1.0$ (the trailing edge) of figure 15(a) illustrate a flow that separates at the leading edge to form a primary vortex, with one secondary vortex occurring beneath the primary vortex. The contour definition of the secondary vortex becomes more distinct as the trailing edge is approached, suggesting that the secondary vortex gains strength as the trailing edge is approached. The contour data and the particle trace data of figures 15(a) and (b) illustrate the near conical growth of the primary vortex down the length of the wing. The surface pressure data of figure 15(c) demonstrate that the edge of the primary vortex does move slightly outboard as the trailing edge is approached.

Presented in figure 16 are the data from conical turbulent Navier-Stokes solutions obtained at Reynolds numbers of 0.5×10^6, 1.0×10^6, and 3.73×10^6 for the 75° delta wing at $\alpha = 8°$. Again, these Reynolds numbers roughly correspond in magnitude to the local Reynolds numbers at $x/c = 0.2$, 0.5, and 1.0 of the corresponding three-dimensional solution. The trends of the vortical structures with increasing local Reynolds number observed in the corresponding three-dimensional solution are also observed in these solutions, as seen in figure 16.

Presented in appendix B are the computational data from the three-dimensional Navier-Stokes solutions and corresponding conical solutions for the 67.5° and 60° delta wings at $\alpha = 8°$. These data reflect the same effects from modeling the three-dimensional wing as were observed on the 75° delta wing. The flow structures predicted by the three-dimensional solutions are essentially conical. The minimal effects that do exist appear to be correlated with local Reynolds number on the basis of comparisons with conical solutions at varying Reynolds numbers. Therefore, conical solutions were used in the parametric comparisons with the experiment below.

Conical Navier-Stokes Results and Comparisons With Experiment

The comparison of laminar and turbulent Navier-Stokes solutions with experimental data is presented here. All Navier-Stokes solutions presented in this section are conical. Portions of the computational data are presented in the form of total pressure ratio ($p_{o,l}/p_o$) contours, which best define vortical structures as they appear in vapor-screen photographs.

Likewise, cross-flow Mach number contours are presented, as these contours best define cross-flow shock systems as they appear in vapor-screen photographs. Yet another form of computational data presentation for the Navier-Stokes solutions is that of particle traces at the first grid point above the surface. This form of data is regarded as a numerical equivalent to the oil-flow photographs obtained experimentally. Surface pressure data are also presented.

75° delta wing. Presented in figure 17 are the vapor-screen photographs for the 75° delta wing at $\alpha = 4°$, $8°$, $12°$, $16°$, and $20°$. This wing has a subsonic leading-edge condition at $M = 2.8$. By examination of these photographs, the flow over the 75° delta wing at $M = 2.8$ is seen to be separated at the leading edge throughout the angle-of-attack range. The discussion in reference 15 points out a transition with angle of attack from a leading-edge bubble at $\alpha = 4°$ to a classical vortex (primary vortex with secondary vortex) at $\alpha = 8°$ to a vortex with shock at $\alpha = 16°$. The corresponding computational data from the laminar and turbulent Navier-Stokes solutions are also presented in the form of color contour plots. Figure 17(a) presents the total pressure ratio contour plots, and figure 17(b) presents the cross-flow Mach number contour plots. Figure 17(c) defines the color bar scales for the color contour data of the 75° delta wing. Note that each angle of attack has a different color bar scale for the cross-flow Mach number data.

The data of figure 17 demonstrate that the wall boundary-layer model (laminar or turbulent) does not significantly influence the primary vortex flow field. At the low angles of attack ($\alpha = 4°$ and $8°$), the boundary-layer model affects the extent of secondary separation occurring beneath the primary vortex. However, at the higher angles of attack, the boundary-layer model has a minimal effect on the secondary separation. This trend is also observed in the surface pressure data of figure 18, which presents the experimental and computational surface pressure distributions for each of the 15 cases. The data for the 75° delta wing demonstrate that as angle of attack increases, the differences in the surface pressure distribution due to boundary-layer model lessen in the region of secondary separation.

Cross-flow shock systems not identified in reference 15 are evident in the cross-flow Mach number data of figure 17(b). For example, the Navier-Stokes solutions predict weak cross-flow shock systems atop the primary vortex at $\alpha = 4°$ and $8°$. The changing gray levels atop the primary vortex in the vapor-screen photograph correspond very well to the computed cross-flow shock structure. The cross-flow

shocks at $\alpha = 4°$ and $8°$ are sufficiently weak that they are not evident in the total pressure ratio contour data of figure 17(a). The data of figure 17(b) also show a cross-flow shock forming between the primary vortex and its counterpart across the longitudinal plane of symmetry at $\alpha = 16°$ and $20°$. This flow structure, although not identified in reference 15, is clearly evident in the corresponding vapor-screen photograph and has been observed experimentally by Szodruch (ref. 32).

As defined in reference 15, a separation bubble is a structure that contains its entire rotational flow within its boundaries and exhibits no secondary separation. At $\alpha = 4°$, the computational data that lie within the separation bubble region, agree with this definition in that the solution predicts a narrow vortex whose core lies close to the surface of the wing such that the reattachment line corresponds to the inboard termination of the vortex. However, the Navier-Stokes solution also predicts the formation of secondary and tertiary separations occurring beneath the primary vortex. As stated above, the extent of this secondary separation is dependent on the boundary-layer model, as is evident in the $\Lambda = 75°$, $\alpha = 4°$, $M = 2.8$ data of figures 17–18.

Figure 19 is a more extensive presentation of the computational and experimental data for the $\Lambda = 75°$, $\alpha = 8°$, $M = 2.8$ case. Line contour plots of total pressure ratio for both the laminar and the turbulent Navier-Stokes solutions are presented underneath the vapor-screen photograph. Particle trace data are presented for both the laminar and the turbulent Navier-Stokes solutions beneath the oil-flow photograph. The experimental and computational surface pressure distributions are presented on the right of the figure.

As stated above, the total pressure ratio contour plots of figure 19 illustrate that the boundary-layer model influences the extent of separation occurring beneath the primary vortex for this case. The contour data of figure 19 illustrate that the laminar Navier-Stokes solution predicts the formation of two secondary vortices beneath the primary vortex. The separation lines for each of these vortices are also evident in the particle trace data for the laminar Navier-Stokes solution. The particle trace data also show evidence of a tertiary vortex beneath each of the secondary vortices. These tertiary vortices are not evident in the contour data of figure 19. This system of secondary and tertiary vortices is seen in a close-up view of the most inboard secondary vortex from the laminar Navier-Stokes solution, as illustrated in the data of figure 20. In contrast, as seen in figure 19, the turbulent Navier-Stokes solution has less separation with just one secondary vortex occurring

because the turbulent flow beneath the primary vortex is more resistant to separation. Thus the turbulent Navier-Stokes solution appears to agree better with the vapor-screen photograph. The surface pressure data also show that the turbulent Navier-Stokes solution is in better agreement with experiment than the laminar Navier-Stokes solution.

The explanation for this observation can be seen from an examination of the oil-flow photograph in figure 19. The oil-flow pattern undergoes a change at the midpoint of the wing. The oil-flow pattern ahead of this point agrees well with the particle trace data of the laminar Navier-Stokes solution, whereas the oil-flow pattern aft of this point agrees well with the particle trace data of the turbulent Navier-Stokes solution. Thus it is conjectured that a transition in boundary-layer state occurred for this case at roughly a Reynolds number of 2×10^6. Since the vapor-screen photograph and surface pressure data were obtained near the trailing edge where a turbulent boundary layer apparently exists, the turbulent Navier-Stokes solution would be expected to agree better with the experimental data.

Contained in figure 21 is an extensive presentation of data for $\Lambda = 75°$, $\alpha = 16°$, and $M = 2.8$. The similarity in contour plots and surface pressure distributions for the laminar and turbulent Navier-Stokes solutions indicates that boundary-layer model has little influence on the extent of separation beneath the primary vortex for the high angles of attack. The contour data of figure 21 show the flow structure to be a cross-flow shock atop a primary vortex, with a secondary vortex occurring beneath the primary vortex. The particle trace data illustrate the secondary separation as well as a tertiary separation occurring beneath the secondary vortex. The tertiary vortex is not evident in the contour data of figure 21. However, the tertiary vortex is evident upon closer scrutiny of the contour data and velocity vectors (not presented here). The separation lines for both the secondary and the tertiary vortices are evident in the particle trace data, which agree well with the oil-flow photograph. However, the tertiary vortex is not evident in the vapor-screen photograph. Also not evident in the vapor-screen photograph is the formation of a shock between the primary and secondary vortices as seen most noticeably in the line contour plots of figure 21. The present vapor-screen flow-visualization technique is apparently not sensitive enough to detect either of these two detailed flow structures. The surface pressure data agree well with experiment, although *the computational minimum pressure coefficient is slightly lower than that observed experimentally.*

67.5° delta wing. Presented in figure 17 are the vapor-screen photographs for the 67.5° delta wing at $\alpha = 4°$, 8°, 12°, 16°, and 20°. Note that the 67.5° delta wing at $M = 2.8$ has a supersonic leading-edge condition. The flow classifications as given in reference 15 would indicate a leading-edge separation bubble with shock at $\alpha \geq 8°$. At $\alpha = 4°$ the flow is attached with a cross-flow shock occurring inboard of the leading edge. Figure 22 also contains color contour data from the laminar and turbulent Navier-Stokes solutions for the 67.5° delta wing. The computational data of figure 22 demonstrate that for $\alpha \leq 12°$ boundary-layer model has an influence on the primary flow structure. The laminar Navier-Stokes solutions predict a separation bubble. The turbulent Navier-Stokes solutions predict attached flow at the leading edge with a cross-flow shock occurring inboard; a shock-induced separation bubble results at $\alpha = 8°$ and 12°. The different flow structures due to boundary-layer model yield different pressure distributions, as illustrated in the 67.5° delta wing data of figure 18.

The surface pressure data for the $\Lambda = 67.5°$, $\alpha = 4°$, $M = 2.8$ case illustrate that the turbulent Navier-Stokes solution is in better agreement with the experimental data. The contour data of figure 22 also demonstrate that the turbulent Navier-Stokes solution is in better agreement with the vapor-screen photograph. The vapor-screen photograph for this angle of attack shows what appear to be a series of streamwise vortices that have been associated with boundary-layer transition on bodies at low angles of attack as noted by Peake and Tobak (ref. 33). Thus, it is proposed that the boundary layer is turbulent at the trailing edge for this case. A corresponding transitional Reynolds number would be about 2.4×10^6.

In contrast to the $\alpha = 4°$ case, the data for $\alpha = 8°$ and 12° demonstrate that the laminar Navier-Stokes solution is in better agreement with the vapor-screen photograph, as seen in figure 22. A more extensive presentation of the data for the $\Lambda = 67.5°$, $\alpha = 8°$, $M = 2.8$ case is contained in figure 23. The cross-flow Mach number contour data from the laminar Navier-Stokes solution demonstrate a thin primary vortex whose core lies close to the surface of the wing (i.e., a leading-edge separation bubble) with a cross-flow shock atop the primary vortex. The corresponding particle trace data illustrate not only these features but also a secondary separation occurring beneath the primary vortex. This secondary flow structure is a weak structure not evident in either the contour data as presented here or the vapor-screen photograph and is only evident in the computational data

9

upon close examination of the cross-flow velocity vectors (not presented here).

In contrast, the turbulent Navier-Stokes solution data of figure 23 demonstrate an attached flow at the leading edge with shock-induced separation occurring inboard. The particle trace data for the turbulent Navier-Stokes solution also demonstrate a small separation bubble occurring just inboard of the leading edge, which is not evident in the contour data. This type of flow structure was observed by Seshadri and Narayan (ref. 34) for shock-induced separated flows.

The contour data of the laminar Navier-Stokes solution agree better with the vapor-screen photograph than do the contour data of the turbulent Navier-Stokes solution. Because the oil-flow pattern from the oil-flow photograph is indiscernible, a comparison with the particle trace data is difficult. However, neither of the computed surface pressure distributions agree well with the experimental data points. The experimental surface pressure data exhibit a constant pressure outboard of two-thirds of the semispan and, in this respect, the laminar Navier-Stokes solution is in better agreement with the experimental data.

The $\Lambda = 67.5°$, $\alpha = 8°$, $M = 2.8$ case has a lower leading-edge sweep than that of the $\Lambda = 75°$, $\alpha = 8°$, $M = 2.8$ case, where a boundary-layer transition is conjectured to occur at an approximate Reynolds number of 2.0×10^6. The trailing-edge Reynolds number for the 67.5° delta wing was 2.4×10^6. Both sets of data are of separated flow types. Other researchers (ref. 35) have noted that a decrease in leading-edge sweep increases the transitional Reynolds number. Therefore, it is conjectured that a complete transition from a laminar boundary layer to a turbulent boundary layer never occurred on the 67.5° wing at $\alpha = 8°$; this would account for the discrepancy between the computed and experimental data.

From the data of figure 22, it can be seen that boundary-layer model does not influence the formation of primary flow features and has a minimal influence on the secondary flow features at high angles of attack ($\alpha \geq 16°$). A more extensive presentation for the $\Lambda = 67.5°$, $\alpha = 16°$, $M = 2.8$ case is contained in figure 24. The contour data for both solutions indicate that the flow structure is that of a narrow primary vortex separating at the leading edge with the core of the vortex lying close to the wing. A cross-flow shock is seen to occur atop the primary vortex, apparently inducing a small vortical structure inboard of the primary vortex. This structure is also evident at $\alpha = 12°$ as shown in figure 22. The flow structures discussed above are evident in the particle trace data. The particle trace data also indicate secondary separation occurring be-

neath the primary vortex. The secondary vortex for the laminar Navier-Stokes solution is seen to reattach very close to the leading edge, whereas the turbulent Navier-Stokes solution predicts a smaller secondary vortex as expected. The shock-induced vortical flow and secondary vortical flow are not evident in the vapor-screen photograph. Because the oil-flow patterns from the photograph are indiscernible, a comparison with the particle trace data is difficult.

The surface pressure data of figure 24 show that both solutions agree well with the experimental distribution. However, the computational pressure coefficients are slightly lower than the experimental data.

In contrast to the trends observed for the 75° delta wing, the 67.5° delta wing data show an influence of boundary-layer model on the prediction of the primary flow structure at low angles of attack ($\alpha \leq 12°$). The turbulent-boundary-layer model allows the flow to remain attached at the leading edge. However, the laminar solution cannot negotiate the expansion of the flow at the leading edge without a separation occurring at the leading edge. The result is a thin separation bubble.

In examining the laminar Navier-Stokes solutions of figure 22, it is also observed that the size of the separation bubble is related to the effect boundary-layer model has on the prediction of primary flow structure. Recall from the discussion on the 75° delta wing that a separation bubble as encountered here is a primary vortex whose core lies close to the surface. At $\alpha \geq 16°$ the vortex core of the separation bubble is apparently large enough that it shields the shock atop the vortex from any interaction with the boundary layer. Thus, there is only a vortex/boundary layer interaction occurring that appears to be insensitive to boundary-layer model. The high-angle-of-attack cases for the 75° delta wing, which also consisted of large primary vortices, were also insensitive to boundary-layer model. However, at $\alpha \leq 12°$ on the 67.5° delta wing the vortex is extremely thin, and the shock atop the vortex is apparently no longer shielded from the boundary layer. It is speculated that an interaction of the shock with the boundary layer and vortex results. This type of interaction appears to be sensitive to boundary-layer model. In addition to the other known deficiencies, the turbulent-boundary-layer model may be incapable of modeling this type of interaction because of nonequilibrium effects.

60° delta wing. Presented in figure 25 are the vapor-screen photographs for the 60° delta wing at $\alpha = 4°$, $8°$, $12°$, $16°$, and $20°$. Note that the 60° delta wing at $M = 2.8$ has a supersonic leading-edge condition. The flow classifications as

10

given in reference 15 would indicate that the flow undergoes a transition as the angle of attack increases from an attached flow with shock to a shock-induced separated flow to a separation bubble with shock. Figure 25 also contains color contour data from the laminar and turbulent Navier-Stokes solutions of the 60° delta wing. The computational data of figure 25 illustrate that for $\alpha \leq 12°$ boundary-layer model does not influence the overall prediction of attached flow at the leading edge with a cross-flow shock occurring inboard. However, in the region of the cross-flow shock, boundary-layer model influences the cross-flow separation for $\alpha = 8°$ and 12°. The separation that occurs at $\alpha = 4°$ is very weak, which is evident in the similarity of the contour plots of figure 25 and the surface pressure distributions for the laminar and turbulent Navier-Stokes solutions as seen in the 60° delta wing data of figure 18.

In contrast, the surface pressure distributions for the laminar and turbulent Navier-Stokes solutions for $\alpha = 8°$ and 12° are significantly different in the region of cross-flow separation. A more extensive data presentation for the $\Lambda = 60°$, $\alpha = 8°$, $M = 2.8$ case is contained in figure 26. The cross-flow Mach number contour data for the laminar Navier-Stokes solution indicate a smooth separation from the surface of the wing to form a very thin primary vortex whose core lies close to the surface of the wing. The vortex arises from separation that occurs outboard of the cross-flow shock. In contrast, the turbulent Navier-Stokes solution does not predict a smooth separation, as the turbulent-boundary-layer flow is more resistant to separation. The turbulent Navier-Stokes solution instead predicts a separation occurring directly under or inboard of the cross-flow shock. The shape of the cross-flow shock as it impinges on the surface of the wing is different for the two types of cross-flow separation. The laminar Navier-Stokes solution predicts that the shock will bend toward the centerline to come to rest on the top edge of the primary vortex, as is more readily evident in the cross-flow Mach number data of figure 25(b). However, the turbulent Navier-Stokes solution predicts that the shock will sweep back toward the leading edge to impinge on the surface near the point of separation.

These different types of cross-flow separation also produce different pressure distributions in the region of cross-flow separation, with the laminar distribution in slightly better agreement with the experimental data points. A comparison of the contour data of figure 26 and the vapor-screen photograph is not so decisive because of the very small nature of the cross-flow separation. As observed in the 75° delta wing data, the vapor-screen technique appears to be insensitive to detecting small-scale detailed flow features. However, the cross-flow shock in the vapor-screen photograph does appear to bend back toward the centerline and thus is in better agreement with the laminar Navier-Stokes solution.

The different types of cross-flow separation illustrated in the contour data of figure 26 are also evident in the particle trace data. A secondary separation underneath the thin primary vortex is also evident in the particle trace data of the laminar Navier-Stokes solution. The data also demonstrate a small separation occurring inboard of the leading edge, as was evident for the turbulent Navier-Stokes solution of the $\Lambda = 67.5°$, $\alpha = 8°$, $M = 2.8$ case (fig. 23). Although the quality of the oil flow makes the comparison difficult, the laminar Navier-Stokes solution appears to be in better agreement.

In contrast to the trends observed for the 75° and 67.5° delta wings, the data of figure 25 indicate that boundary-layer model does influence the formation of the primary flow structure for the 60° delta wing at the high angles of attack ($\alpha \geq 16°$). A more extensive presentation for the $\Lambda = 60°$, $\alpha = 16°$, $M = 2.8$ case is in figure 27. A detailed inspection of the contour data of figure 27 demonstrates that the laminar Navier-Stokes solution predicts the formation of a leading-edge separation bubble (i.e., a thin primary vortex whose core lies close to the surface of the wing). A cross-flow shock occurs atop the inboard edge of the separation bubble. The laminar Navier-Stokes solution agrees well with the vapor-screen photograph and the oil-flow pattern over the forward portion of the wing. The particle trace data from the laminar Navier-Stokes solution also reflect the formation of a small weak secondary separation (beneath the primary vortex) which is not evident in the contour data or the vapor-screen photograph. In contrast, the turbulent Navier-Stokes solution predicts attached flow at the leading edge with shock-induced separation occurring inboard. The particle trace data of the turbulent Navier-Stokes solution also show the formation of a small weak secondary separation. The contour and particle trace data of the turbulent data do not correspond well to the vapor-screen and oil-flow photographs.

The different flow structures corresponding to a change in boundary-layer model for $\alpha = 16°$ yield different surface pressure distributions, as seen in figure 27. Neither distribution agrees completely with the experimental data points. However, the laminar Navier-Stokes solution is in better agreement with the experimental data in that it predicts that the pressure distribution is nearly constant approaching the leading edge.

As seen in figure 18, the data for each of the three wings exhibit an increment between the

laminar Navier-Stokes solution and experimental surface pressure distributions at the high angles of attack ($\alpha \geq 16°$). This increment is seen to increase as angle of attack is increased. In fact, the increment is seen to increase with decreasing leading-edge sweep. Although grid refinement was not performed, the grid is probably fine enough that the noted increment between the experimental and computational data is not a function of grid size, especially since the flow structures associated with the lower sweep wings are closer to the surface of the geometry where the grid is highly clustered. The noted trends in this increment between the experimental and computational surface pressure distributions are also observed in the Euler computations of figure 28. The computational and experimental leeward pressures on the centerline are in good agreement and an error in angle of attack is therefore unlikely. This discrepancy is unresolved at the present time.

The observation that boundary-layer model influences the formation of the primary flow structure for the 60° delta wing at high angles of attack ($\alpha \geq 16°$) also applies at low angles of attack ($\alpha \leq 12°$) on the 67.5° delta wing. The size and the location of the leading-edge vortex for these two sets of data are of the same order of magnitude and could be expected to have the same sensitivity to boundary-layer model.

As noted in figure 27, the laminar Navier-Stokes solution agrees better with the experimental data for the 60° wing at $\alpha = 16°$. The trailing-edge Reynolds number for the 60° delta wing was 1.7×10^6. This wing has a lower leading-edge sweep than that of the $\Lambda = 75°$, $\alpha = 8°$, $M = 2.8$ case, a separated flow case, where a boundary-layer transition is conjectured to occur at an approximate Reynolds number of 2.0×10^6. As other researchers (ref. 35) have noted that a decrease in leading-edge sweep increases the transitional Reynolds number, it is possible that a transition from a laminar boundary layer to a turbulent boundary layer never occurred on the 60° delta wing with leading-edge separated flow ($\alpha \geq 16°$). Therefore, it is speculated that the transition strip is ineffective in promoting boundary transition for the separated flow cases examined in this investigation. The boundary-layer transition observed to occur for the $\Lambda = 75°$, $\alpha = 8°$, $M = 2.8$ case is a natural boundary-layer transition since the flow separates at the leading edge and reattaches inboard of the transition strip.

However, for the attached flow, the flow does encounter the transition strip, which was applied on the models in an attempt to force a transition from a laminar boundary layer to a turbulent boundary layer. Recall that the $\Lambda = 67.5°$, $\alpha = 4°$, $M = 2.8$ case, an attached flow case, had a better agreement between the turbulent Navier-Stokes solution and the experimental data. The transitional Reynolds number for the 60° delta wing at $\alpha = 4°$ could be expected to be greater than that of the 67.5° delta wing at $\alpha = 4°$. Also, the transitional Reynolds number for the 60° delta wing could be expected to increase as angle of attack increases, since it has been observed by Stallings and Lamb (ref. 36) that increasing angle of attack results in an increase in transitional Reynolds number for attached flow. Since the 60° delta wing had a lower trailing-edge Reynolds number than the 67.5° delta wing, it is possible that a complete transition from laminar to turbulent flow did not exist. Thus, it is speculated that the transition strip is ineffective in forcing a complete transition in boundary-layer state for those attached flow cases examined in this investigation.

Conical Euler Results and Comparisons With Experiment

In order to determine the ability of the Euler code to predict the six flow regions of interest, a comparison of the conical Euler solutions with the Navier-Stokes solutions and with the experimental data is presented here. All solutions presented in this section are conical solutions. The laminar Navier-Stokes solutions from the Navier-Stokes code were selected for comparison here since these solutions had, in general, a better agreement with the experimental data over the computational test matrix. The computational data are presented in the same fashion as in the previous section. The particle trace data from the Euler solutions are not presented since the particle traces represent the particle trajectories in the inviscid portion of the flow and do not have any relation to the oil flows measured experimentally.

75° delta wing. Presented in figure 29 are the vapor-screen photographs and color contour data from the laminar Navier-Stokes and Euler solutions for the 75° delta wing over the angle-of-attack range. The Euler solutions predict the same type of primary flow structure as the laminar Navier-Stokes solutions (i.e., flow separates at the leading edge to form a primary vortex). Also, the Euler solutions predict a cross-flow shock system above the primary vortex over the angle-of-attack range. The shock system is similar to, but somewhat stronger than, that of the laminar Navier-Stokes solutions.

The surface pressure data for the 75° delta wing of figure 28 illustrate that the Euler solutions overpredicted the expansion due to the primary vortex at all angles of attack. The data for the 75° delta wing at $\alpha \leq 8°$ show that the expansion in the Euler surface pressure due to the primary vortex

occurs outboard of the corresponding expansion for the laminar Navier-Stokes solutions. This observation corresponds to the Euler prediction of a smaller primary vortex in the spanwise direction and is consistent with the trends in Reynolds number predicted with the laminar Navier-Stokes solution. However, at the higher angles of attack the expansion due to the primary vortex occurs at the same location in the Euler and laminar Navier-Stokes solutions. This observation that the size of the primary vortex is similar for the two computational codes at $\alpha \geq 12°$ is also evident in the contour data of figure 29. The contour data of figure 29 also indicate that the Euler solutions predict a larger total pressure loss for the primary vortex.

In contrast to its ability to predict the primary vortex, the contour data of figure 29 demonstrate that the Euler code is incapable of predicting the formation of any secondary separation beneath the primary vortex. In fact, for $\alpha \geq 12°$, the Euler solutions predict that a cross-flow shock will form underneath the core of the primary vortex and extend to the surface of the wing. This cross-flow shock is evident in the surface pressure distributions for these cases in the 75° delta wing data of figure 28. The laminar Navier-Stokes solutions also predicted the formation of a cross-flow shock that extends from beneath the primary vortex core to the feeding sheet of the secondary vortex.

67.5° delta wing. Presented in figure 30 are the vapor-screen photographs and color contour data from the conical laminar Navier-Stokes and Euler solutions for the 67.5° delta wing over the angle-of-attack range. In examining the Euler solution for $\alpha = 4°$, the turbulent Navier-Stokes solution should be used since it was shown to be in better agreement with the experimental data than the laminar Navier-Stokes solution. Figure 31 presents the cross-flow Mach number contour data and the surface pressure distributions for the Euler and turbulent Navier-Stokes solutions for the 67.5° delta wing at $\alpha = 4°$. Both codes predict attached flow at the leading edge, with a cross-flow shock occurring inboard. The location of the cross-flow shock as judged from the cross-flow Mach number contour data is the same for both solutions. However, the Euler solutions predict a stronger cross-flow shock, as is evident in the surface pressure data.

As evident in figure 30, the Euler solution for $\alpha = 8°$ case predicts attached flow at the leading edge, with a cross-flow shock occurring inboard. In contrast, the laminar Navier-Stokes solution predicts a separation bubble with shock flow type. The laminar Navier-Stokes solution is in better agreement

with the vapor-screen photograph and the surface pressure data.

At the higher angles of attack, $\alpha \geq 12°$, the data of figure 30 show that the Euler solutions predict the same type of primary flow structure as that predicted by the laminar Navier-Stokes solutions (i.e., separation bubble with shock). However, the Euler solutions do not predict any secondary separation underneath the narrow primary vortex as is evident in the laminar Navier-Stokes solutions (see fig. 24). The size of the primary vortex appears to be similar for the two solutions, as is also evident in the surface pressure data of figure 28. However, the Euler code overestimates the expansion in surface pressure due to the primary vortex, as was found in the data for the 75° delta wing. The overestimation of the expansion in surface pressure due to the primary vortex is found to decrease with increasing angle of attack for both sets of data.

The data of figure 30 for $\alpha \geq 12°$ illustrate that the Euler solutions predict a slightly stronger cross-flow shock atop the primary vortex than the laminar Navier-Stokes solutions. The laminar Navier-Stokes solutions for $\alpha = 12°$ and 16° predicted the formation of a vortical structure inboard of the primary vortex. The Euler solutions predicted a weak vortical structure for $\alpha = 16°$ but none for $\alpha = 12°$.

60° delta wing. Shown in figure 32 are the vapor-screen photographs and color contour data from the conical laminar Navier-Stokes and Euler solutions for the 60° delta wing over the angle-of-attack range. For $\alpha \leq 12°$, the contour data of figure 32 show that the Euler solutions predict an attached flow condition as is predicted by the laminar Navier-Stokes solutions. However, the laminar Navier-Stokes solutions also predict a smooth separation from the surface of the wing to form a thin primary vortex with a cross-flow shock occurring atop the primary vortex. The Euler solutions predict a cross-flow shock occurring inboard of the leading edge and, as expected, no shock-induced separation. The 60° delta wing data of figure 32 show that the Euler and laminar Navier-Stokes surface pressure distributions agree well except in the region of the cross-flow shock. The laminar Navier-Stokes solutions are in better agreement with the vapor-screen photographs and the experimental surface pressure data.

For the higher angles of attack, $\alpha \geq 16°$, the data of figure 32 show that the laminar Navier-Stokes solutions agree well with the vapor-screen photographs in predicting a separation bubble with shock. The Euler solutions predict the occurrance at the leading edge of a small separated flow, which is barely

discernible in the total pressure ratio contour data of figure 32(a). This separation is clearly evident in the cross-flow velocity vectors for the Euler solutions (not presented here). The Euler solution then predicts attached flow from the reattachment of this very small separation to a cross-flow shock occurring inboard. For $\alpha = 20°$ the Euler solution also predicts a shock-induced vortex occurring inboard of the cross-flow shock. The difference in the flow structures between the laminar Navier-Stokes and Euler solutions is evident in the surface pressure data for the 60° delta wing (fig. 28).

Summary of Computational Results

This section provides a summary of the ability of the Navier-Stokes code and the Euler code to predict the flow patterns observed experimentally over the lee side of delta wings at supersonic speeds. Based on these results, a discussion of the appropriateness of when to use either code is given.

Summary of Navier-Stokes results. The results of the comparisons in a previous section between the conical laminar and turbulent Navier-Stokes solutions and the experimental data are summarized in figure 33 and are discussed below. Figure 33(a) presents the summary of the effect of boundary-layer model on the prediction of primary and secondary flow structures. The definition of primary flow structure corresponds to the flow at the leading edge being either separated or attached. Figure 33(b) presents the summary of the comparison with experimental data.

Figure 33(a) illustrates that boundary-layer model had an influence on the type of primary flow structure predicted only when a thin leading-edge separation bubble was experimentally observed. These points are represented by the solid symbols in figure 33(a). The turbulent flow remained attached as the flow turned around the leading edge. The laminar flow could not negotiate the turn at the leading edge and thus separated. It is speculated that the extremely thin separation bubble caused an interaction to occur between the shock, the separation bubble, and the boundary layer. This interaction is apparently sensitive to boundary-layer model.

The open and partially shaded symbols in figure 33(a) are those cases where the boundary-layer model had no influence on the type of primary flow structure predicted. Note that these cases are not in a region where the flow is transitioning from separated to attached flow at the leading edge. At high angles of attack, the boundary-layer model had a minimal influence on the prediction of secondary separation (open symbols). At low to moderate angles of attack, boundary-layer model did have an influence on secondary separation (partially shaded symbols). For the separated flow cases, boundary-layer model influenced the extent of secondary separation. For the attached flow cases, boundary-layer model influenced the type of cross-flow separation.

The flow chart of figure 33(b) illustrates that with increasing M_N the laminar Navier-Stokes solutions agreed better with the experimental data. This observation is speculated to be a reflection of decreasing trailing-edge Reynolds number with decreasing leading-edge sweep. For example, a natural transition in boundary-layer state (i.e., from laminar flow to turbulent flow) is conjectured to occur for the separated flow case $\Lambda = 75°$, $\alpha = 8°$, $M = 2.8$ ($\mathrm{Re_{TE}} = 3.7 \times 10^6$). Whereas, it is conjectured that a complete transition in boundary-layer state did not occur for the attached flow case $\Lambda = 60°$, $\alpha = 8°$, $M = 2.8$ ($\mathrm{Re_{TE}} = 1.7 \times 10^6$).

Summary of Euler results. The results of the comparisons in a previous section between the Euler solutions and the experimental data are summarized in figure 34. For those cases expected to be clearly separated at the leading edge (through a subsonic leading-edge condition or a high angle of attack) or clearly attached at the leading edge (through a supersonic leading-edge condition at a low angle of attack), the Euler code is seen to be capable of predicting the primary flow structure. Typically, for those cases where the Navier-Stokes results showed a sensitivity to boundary-layer model of the primary flow structure predicted, the Euler code was incapable of predicting the type of primary flow structure experimentally observed. The Euler code is incapable of predicting any of the secondary flow structures such as secondary vortices or separation induced by a shock.

Code applicability. In examining the summaries presented in figures 33–34, several observations can be made on the suitability of the Navier-Stokes and Euler codes in supersonic wing design. The first region of interest is for a wing design at conditions where the flow will clearly separate at the leading edge or clearly remain attached at the leading edge. These regions are the shaded regions evident in figure 35. In these regions the Euler and Navier-Stokes codes have an equivalent ability in the prediction of the primary flow structure. However, if the wing design requires the prediction of secondary flow structures the Navier-Stokes code must be used. Also note that at the lower angles of attack the wing design should take into account the effects of boundary-layer model on the secondary structures predicted by the Navier-Stokes code.

14

The second region of interest is where the primary flow structure is computationally dependent on boundary-layer model. It is recommended that wing design conducted in this region not use the Euler code. The use of the Navier-Stokes code should account for the sensitivity to boundary-layer model.

Refinement of Experimental Data Classification

The computational study prompted a detailed re-examination of the data of reference 15. Listed in table I are the cases that were reclassified. With these changes imposed on the flow chart of figure 1(a), a different arrangement of the boundaries of the chart of α_N versus M_N is proposed and presented in figure 36. This type of boundary arrangement has also been proposed by other researchers (refs. 32 and 34).

This refinement of the classification provides for a smoother transition between separated and attached flow at the leading edge. The separation bubble with shock flow field is proposed as the transitional flow pattern. A discussion of the transition between separated and attached flows can be found in references 34 and 37 and is summarized here with the aid of the computational data. Presented in figure 37 are the cross-flow Mach number contour data for those cases that most closely correspond to lines AA and BB in the chart of α_N versus M_N at the top of figure 37. Line AA is at a constant α_N but varies in M_N, whereas line BB is at a constant M_N varying in α_N. The computational data presented in figure 37 are from the laminar Navier-Stokes solutions.

Along line AA, the angle the flow has to turn in order to be tangent to the surface remains constant since α_N is held constant. At low M_N, the energy of the flow normal to the leading edge is not sufficient to negotiate the expansion at the leading edge because of the turning angle. The result is leading-edge separation with primary and secondary vortices. With an increase in M_N, the flow normal to the leading edge has a greater energy level. Therefore, the flow can resist separation at the leading edge longer such that the separation angle between the surface and the vortex feeding sheet becomes smaller. The result is a flatter primary vortex of a lower intensity than that observed at the low M_N cases. Since the reattachment line of the flow corresponds to the inboard edge of the primary vortex, this type of flow is considered to be a separation bubble. However, in contrast to the definition of separation bubble in reference 15, secondary separation still occurs beneath the primary vortex, although the secondary separation is weaker because of the decrease in vortex intensity with an increase in M_N. A decrease in vortex intensity is evident in the decrease in the size of the primary vortex with increasing M_N. For sufficiently large M_N, the energy level of the flow is large enough to allow expansion of the flow around the leading edge without separation occurring. The result is attached flow at the leading edge.

The discussion above is for a transition between separated and attached flows at constant α_N with increasing M_N. The same trends in the transition of the primary flow structure are evident in the data corresponding to line BB along which α_N increases at a constant M_N. Along line BB the flow normal to the leading edge has the same energy level since M_N is held constant. However, as angle of attack increases the turning angle increases, and thus the expansion at the leading edge increases. For those cases along line BB that are at moderate angles of attack, the energy of the flow is capable of completing the expansion at the leading edge. The result is attached flow at the leading edge. For α_N large enough, the energy of the flow can no longer negotiate the expansion without separating at the leading edge. The size of this thin leading-edge separation increases as angle of attack increases. Although not evident in the present investigation, the separation could be expected to increase to a large primary vortex with further increases in angle of attack.

Conclusions

An Euler flow solver and a thin-layer Navier-Stokes computational flow solver have been used to numerically simulate the supersonic lee-side flow fields over delta wings. These lee-side flow fields have been experimentally observed over sharp leading-edge delta wings through parametric variations in leading-edge sweep, angle of attack, and Mach number. Throughout the computational study, Mach number was held constant at 2.8. The flow fields over three delta wings with 75°, 67.5°, and 60° leading-edge sweeps were computed over an angle-of-attack range of 4° to 20°. Conical solutions were used throughout the computational study. A comparison of three-dimensional Navier-Stokes solutions with the conical Navier-Stokes solutions computationally illustrates that the flow is essentially conical for the conditions examined in this investigation, as has been observed experimentally. The effects of Reynolds number are confined to small changes in the secondary flow features; these changes can be modeled through the use of conical solutions at varying Reynolds numbers. The conical Navier-Stokes solutions with the laminar-boundary-layer model (as opposed to the turbulent-boundary-layer model) agreed better with the experimental data, especially for the lower sweep delta wings.

The Euler code is adequate in predicting the primary flow structure (i.e., a primary vortex or a cross-flow shock) where the flow is clearly separated or attached at the leading edge because of the flow conditions normal to the leading edge. The Euler code is incapable of modeling the secondary vortices and shock-induced separations observed experimentally. The Navier-Stokes code is capable of predicting both primary and secondary flow features regardless of the flow conditions normal to the leading edge.

The observations made throughout the computational study prompted a detailed reexamination of the Miller and Wood experimental data. This resulted in a refinement of the flow classification chart that classifies the six flow regions of interest as functions of angle of attack and Mach number normal to the leading edge. This refinement of the flow classifications results in a transitional flow between separated and attached flows with the separation bubble with shock flow as the intermediate flow pattern. Viewing the separation bubble with shock flow as an intermediate flow pattern is supported by the Navier-Stokes computations, which show that a separation bubble, with or without a shock, is a narrow primary vortex whose core lies close to the surface of the wing, with secondary separation occurring beneath the primary vortex.

The computational boundary-layer model was not observed to influence the prediction ability of the Navier-Stokes code of the primary flow field with flows that are not within the intermediate flow region between the separated and attached flow regions. At high angles of attack, the boundary-layer model had a minimal influence on the secondary separation predicted by the Navier-Stokes code. However, at low angles of attack there was a substantial influence of boundary-layer model on the secondary separation. For separated flow, the influence of boundary-layer model was on the extent of secondary separation, whereas for attached flow the influence was on the type of secondary separation.

The computational boundary-layer model was observed to influence the ability of the Navier-Stokes code to predict the primary flow structure in the intermediate flow region between the separated and attached flow regions. The flow pattern in this intermediate flow region is a thin leading-edge separation. The primary explanation for this observation is that the boundary-layer model affects the ability of the flow to negotiate the expansion of the flow at the leading edge. The observation that the separation was very thin indicates that a possible interaction of the shock with the boundary layer and the vortex is occurring and is sensitive to boundary-layer model. In this same region the Euler code is incapable of predicting the type of primary flow experimentally observed.

Table I. Reclassified Cases

Λ, deg	α, deg	M	Previous classification	Reclassification
67.5	4	1.7	Primary and secondary vortex	Separation bubble
67.5	4	2.0	Primary and secondary vortex	Separation bubble
60	12	1.7	Separation bubble	Separation bubble with shock
60	12	2.0	Shock-induced separation	Separation bubble with shock
52.5	16	1.7	Shock-induced separation	Separation bubble with shock
52.5	20	1.7	Shock-induced separation	Separation bubble with shock
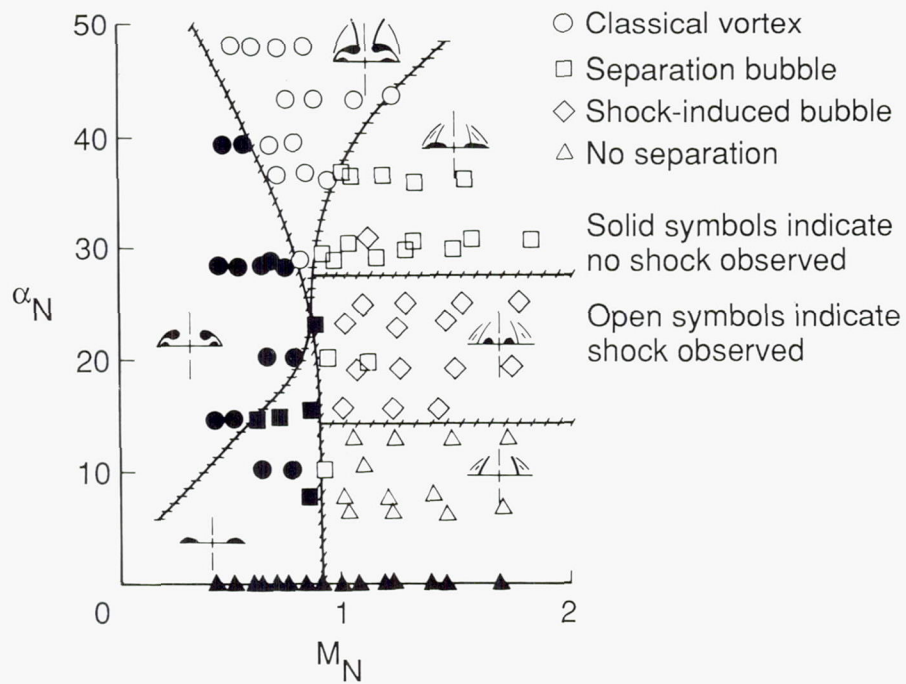
(a) Flow classification chart.
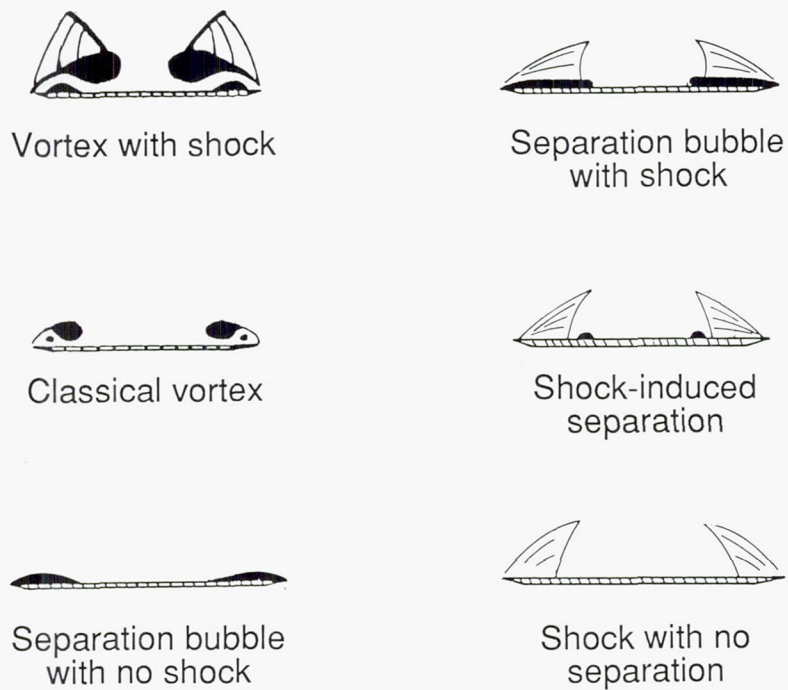
(b) Sketches of flow patterns.

Figure 1. Classification of experimental data for sharp-leading-edge delta wings (ref. 15).
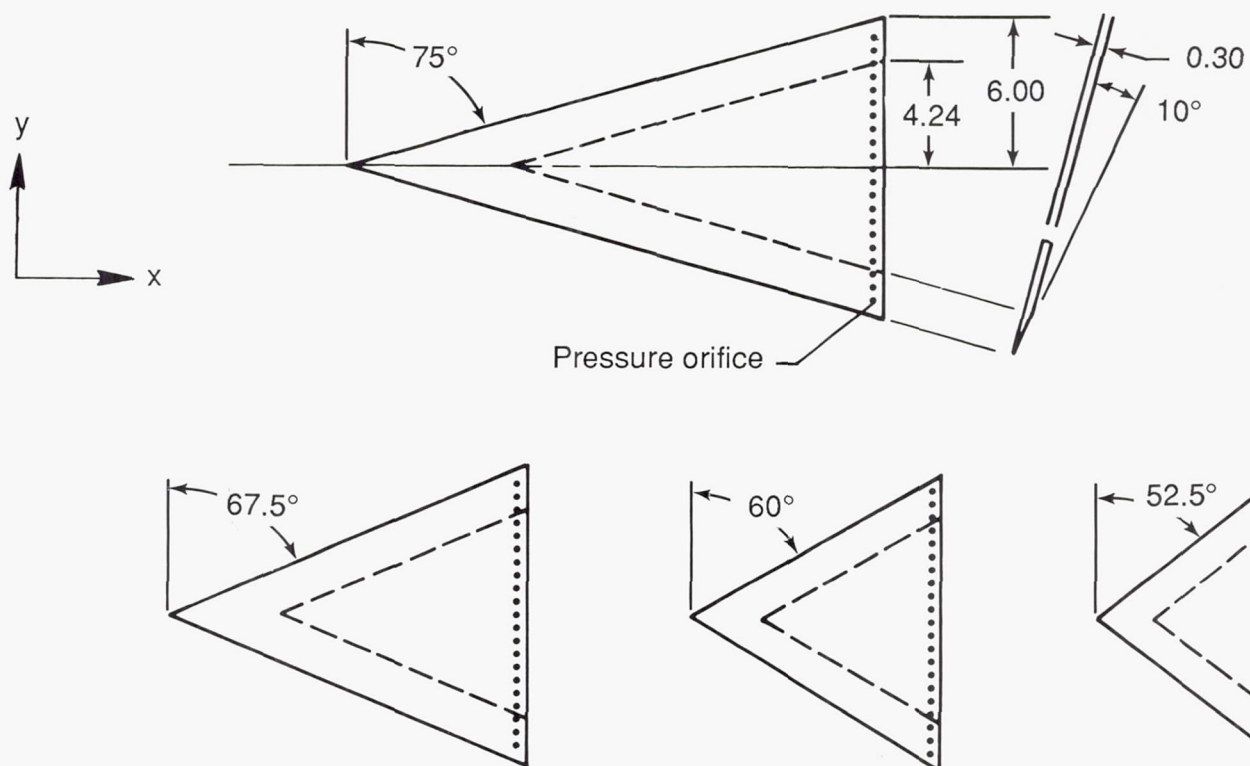
Figure 2. Sketches of the delta wing models from the wind-tunnel test of reference 15. Linear dimensions in inches.
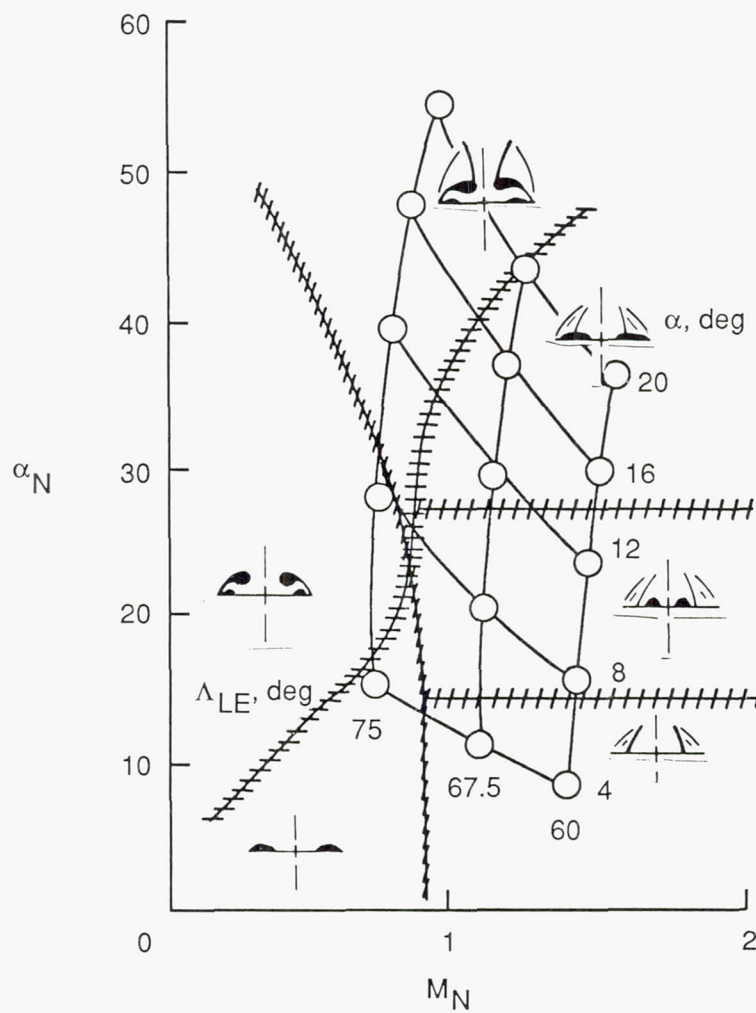
Figure 3. Test matrix for the computational study; free-stream Mach number held constant at 2.8.
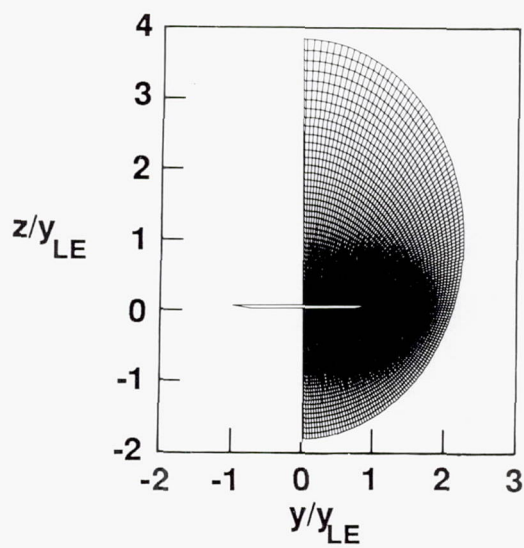
(a) Total grid.
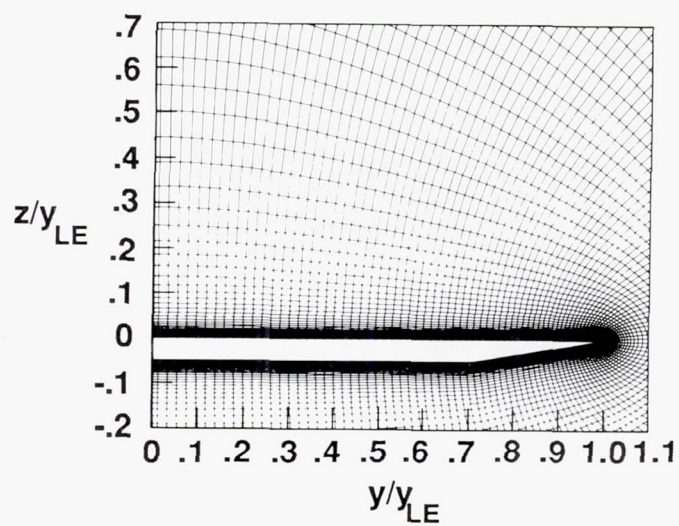
(b) Close-up of grid around the surface.

Figure 4. A typical grid used in the Navier-Stokes solutions.
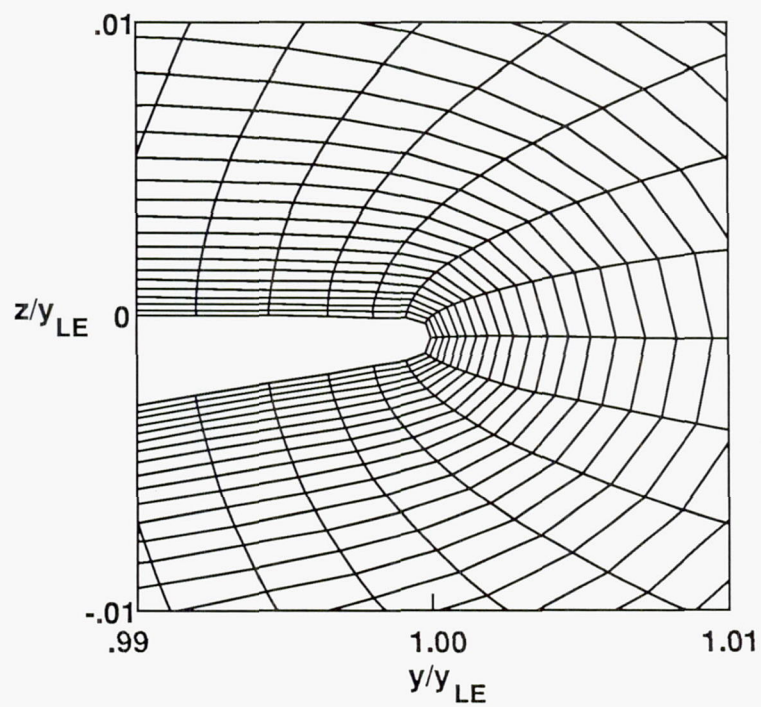
(a) Laminar boundary layer.
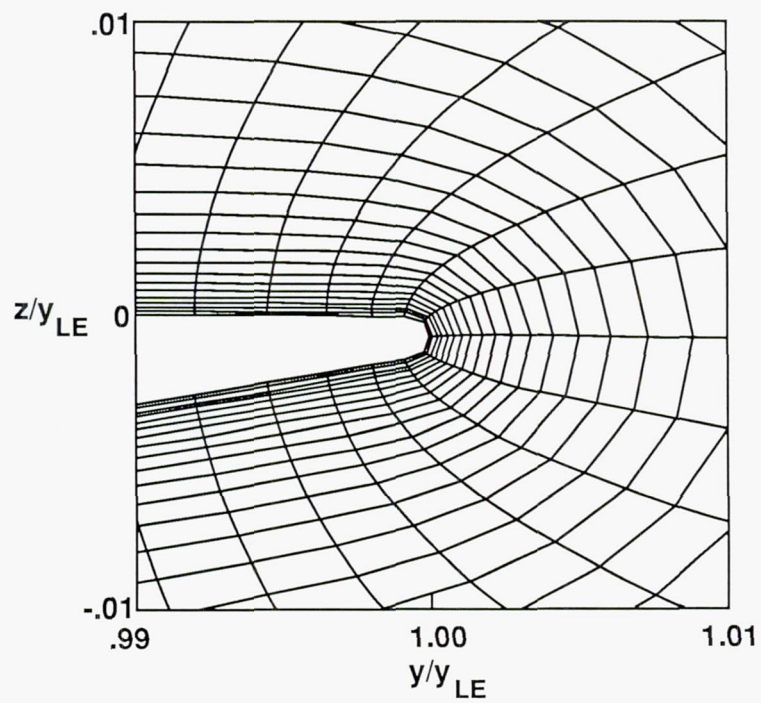
(b) Turbulent boundary layer.

Figure 5. Grid spacing for the laminar- and turbulent-boundary-layer Navier-Stokes solutions.
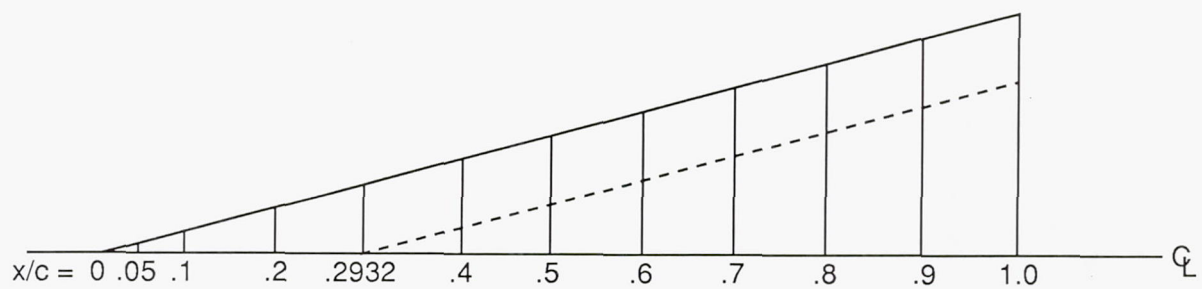
(a) *x*-stations.
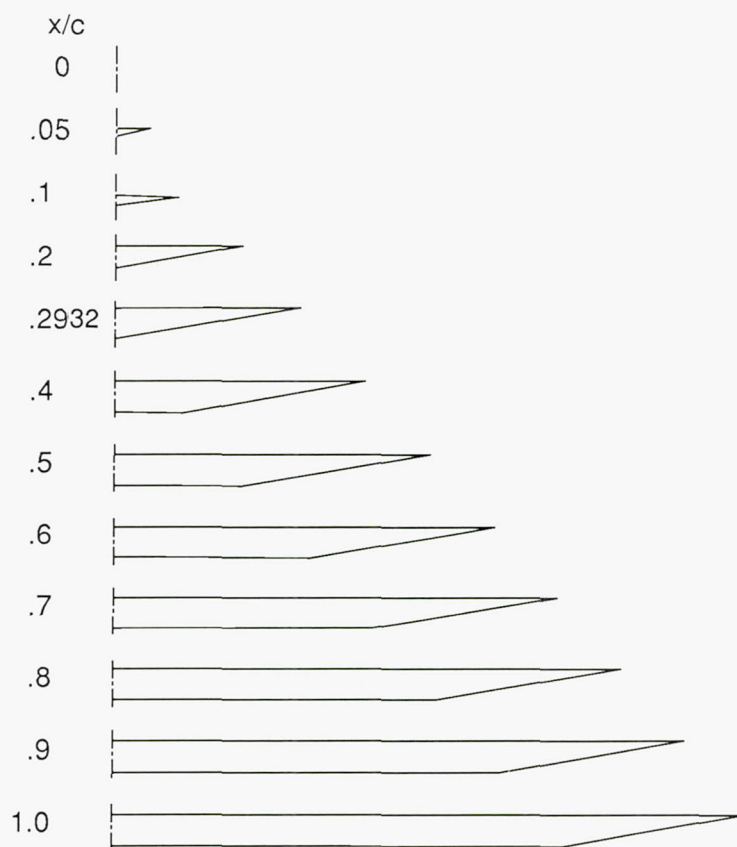
(b) Cross sections.

Figure 6. Three-dimensional Navier-Stokes grid for the 75° delta wing.
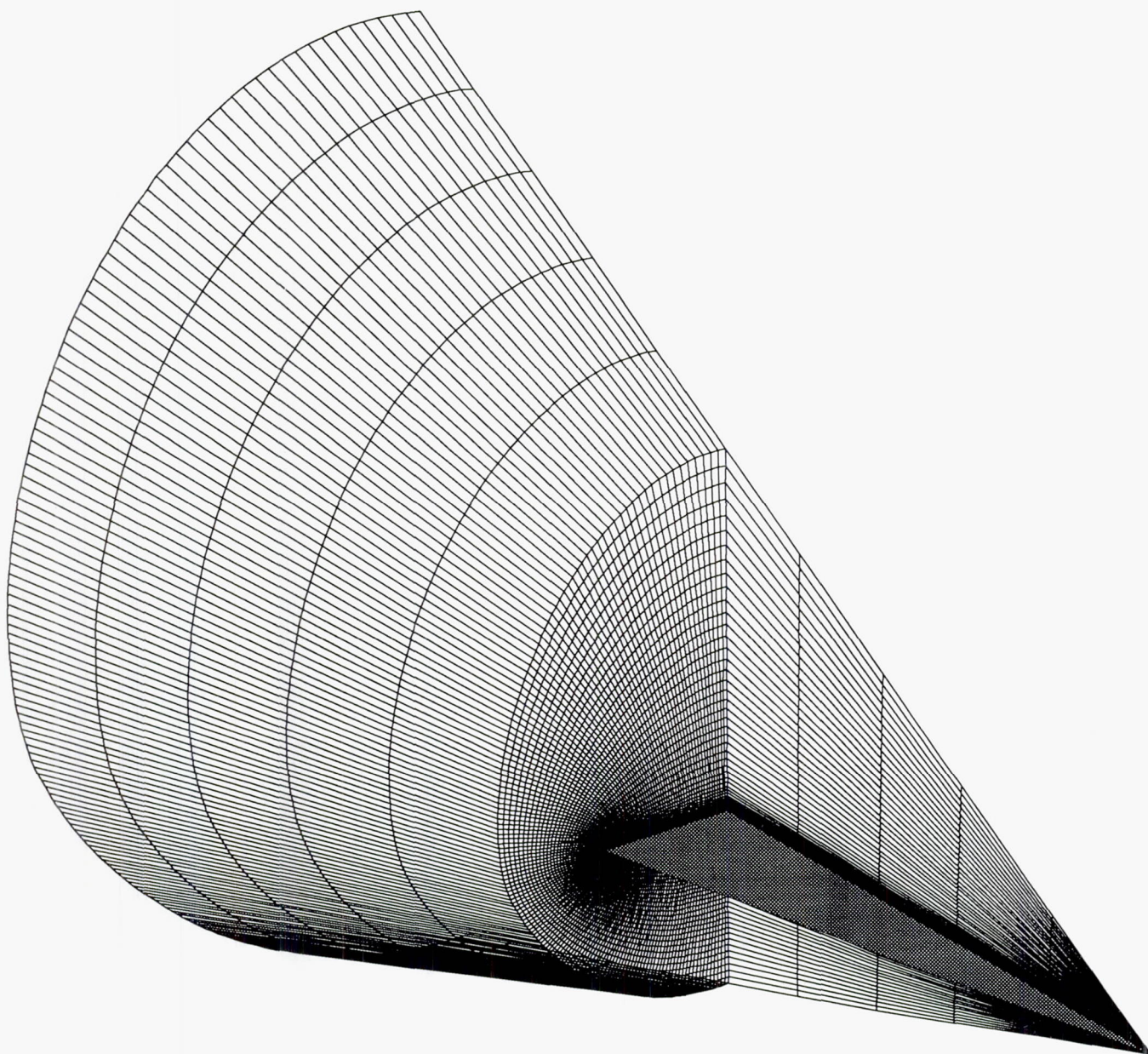
(c) Oblique view of grid.

Figure 6. Concluded.
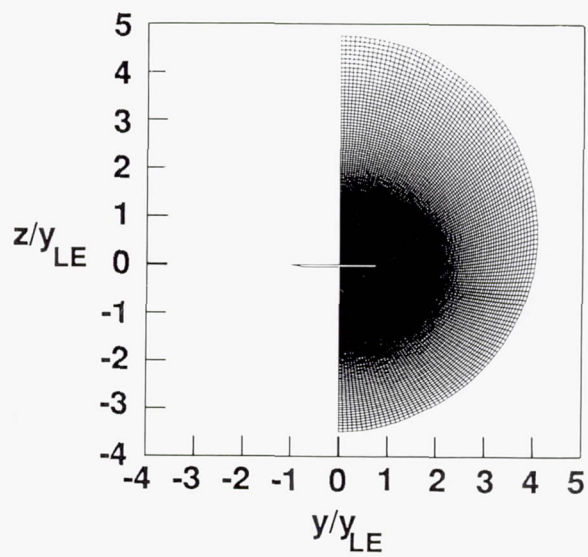
(a) Total grid.
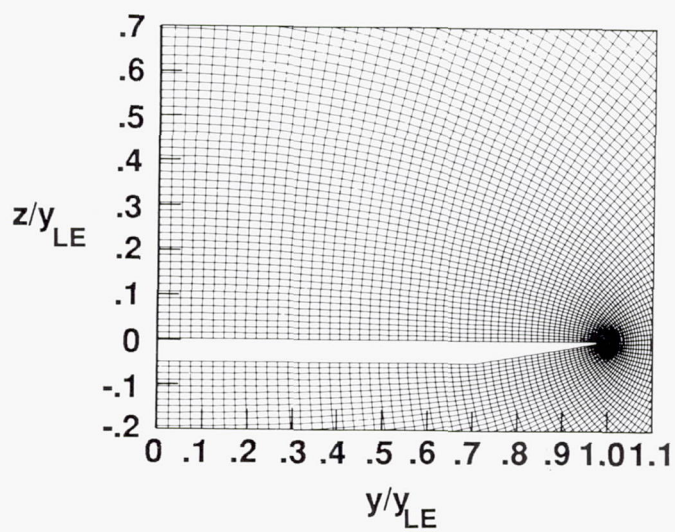
(b) Close-up view.

Figure 7. A typical grid used in the conical Euler solutions.
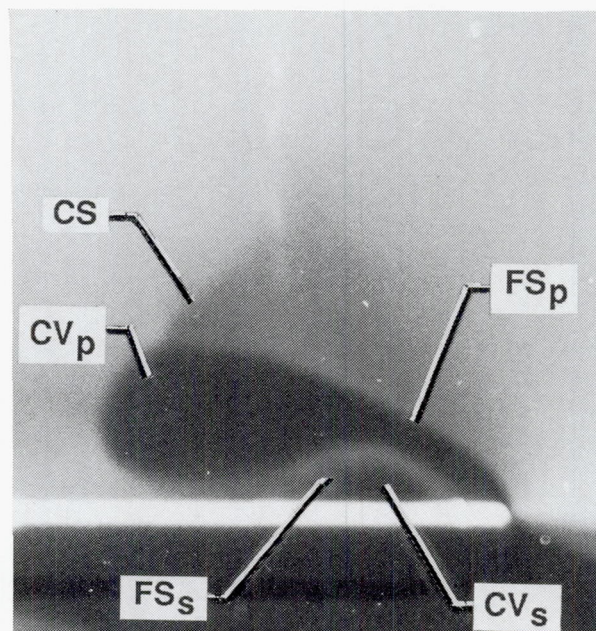
Figure 8. Vapor-screen photograph for $\Lambda = 75°$, $\alpha = 16°$, and $M = 2.8$.
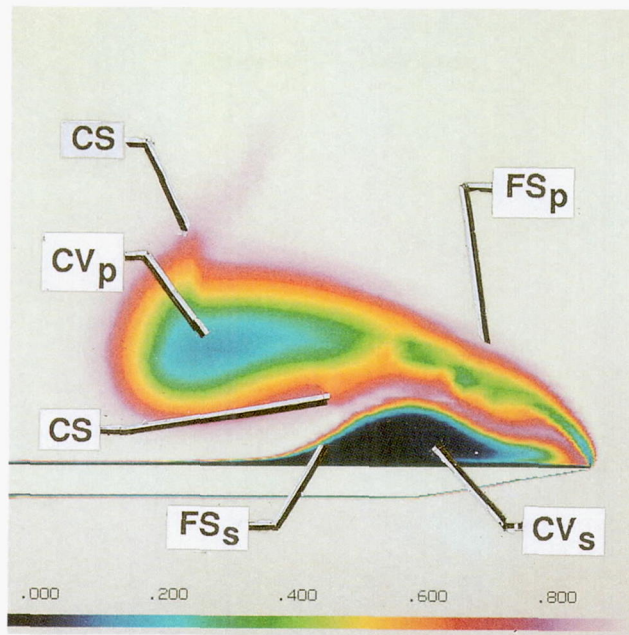
(a) Total pressure ratio.
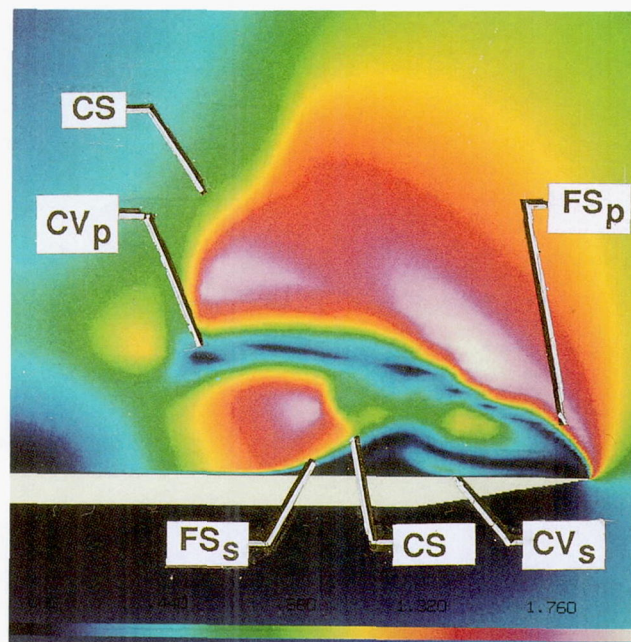
(b) Cross-flow Mach number.

Figure 9. Color contour data from the laminar-boundary-layer solution for $\Lambda = 75°$, $\alpha = 16°$, and $M = 2.8$.
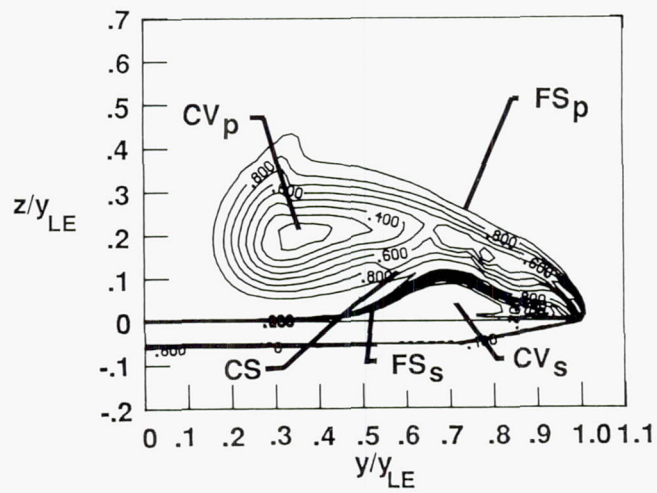
(a) Total pressure ratio.
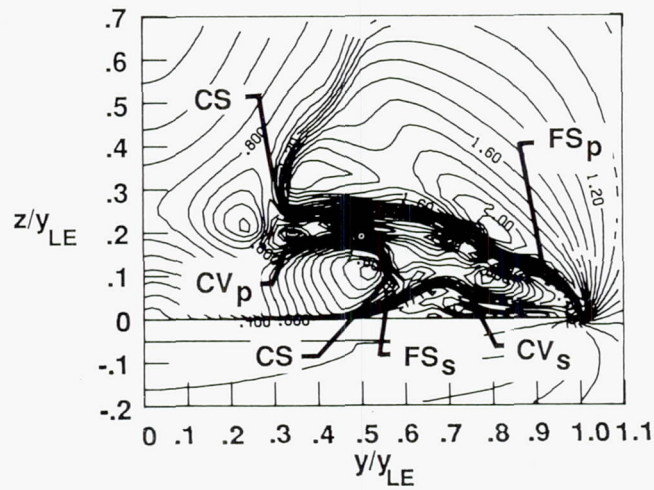
(c) Cross-flow velocity vectors.
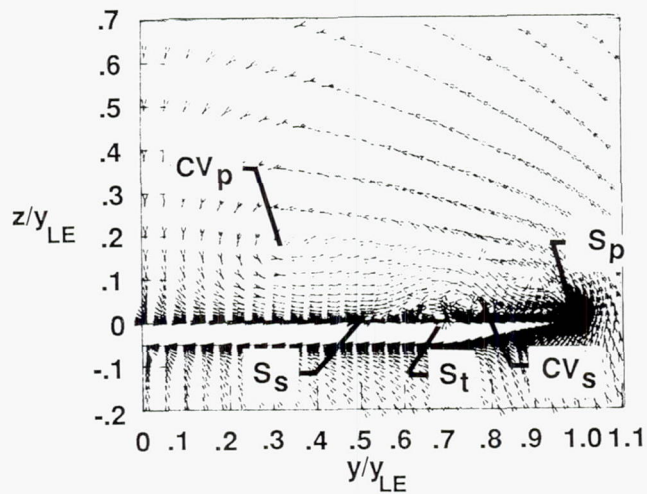
(b) Cross-flow Mach number.

Figure 10. Computational data from the laminar-boundary-layer solution for $\Lambda = 75°$, $\alpha = 16°$, and $M = 2.8$.

28
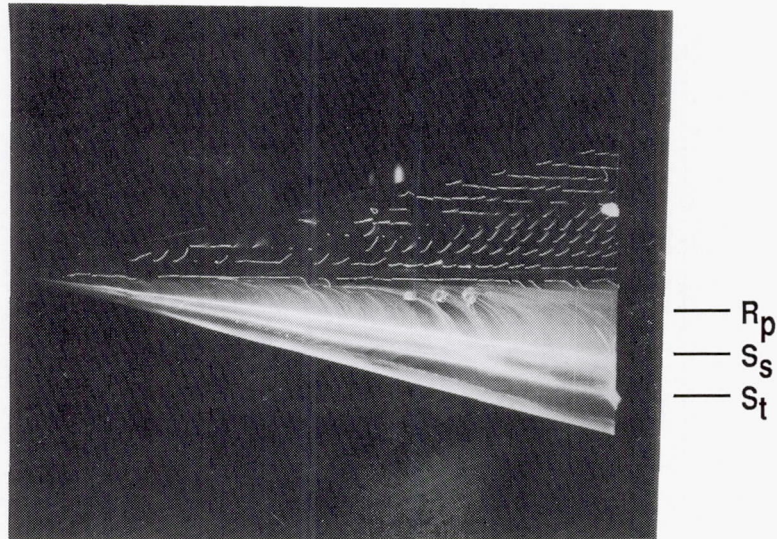
Figure 11. Oil-flow photograph for $\Lambda = 75°$, $\alpha = 16°$, and $M = 2.8$.
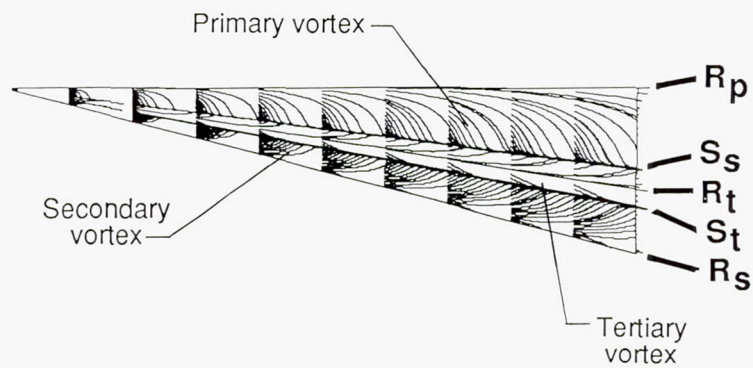
Figure 12. Particle trace data from the laminar-boundary-layer solution for $\Lambda = 75°$, $\alpha = 16°$, and $M = 2.8$.
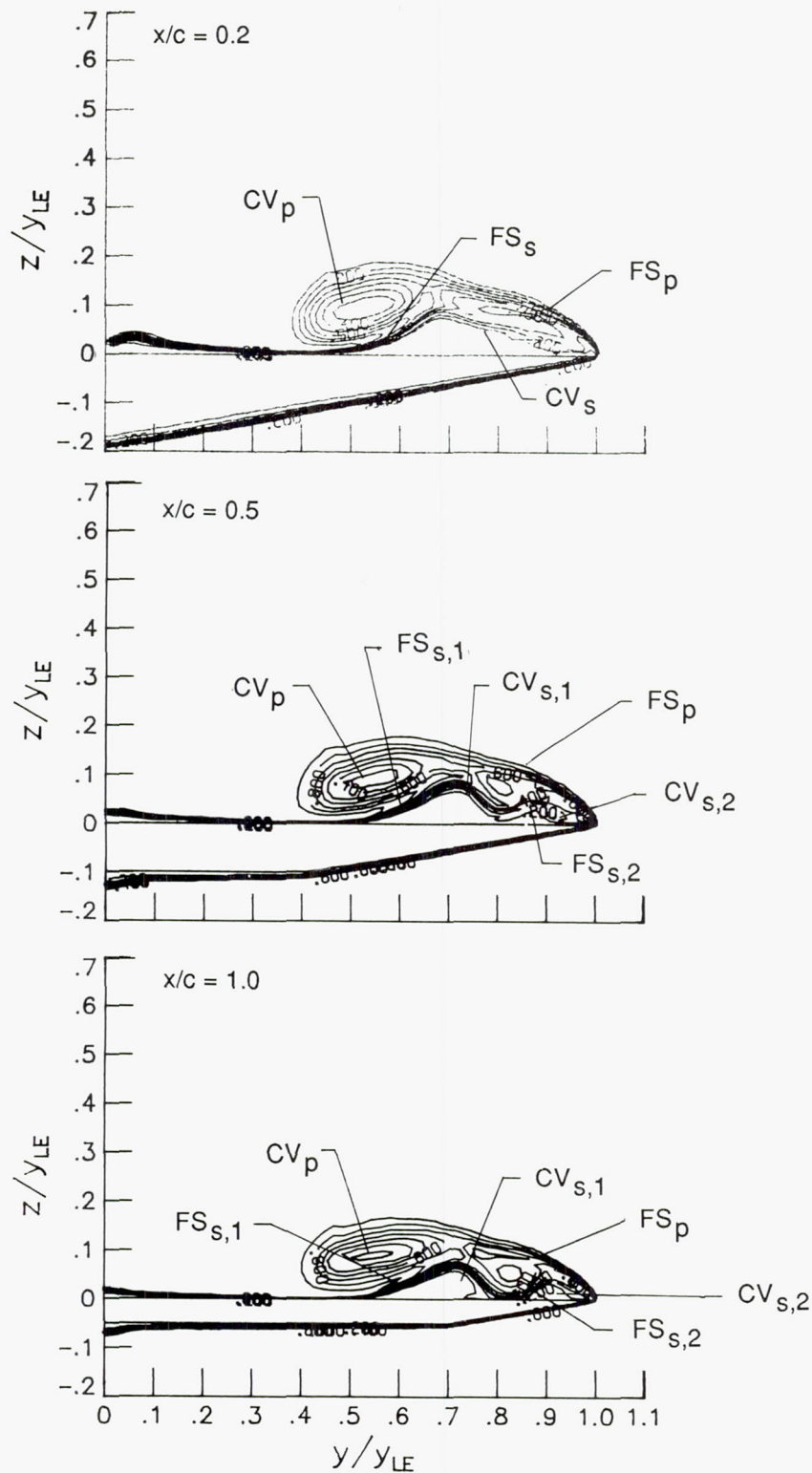
(a) Total pressure ratio contours at three x-stations.

Figure 13. Computational data from the three-dimensional laminar Navier-Stokes solution for $\Lambda = 75°$, $\alpha = 8°$, and $M = 2.8$.
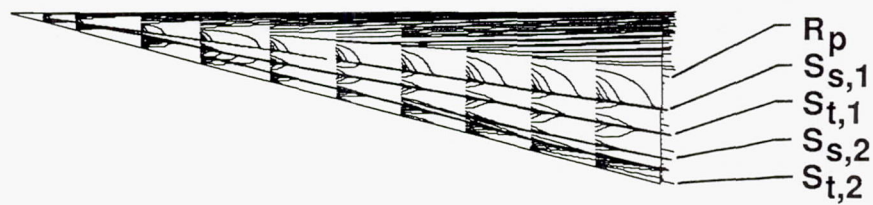
(b) Particle trace data.
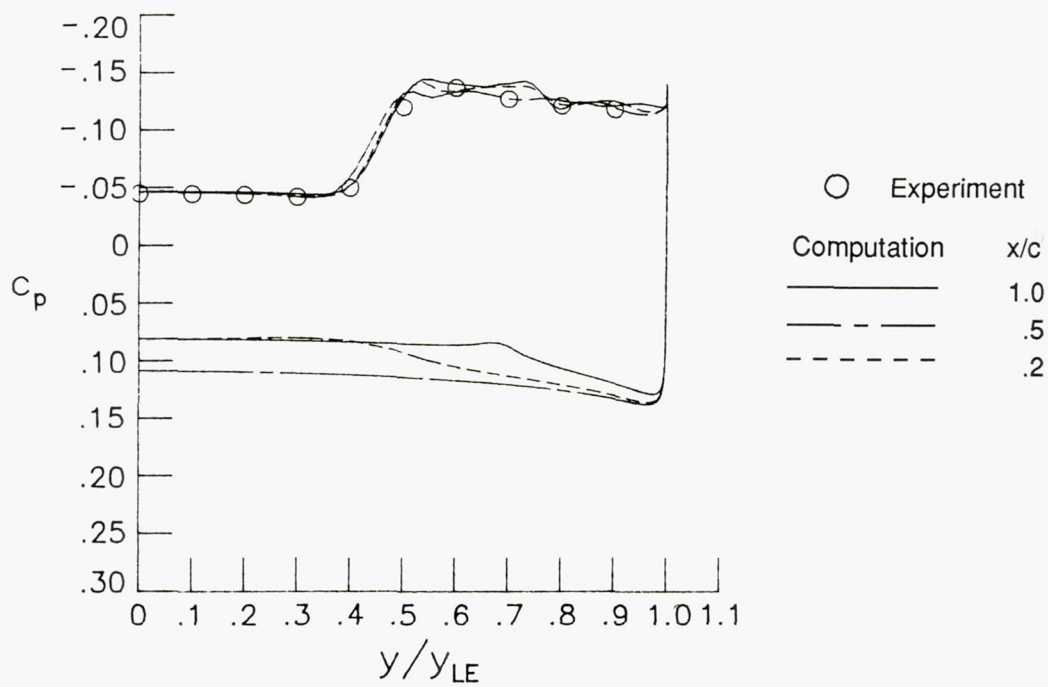
(c) Surface pressure distributions.

Figure 13. Concluded.

(a) Total pressure ratio contours.

Figure 14. Computational data from the conical laminar Navier-Stokes solutions at various Reynolds numbers for $\Lambda = 75°$, $\alpha = 8°$, and $M = 2.8$.

Re = 0.5 x 10^6

R_p
S_s
S_t

Re = 1.0 x 10^6

R_p
$S_{s,1}$
S_t
$S_{s,2}$

Re = 3.73 x 10^6

R_p
$S_{s,1}$
$S_{t,1}$
$S_{s,2}$
$S_{t,2}$
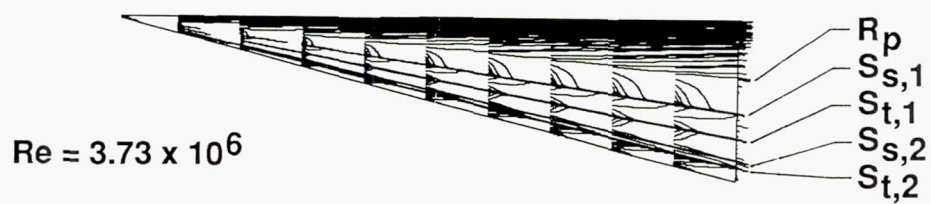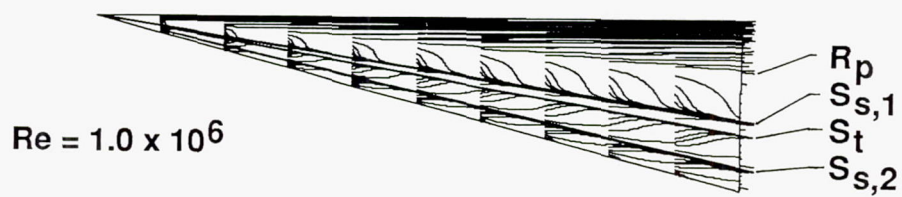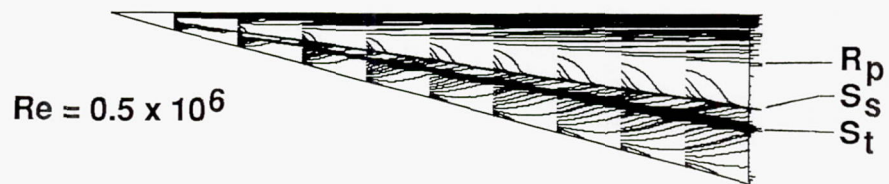
(b) Particle trace data.

Figure 14. Continued.

33
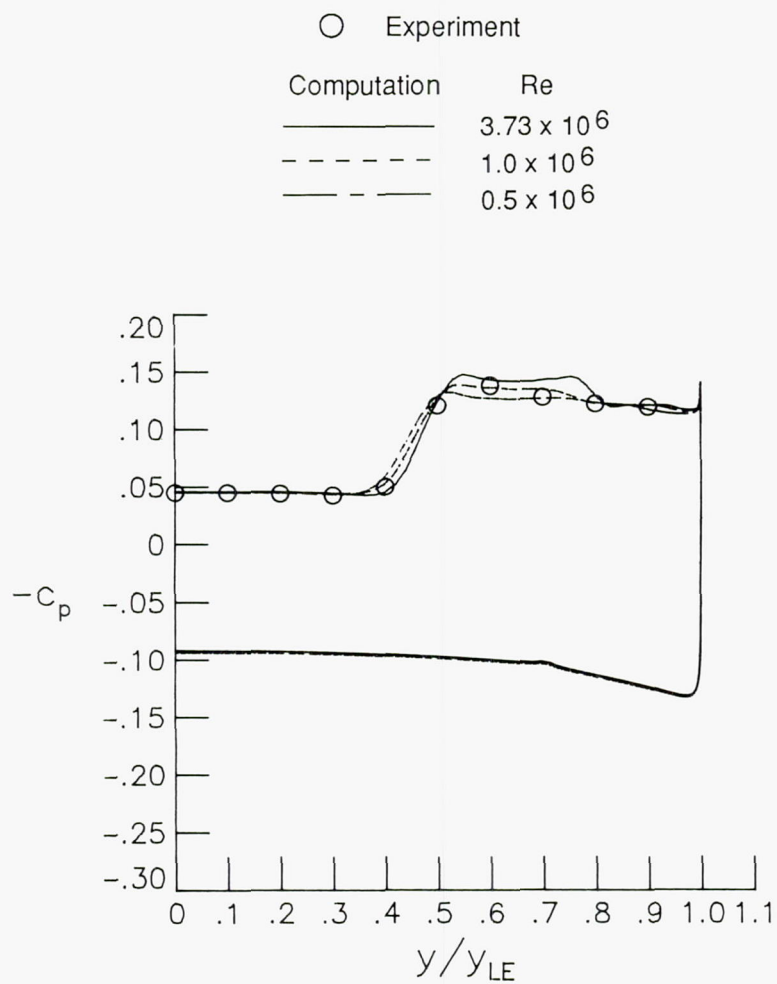
(c) Surface pressure distributions.

Figure 14. Concluded.
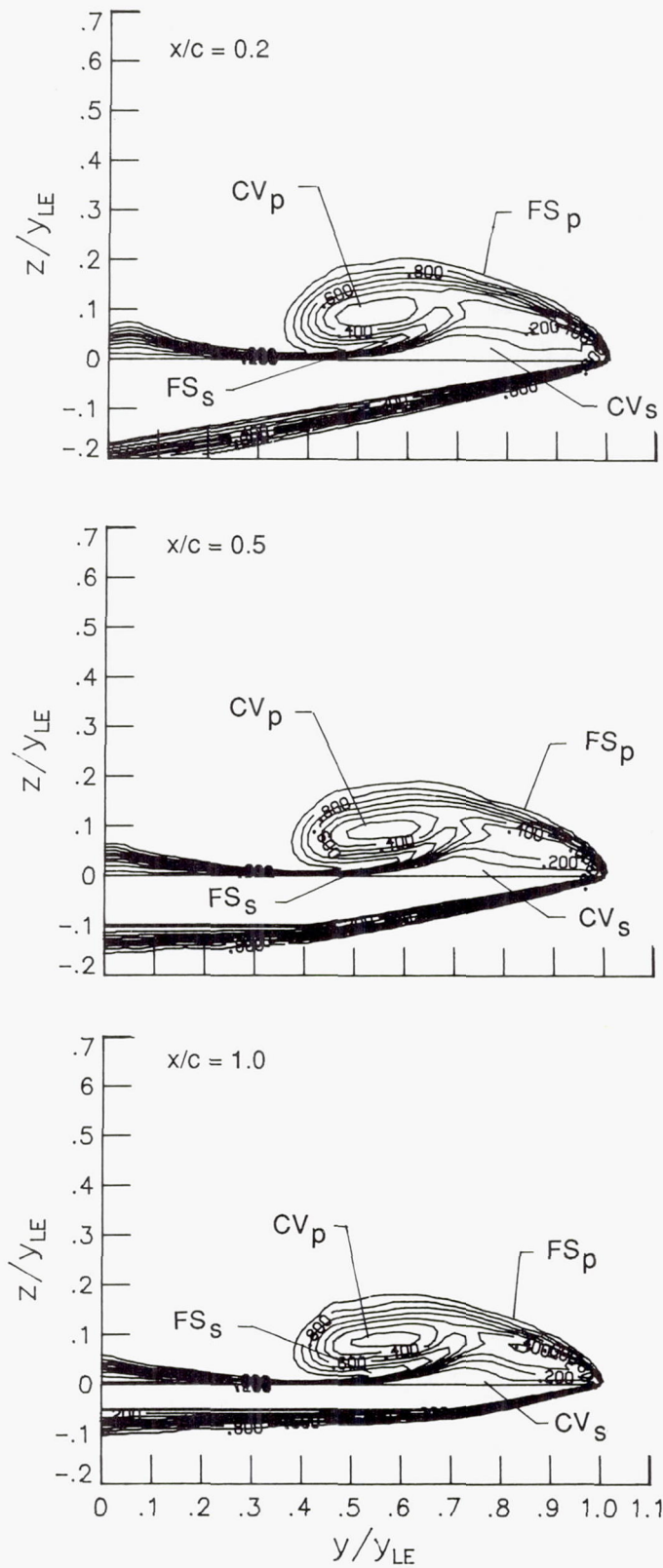
(a) Total pressure ratio contours.

Figure 15. Computational data from the turbulent three-dimensional Navier-Stokes solution for $\Lambda = 75°$, $\alpha = 8°$, and $M = 2.8$.
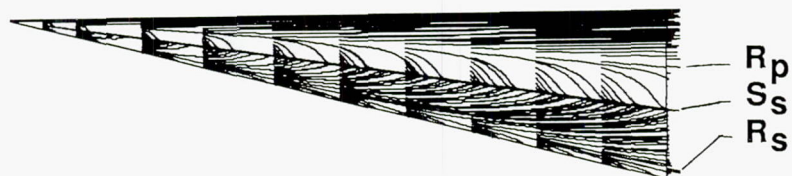
(b) Particle trace data.
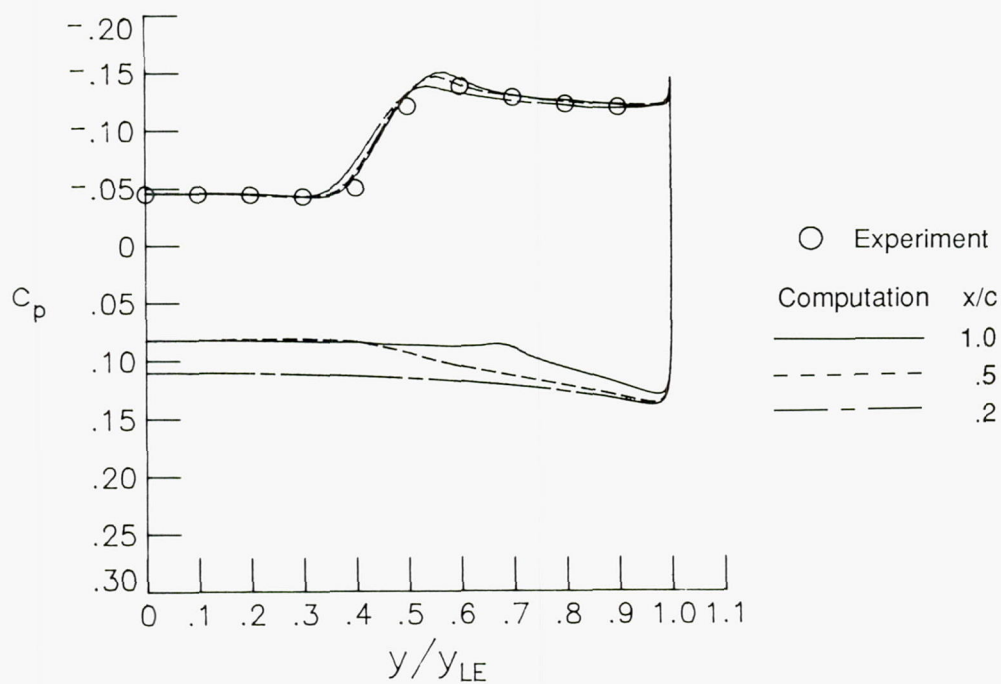
(c) Surface pressure distributions.

Figure 15. Concluded.
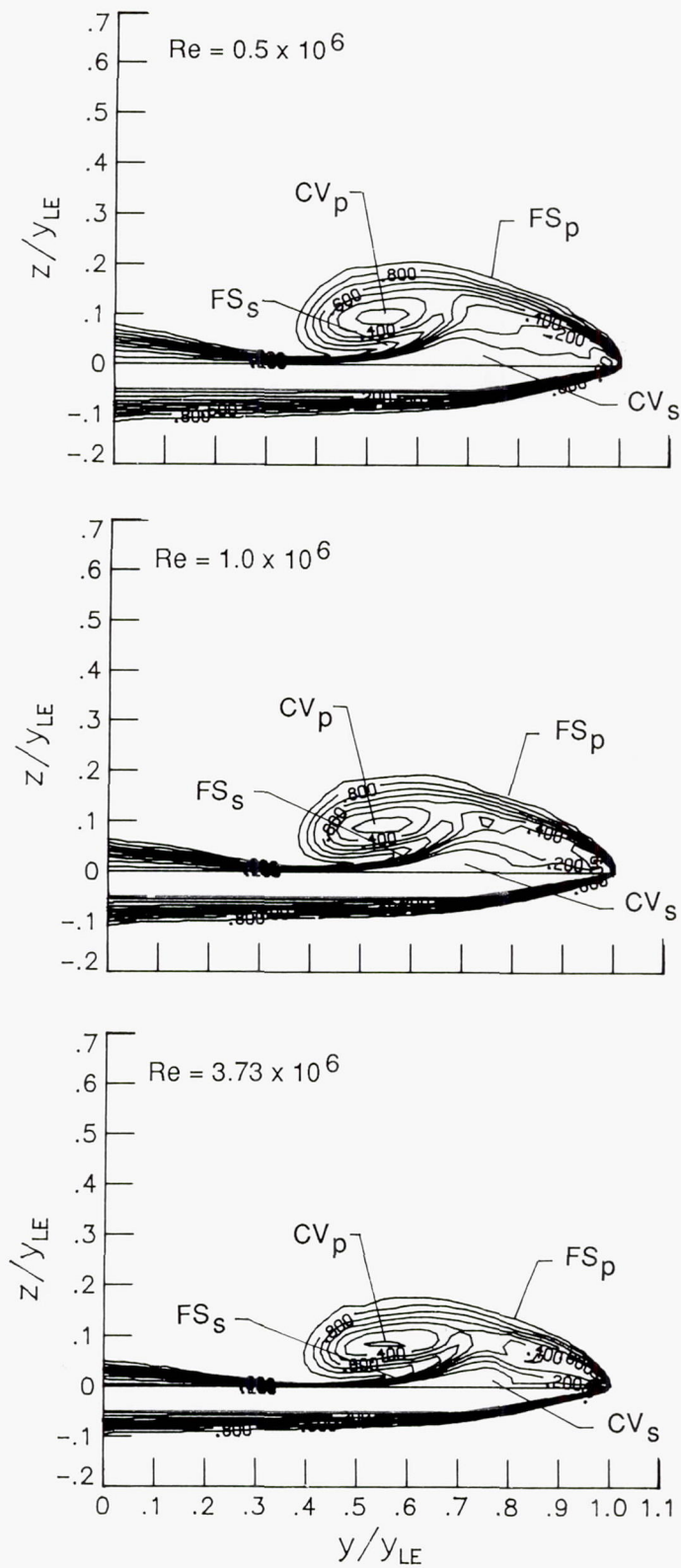
(a) Total pressure ratio contours.

Figure 16. Computational data from the conical turbulent Navier-Stokes solutions at various Reynolds numbers for $\Lambda = 75°$, $\alpha = 8°$, and $M = 2.8$.

$Re = 0.5 \times 10^6$

R_p
S_s
R_s

$Re = 1.0 \times 10^6$

R_p
S_s
R_s

$Re = 3.73 \times 10^6$

R_p
S_s
R_s
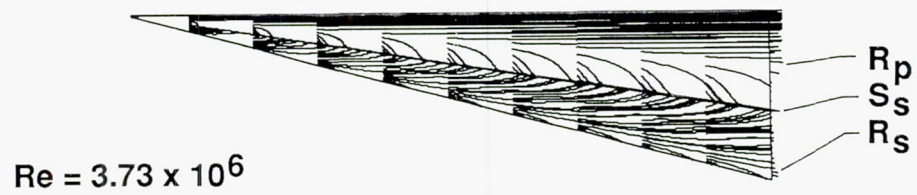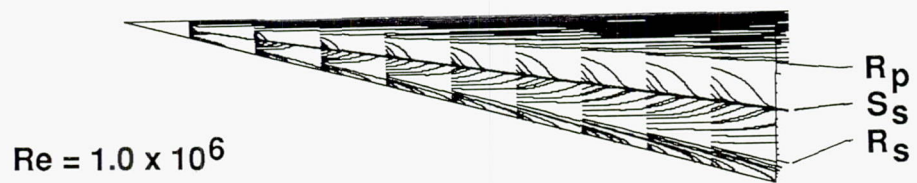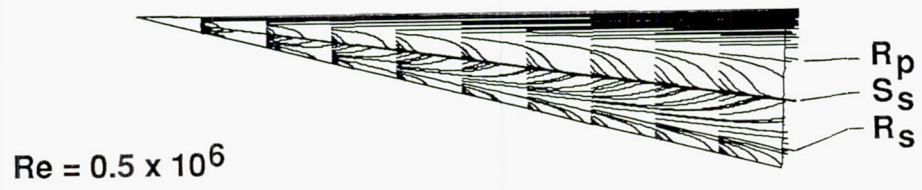
(b) Particle trace data.

Figure 16. Continued.

C_p

−.20
−.15
−.10
−.05
0
.05
.10
.15
.20
.25
.30

0 .1 .2 .3 .4 .5 .6 .7 .8 .9 1.0 1.1

y/y_{LE}

○ Experiment

Computation   Re

———————— 3.73×10^6

– – – – – – 1.0×10^6

— – — – — 0.5×10^6
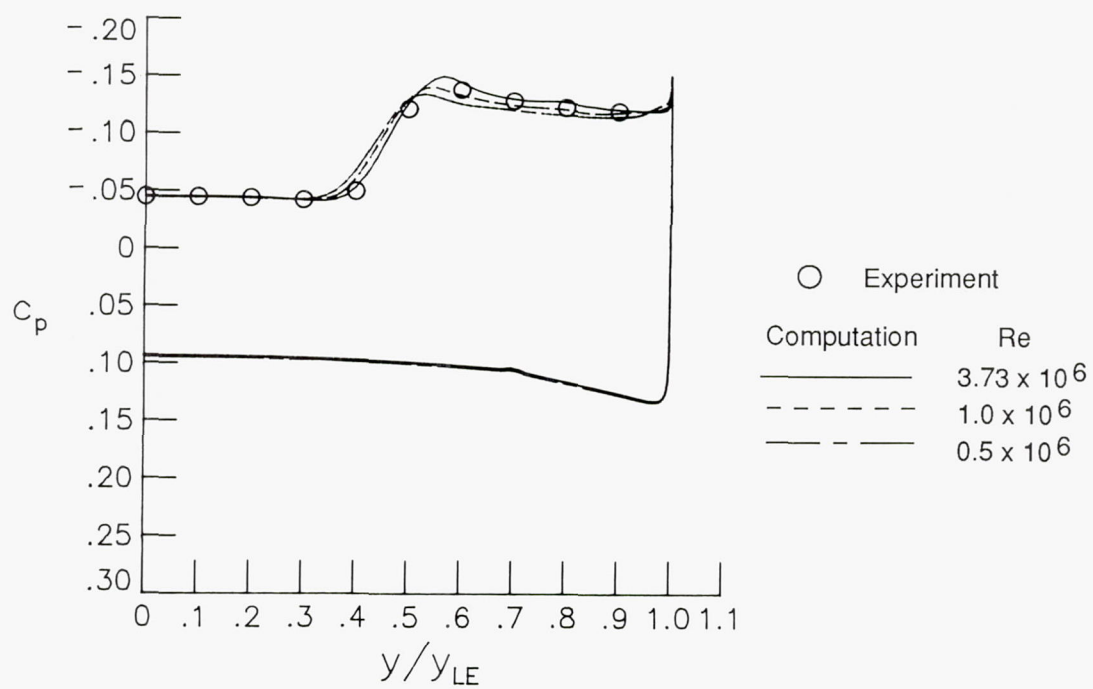
(c) Surface pressure distribution.

Figure 16. Concluded.
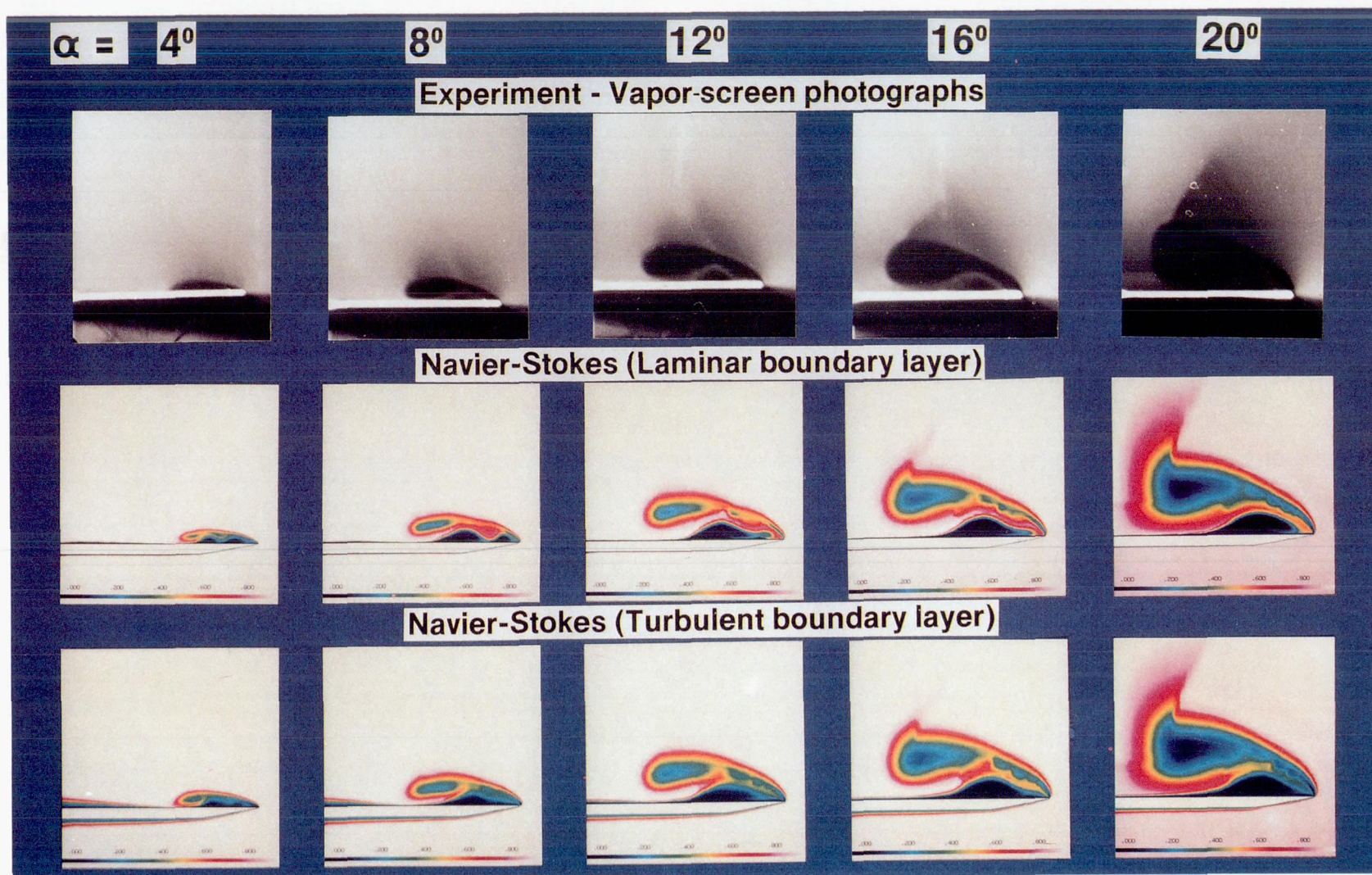
(a) Total pressure ratio.

Figure 17. Vapor-screen photographs and conical Navier-Stokes color contour data for the 75° delta wing at $M = 2.8$ and $\alpha = 4°$, $8°$, $12°$, $16°$, and $20°$.

α = 4° 8° 12° 16° 20°

Experiment - Vapor-screen photographs

Navier-Stokes (Laminar boundary layer)

Navier-Stokes (Turbulent boundary layer)
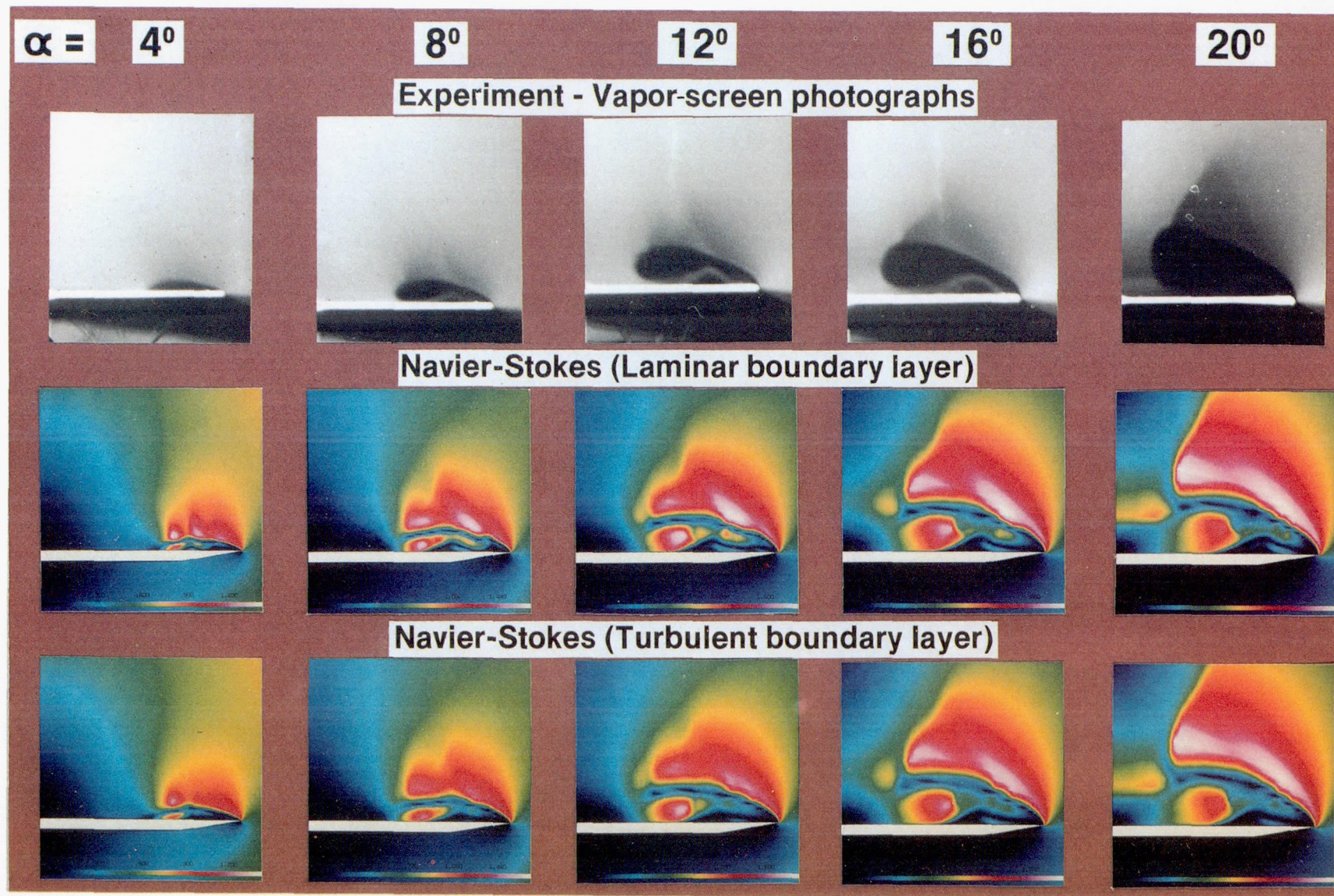
(b) Cross-flow Mach number.

Figure 17. Continued.

41
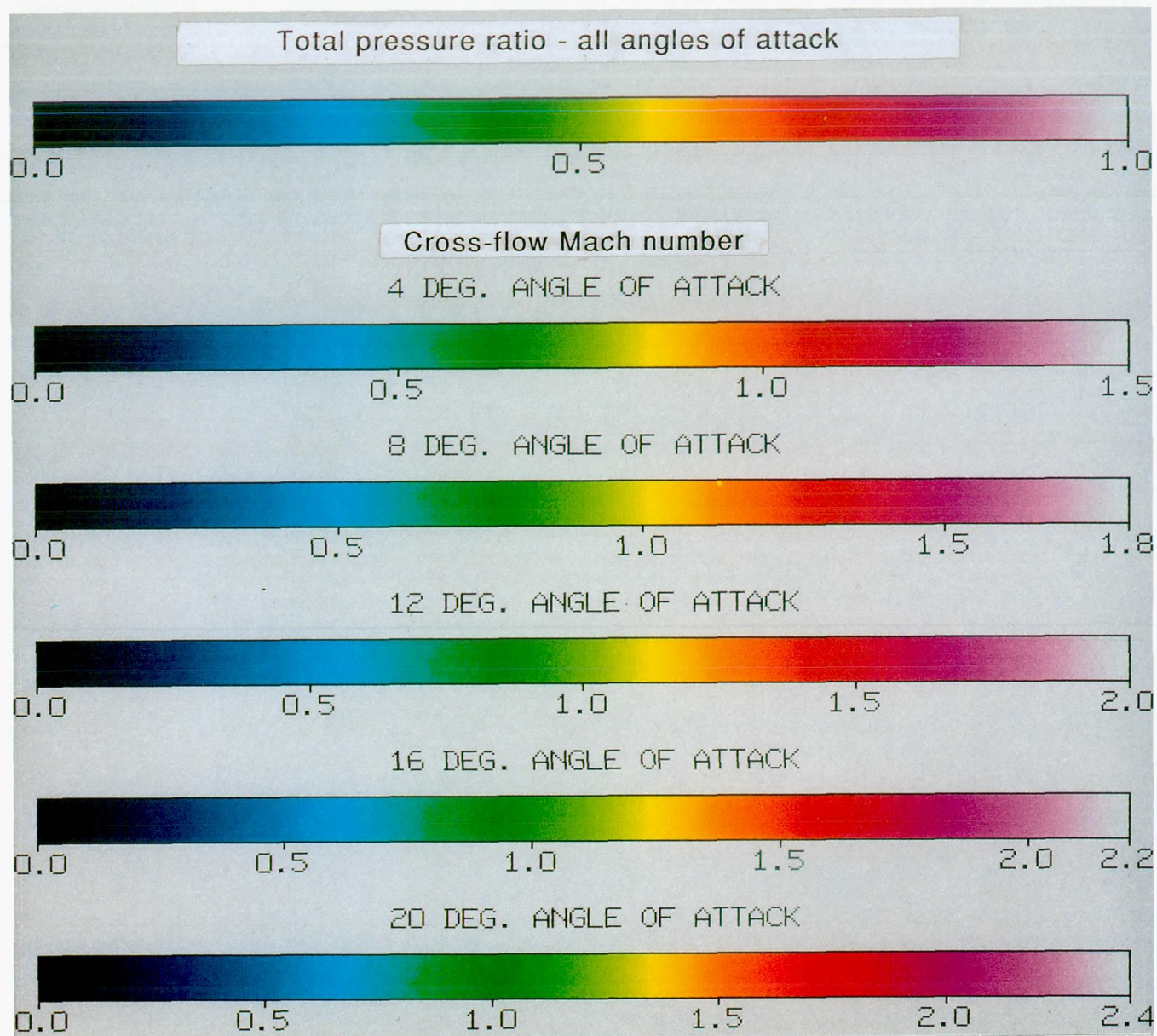
(c) Color bar definitions.

Figure 17. Concluded.
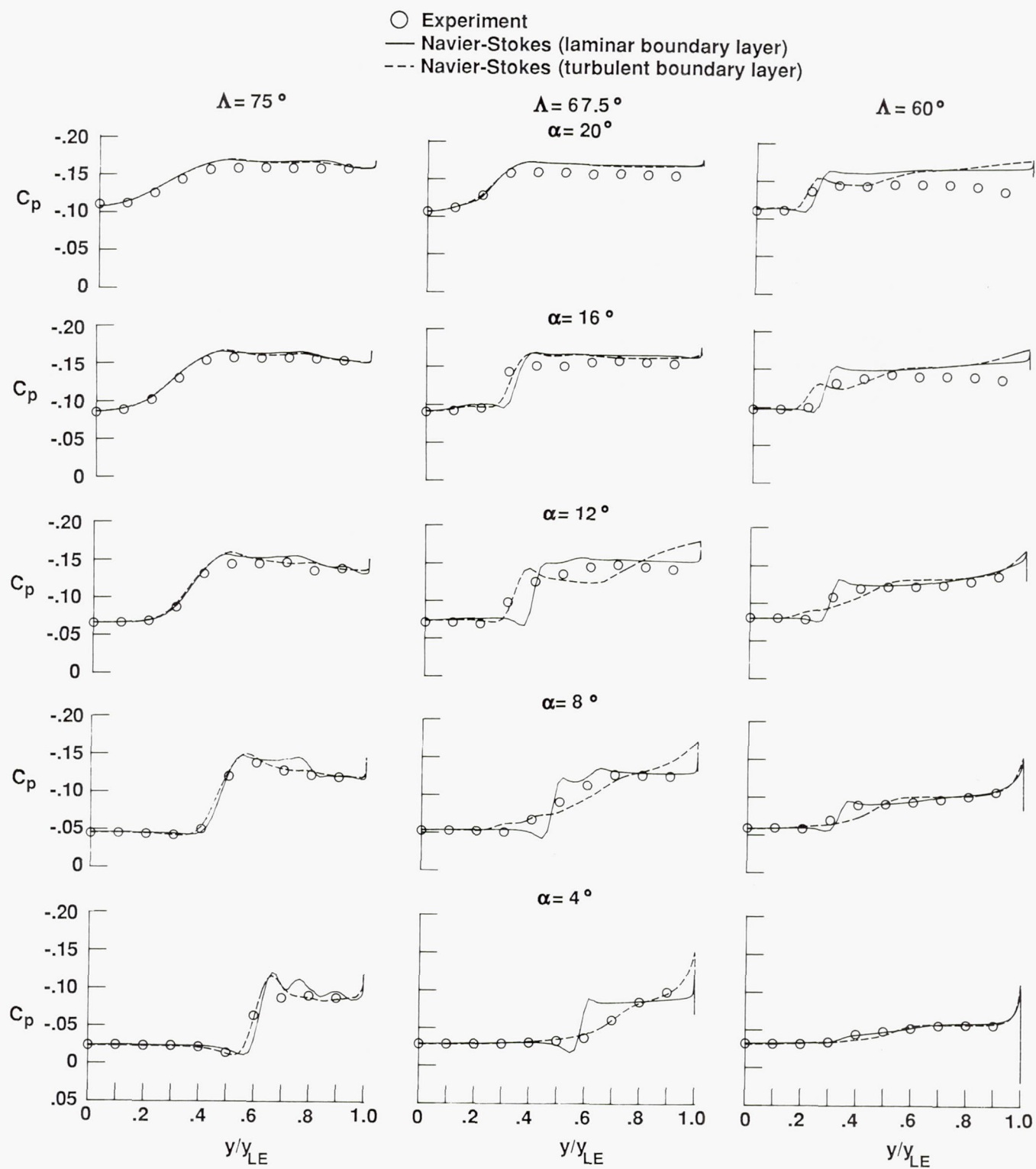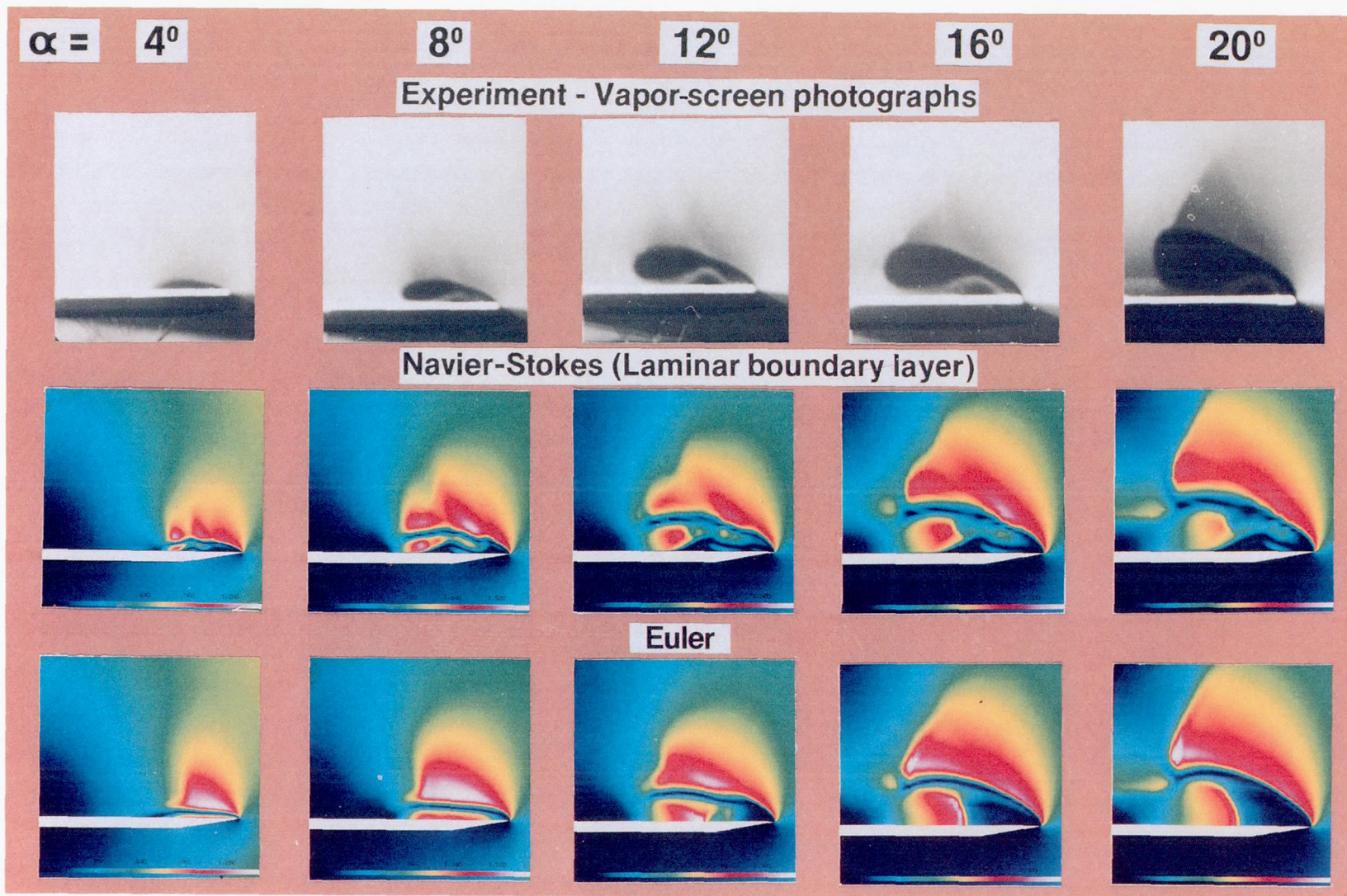
Figure 18. Comparison of experimental and conical Navier-Stokes computational surface pressure distributions for the 15 test cases.
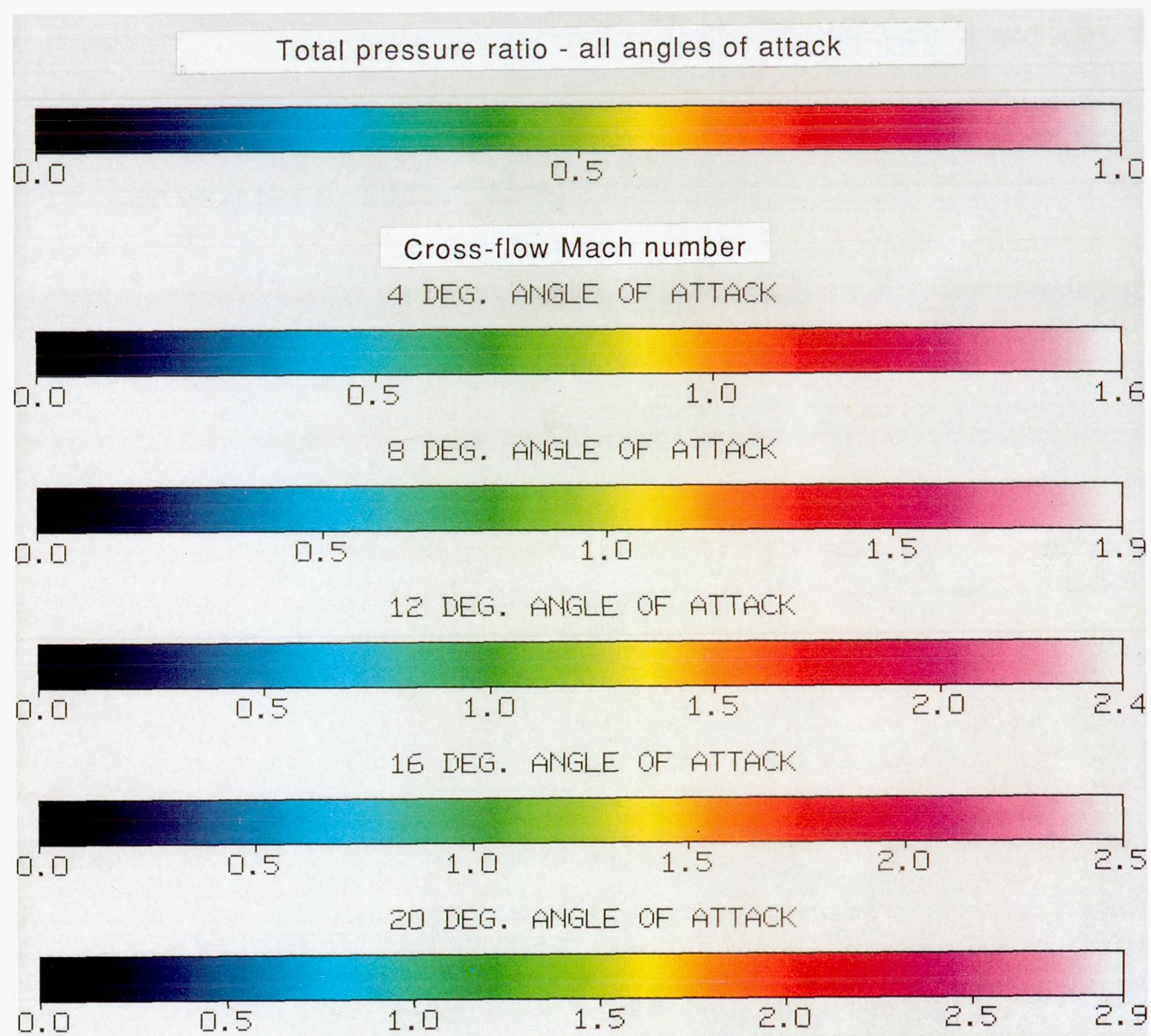
Experimental data

Vapor screen

Oil flow

Computational data

Total pressure

Particle trace

Surface pressure distribution

Laminar boundary layer

Turbulent boundary layer
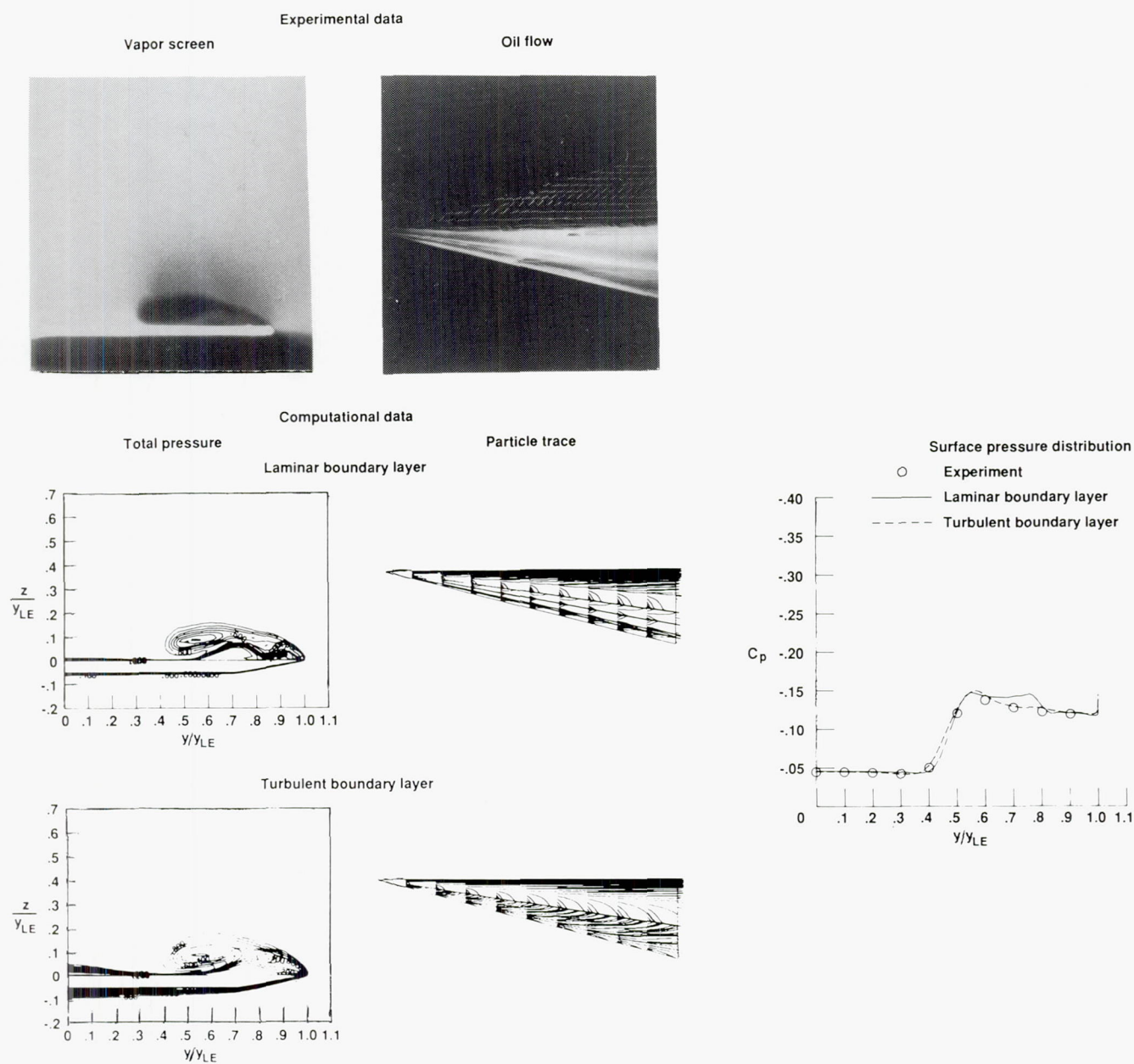
Figure 19. Comparison of experimental and conical Navier-Stokes computational data for $\Lambda = 75°$, $\alpha = 8°$, and $M = 2.8$.
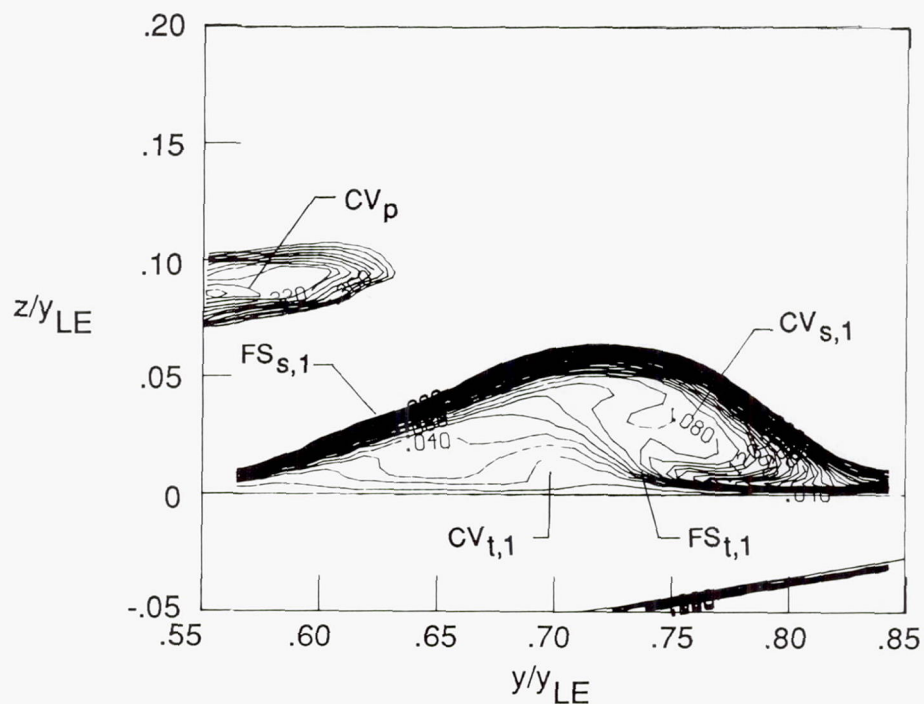
(a) Total pressure ratio contours.
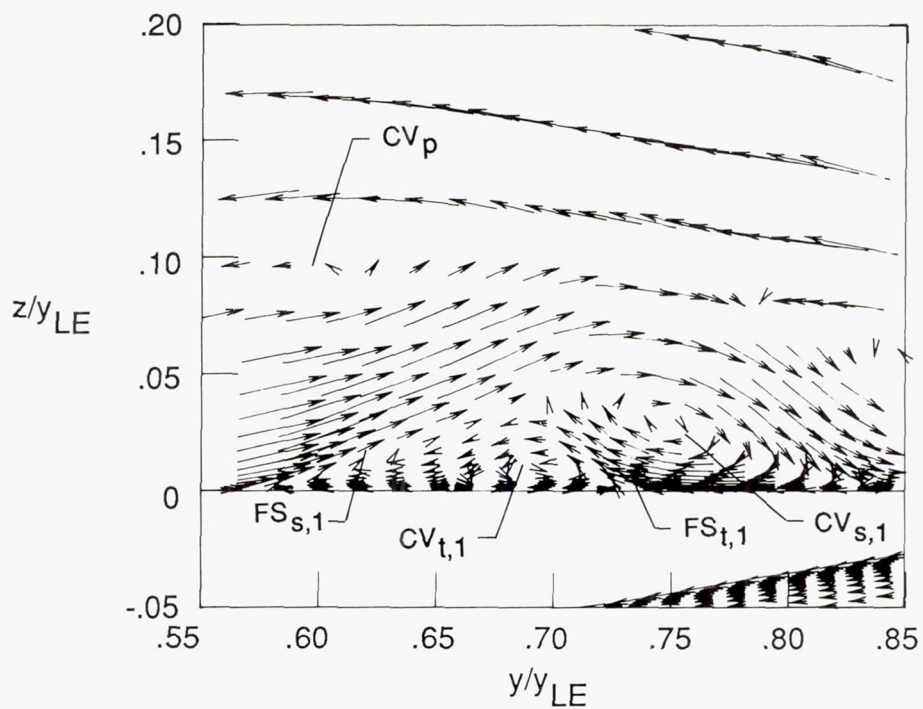
(b) Cross-flow velocity vectors.

Figure 20. A close-up view of the most inboard secondary vortex from the conical laminar Navier-Stokes solution for $\Lambda = 75°$, $\alpha = 8°$, and $M = 2.8$.
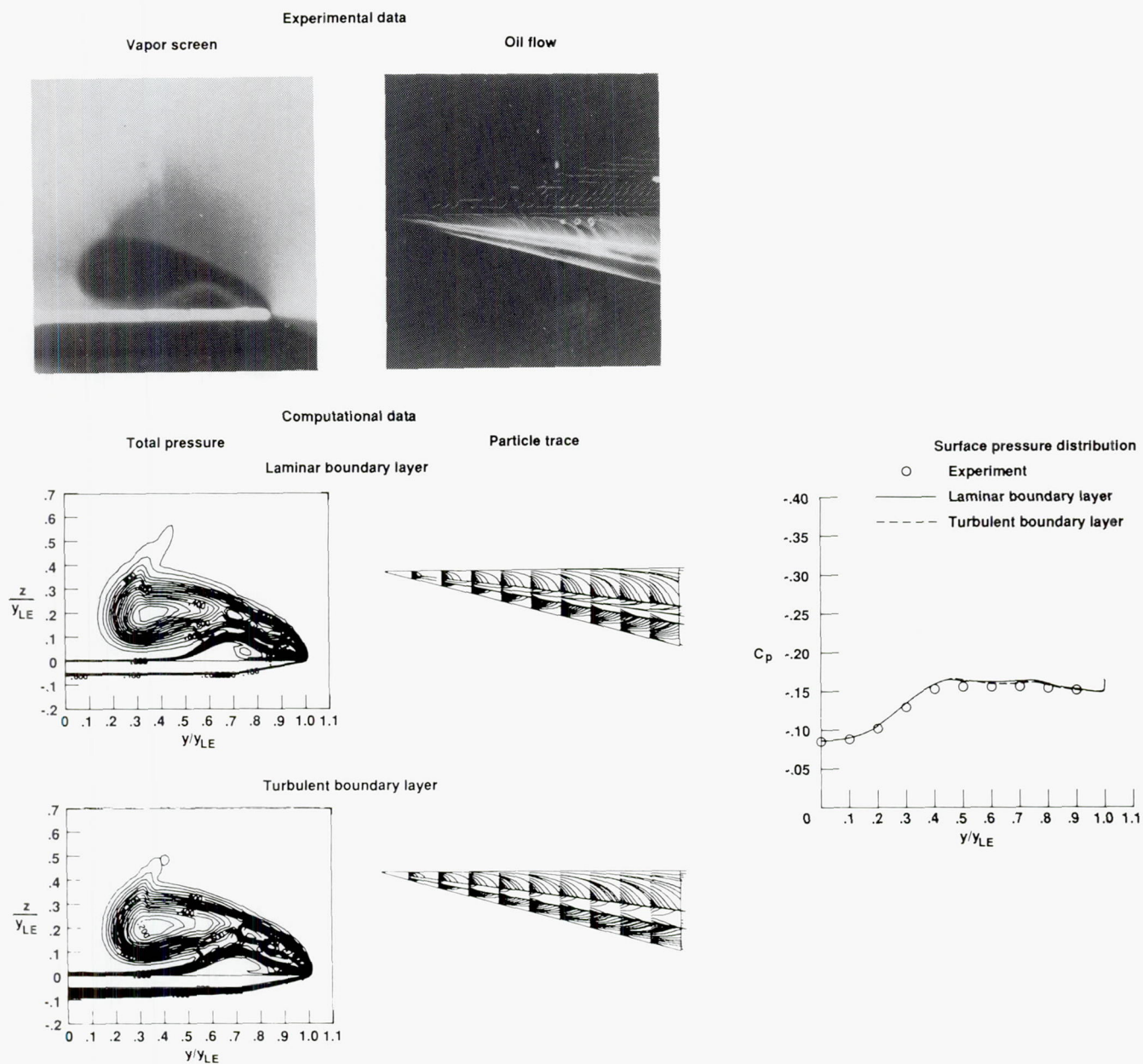
Figure 21. Comparison of experimental and conical Navier-Stokes computational data for $\Lambda = 75°$, $\alpha = 16°$, and $M = 2.8$.
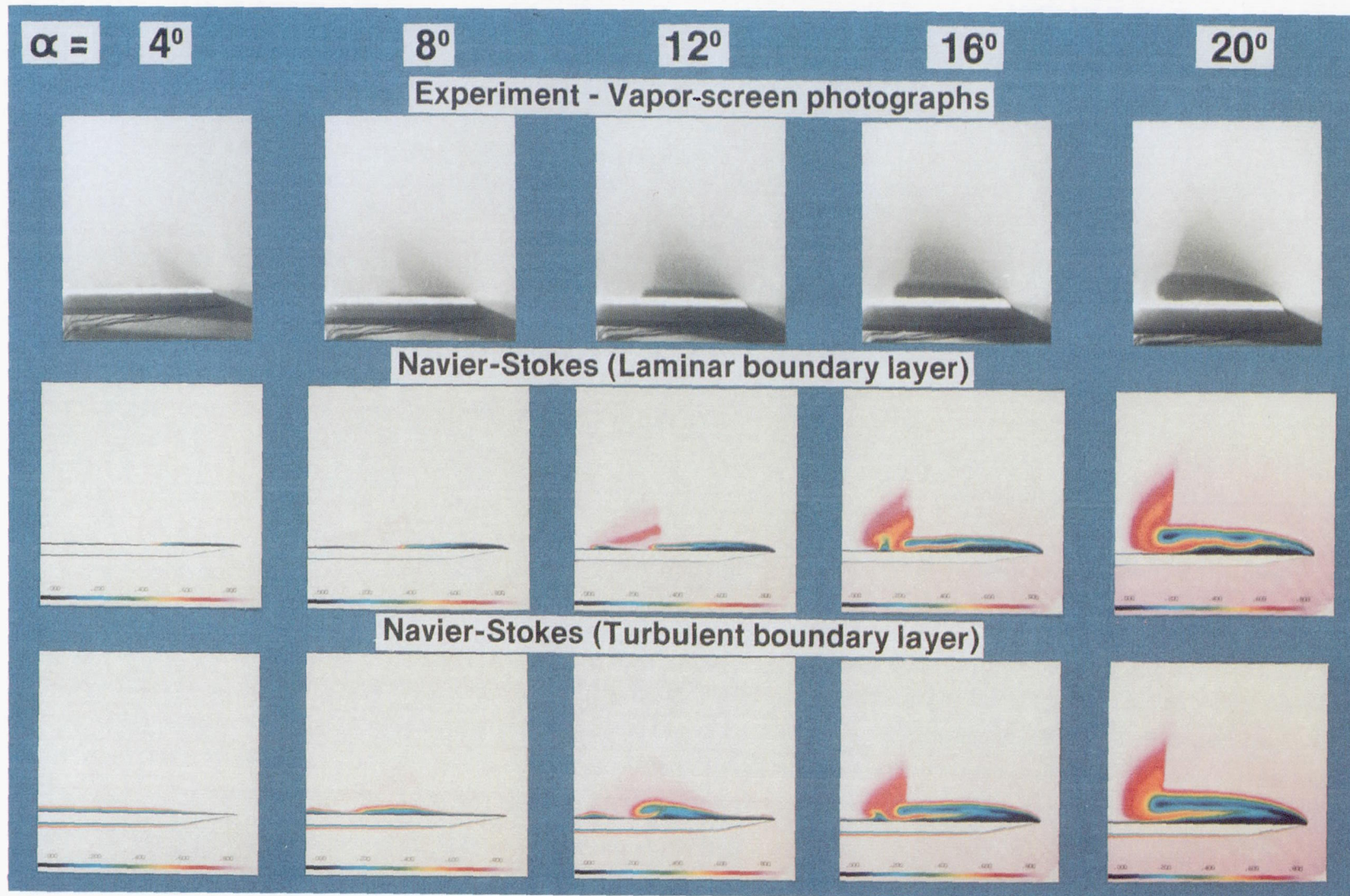
(a) Total pressure ratio.

Figure 22. Vapor-screen photographs and conical Navier-Stokes color contour data for the 67.5° delta wing at $M = 2.8$ and $\alpha = 4°$, 8°, 12°, 16°, and 20°.
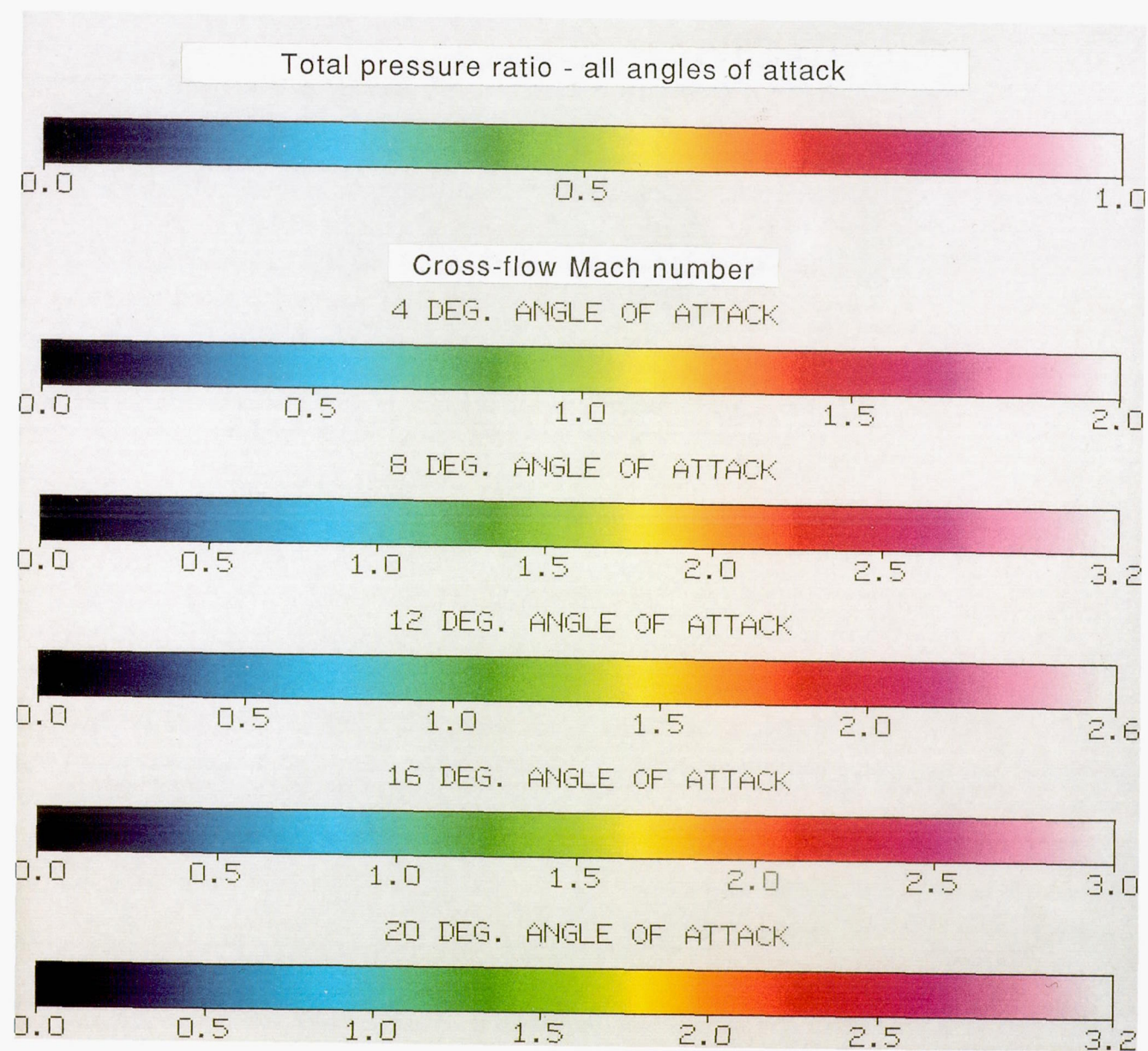
α = 4°   8°   12°   16°   20°

Experiment - Vapor-screen photographs

Navier-Stokes (Laminar boundary layer)

Navier-Stokes (Turbulent boundary layer)
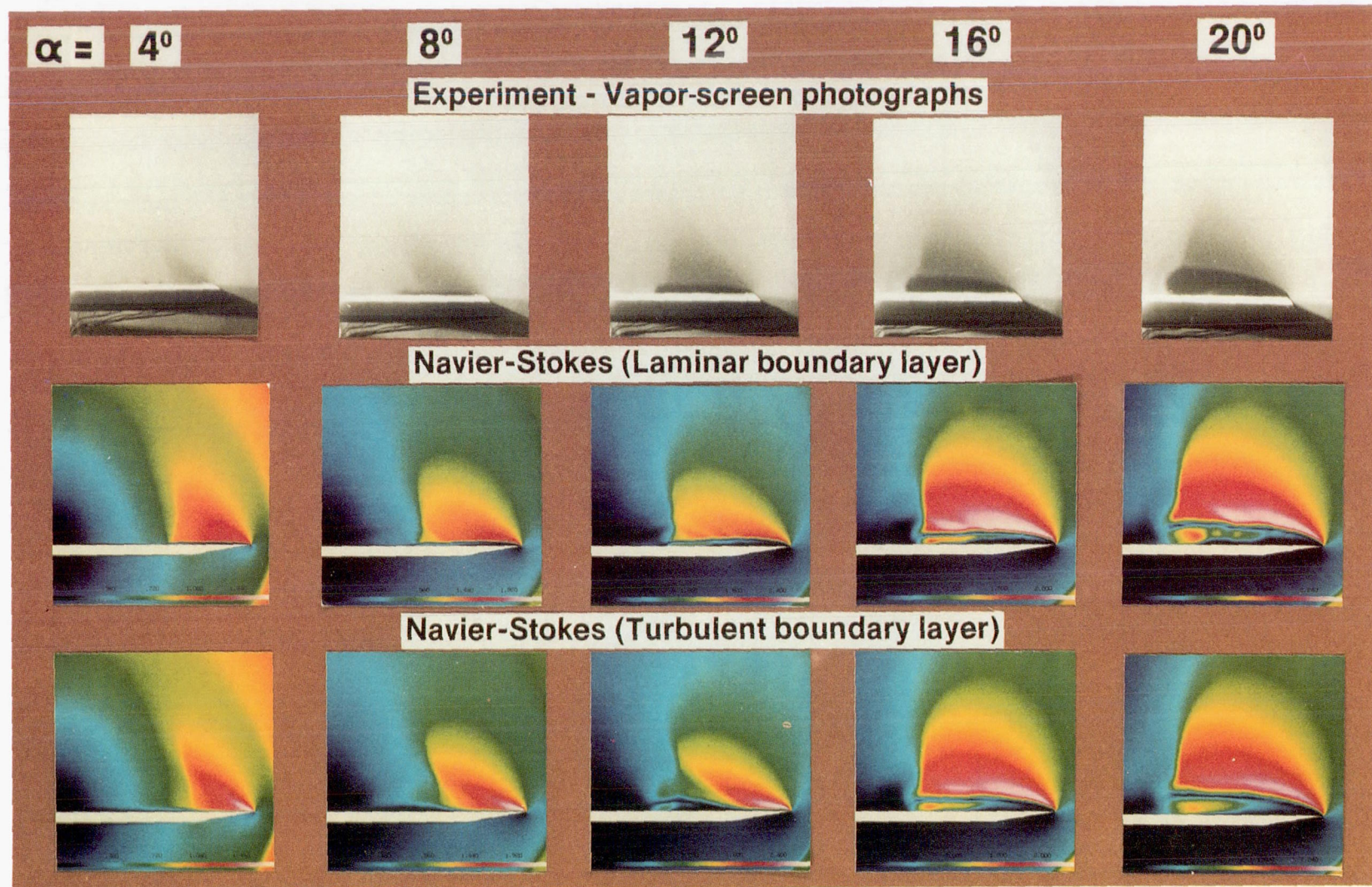
(b) Cross-flow Mach number.

Figure 22. Continued.
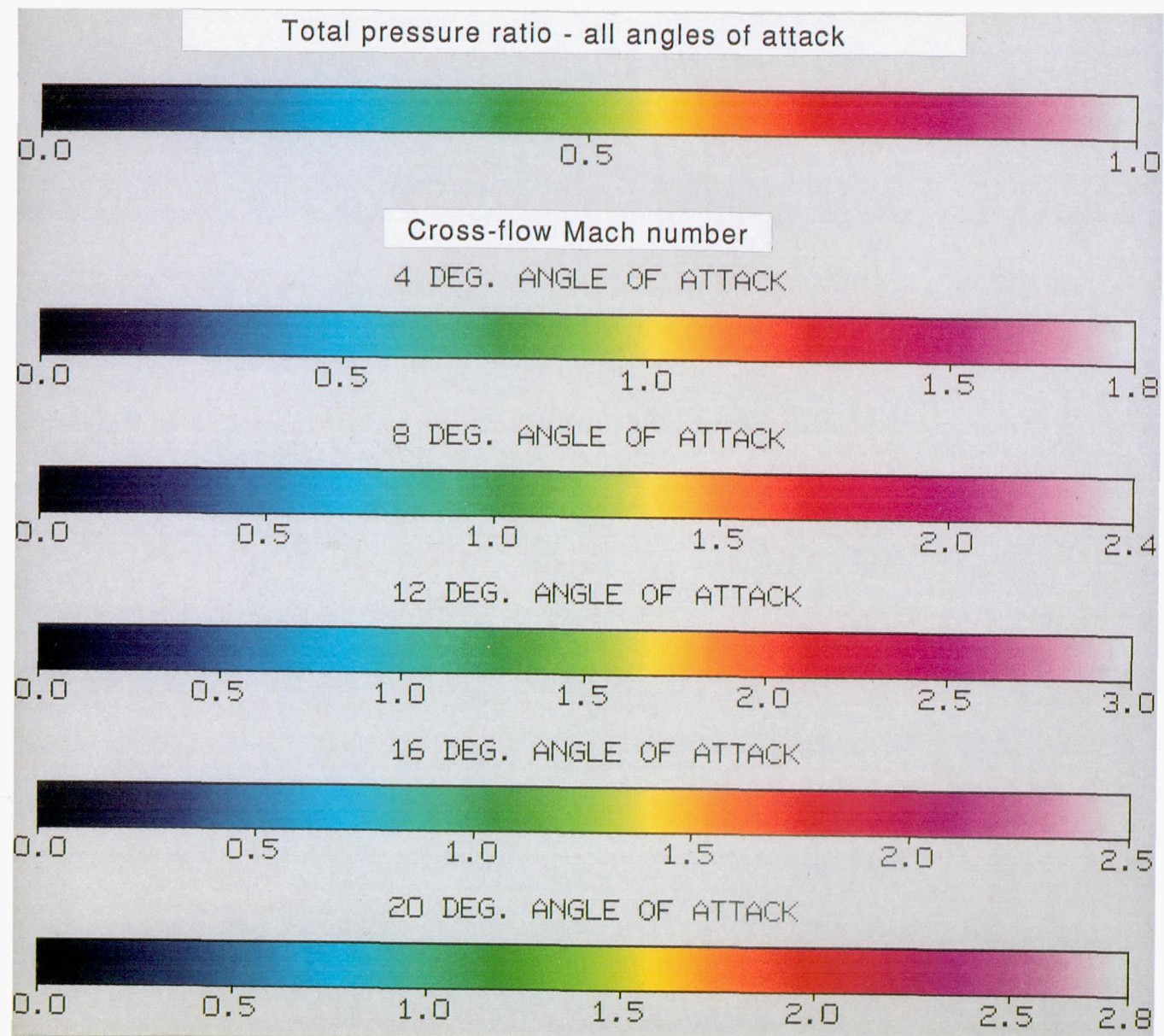
(c) Color bar definitions.

Figure 22. Concluded.
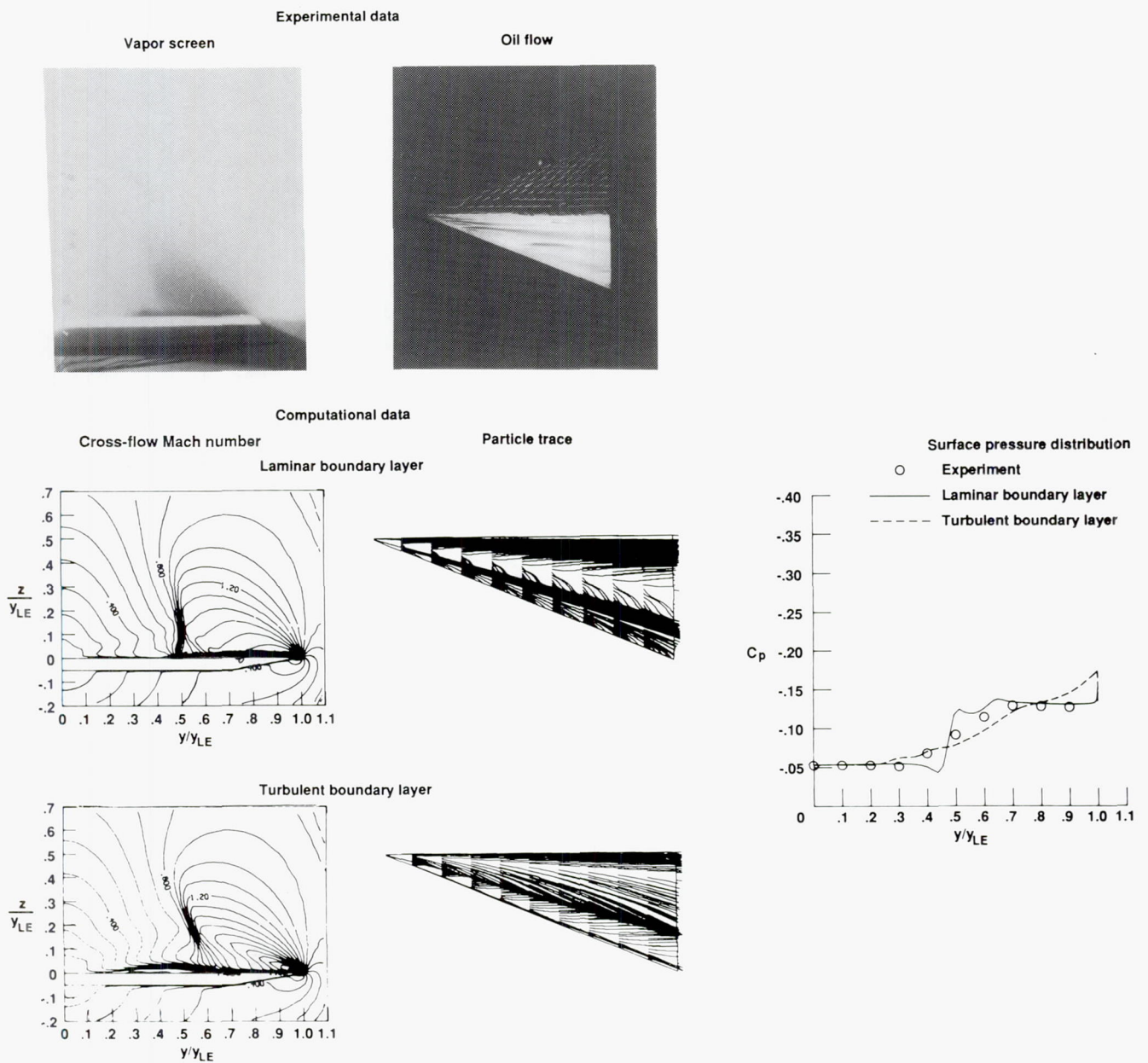
Figure 23. Comparison of experimental and conical Navier-Stokes computational data for $\Lambda = 67.5°$, $\alpha = 8°$, and $M = 2.8$.
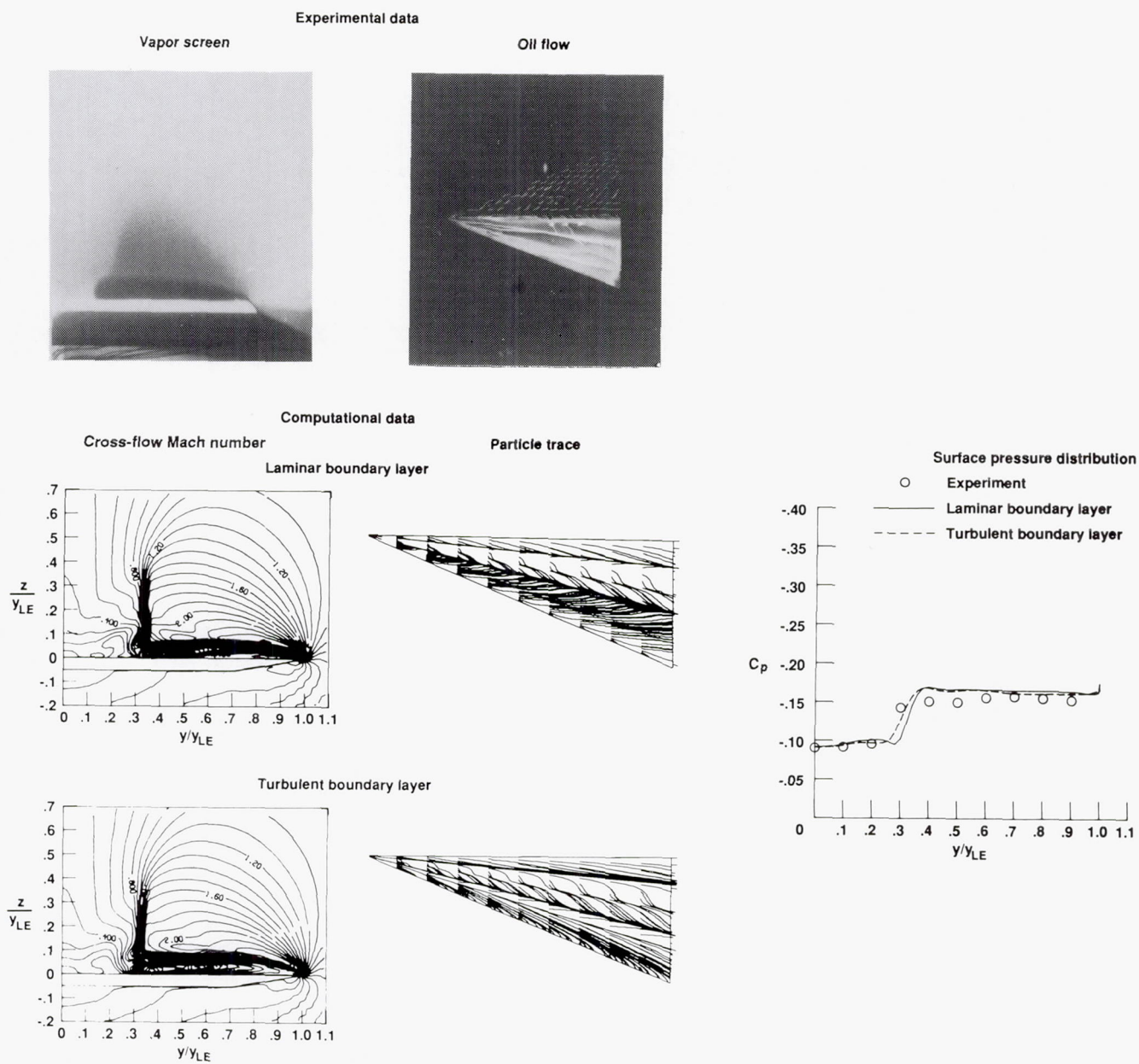
Figure 24. Comparison of experimental and conical Navier-Stokes computational data for $\Lambda = 67.5°$, $\alpha = 16°$, and $M = 2.8$.

α =   4⁰   8⁰   12⁰   16⁰   20⁰

Experiment - Vapor-screen photographs

Navier-Stokes (Laminar boundary layer)

Navier-Stokes (Turbulent boundary layer)
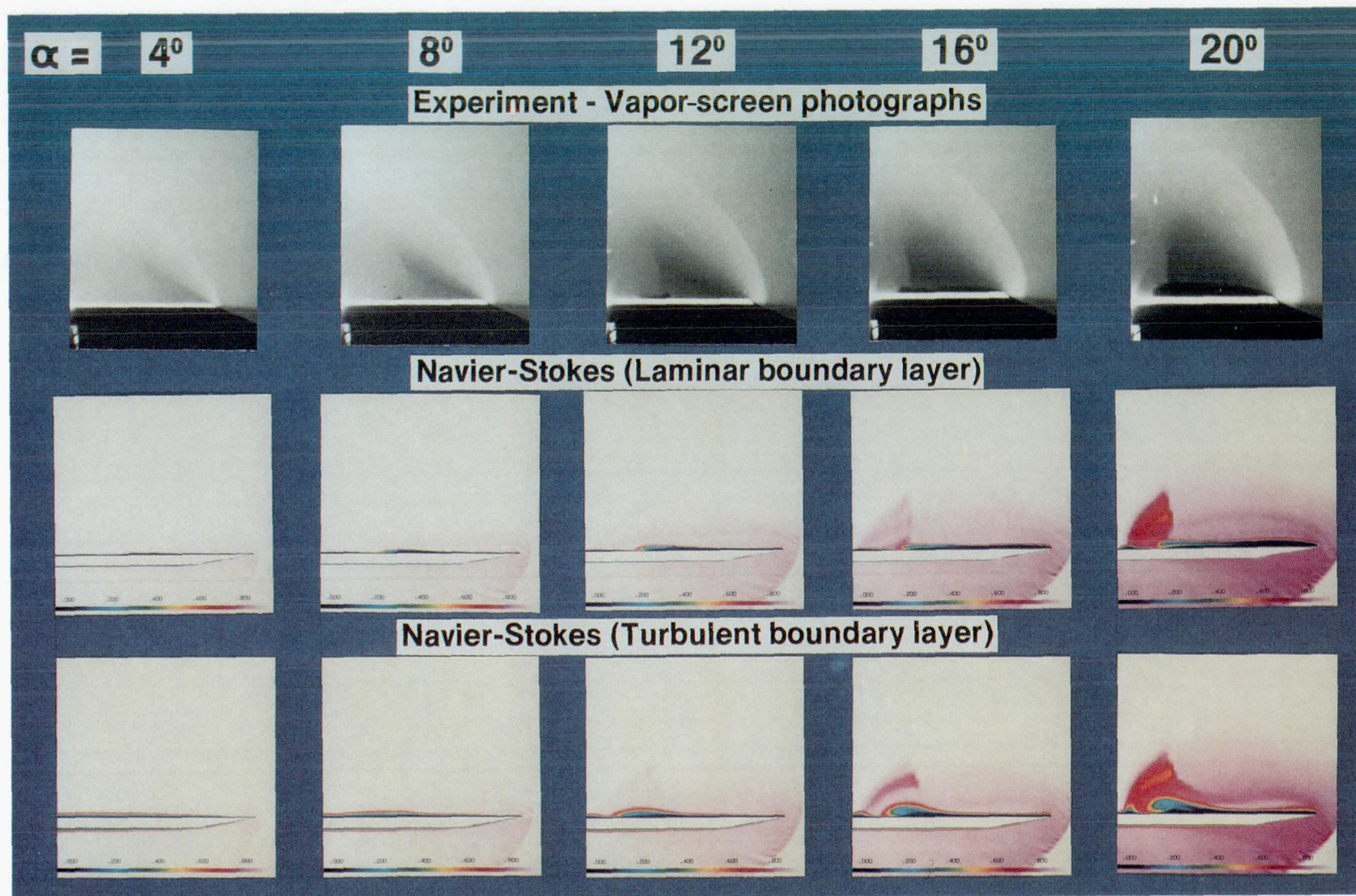
(a) Total pressure ratio.

Figure 25. Vapor-screen photographs and conical Navier-Stokes color contour data for the 60° delta wing at $M = 2.8$ and $\alpha = 4°$, $8°$, $12°$, $16°$, and $20°$.
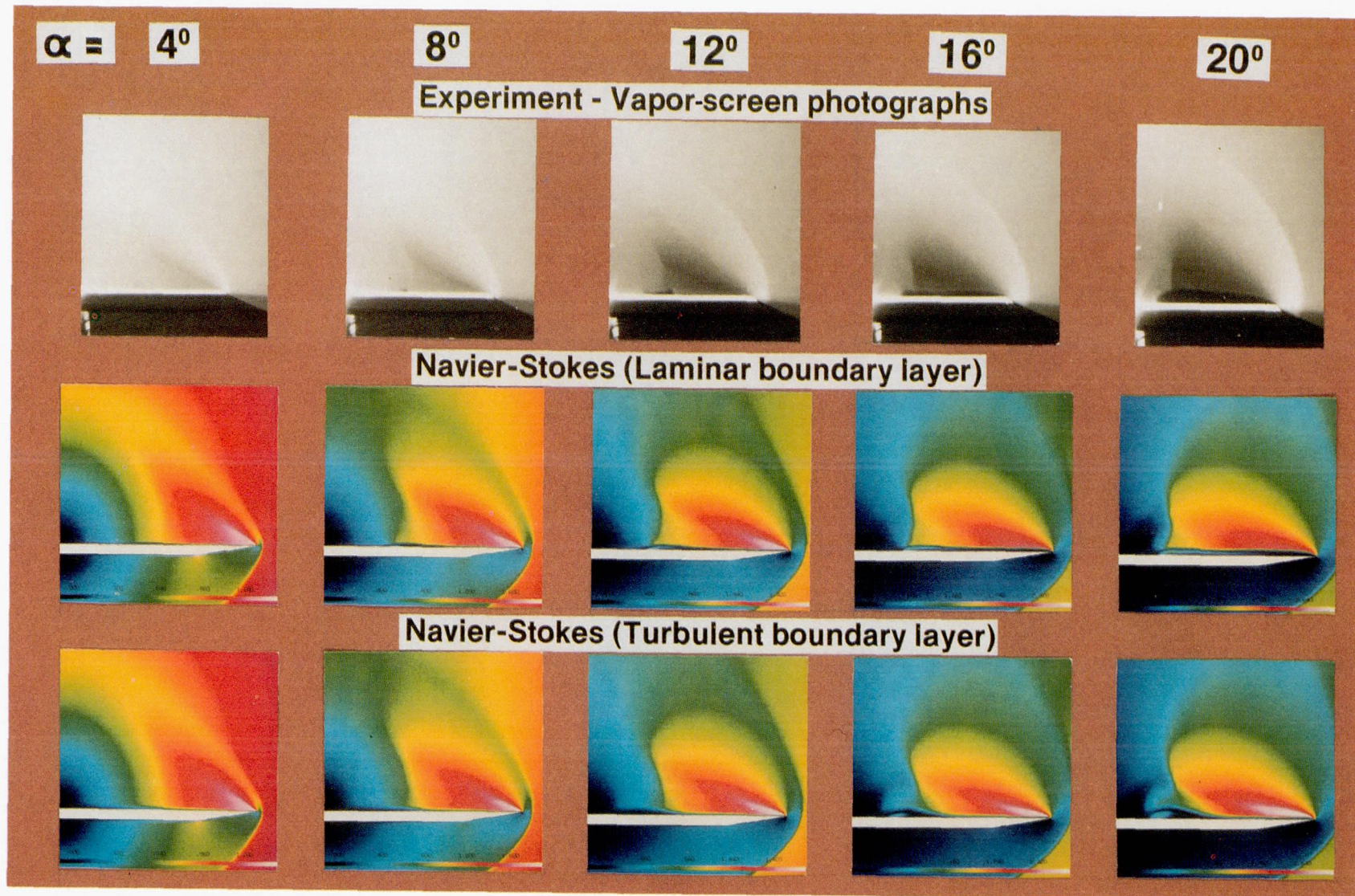
(b) Cross-flow Mach number.

Figure 25. Continued.
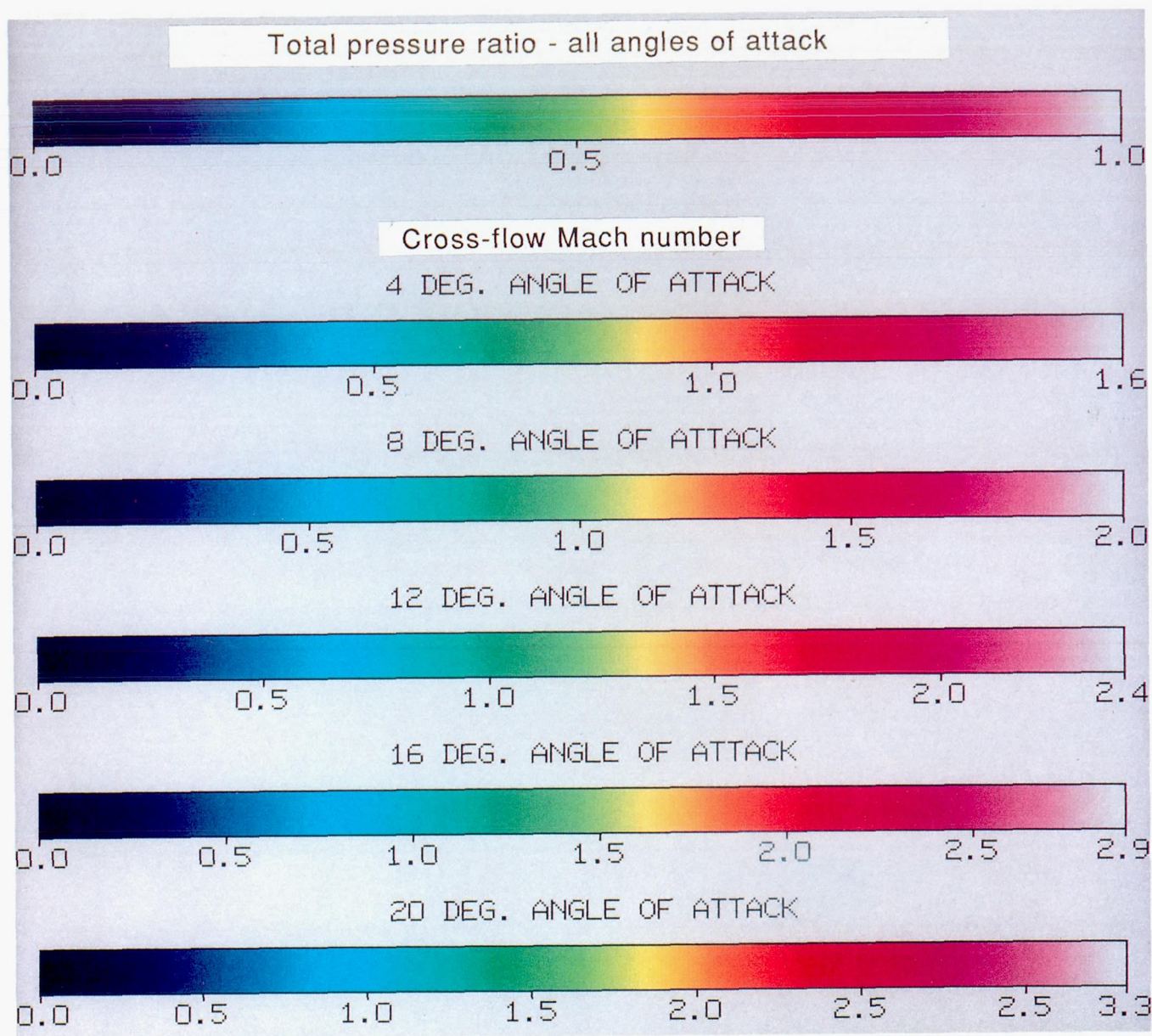
(c) Color bar definitions.

Figure 25. Concluded.
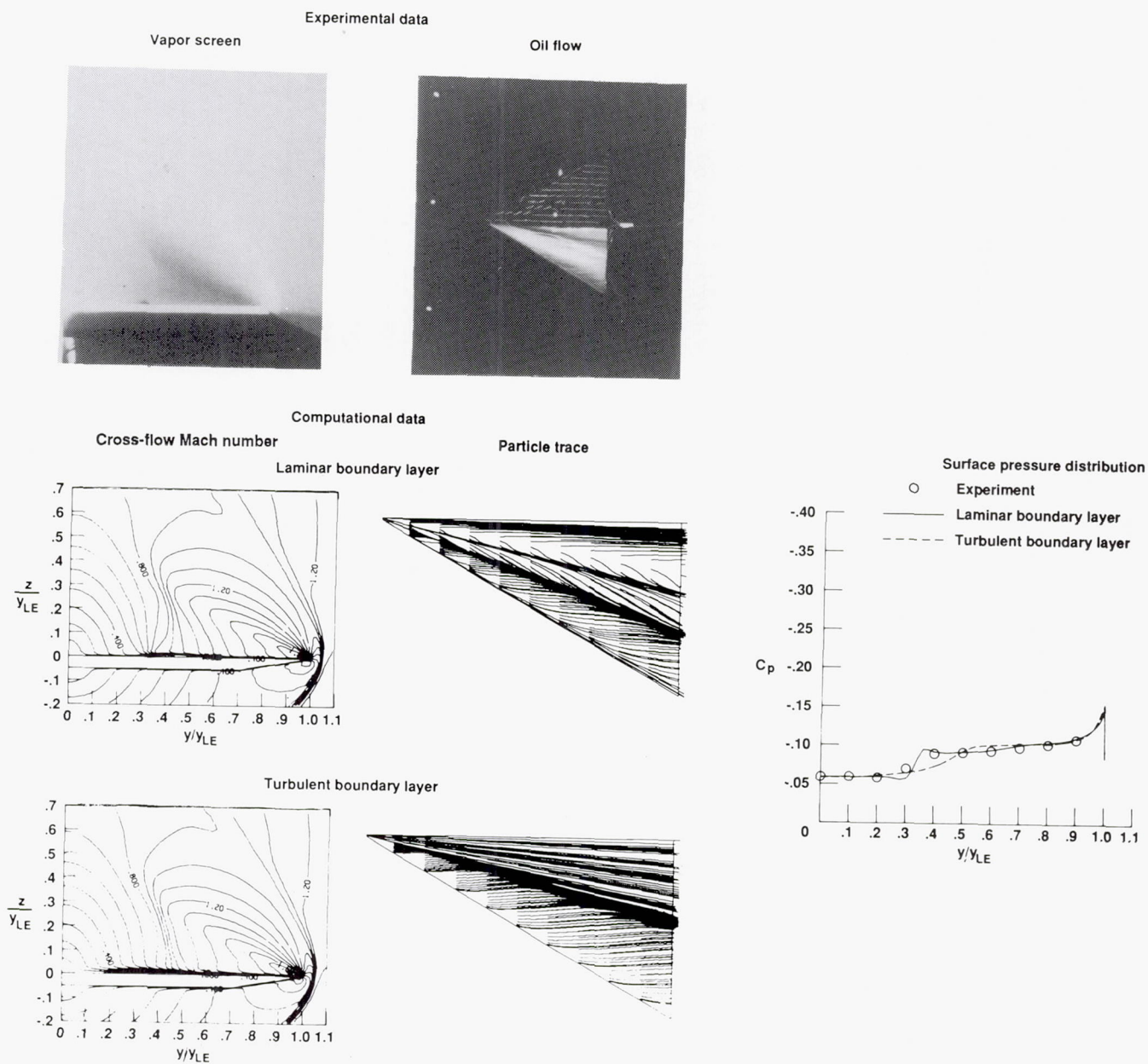
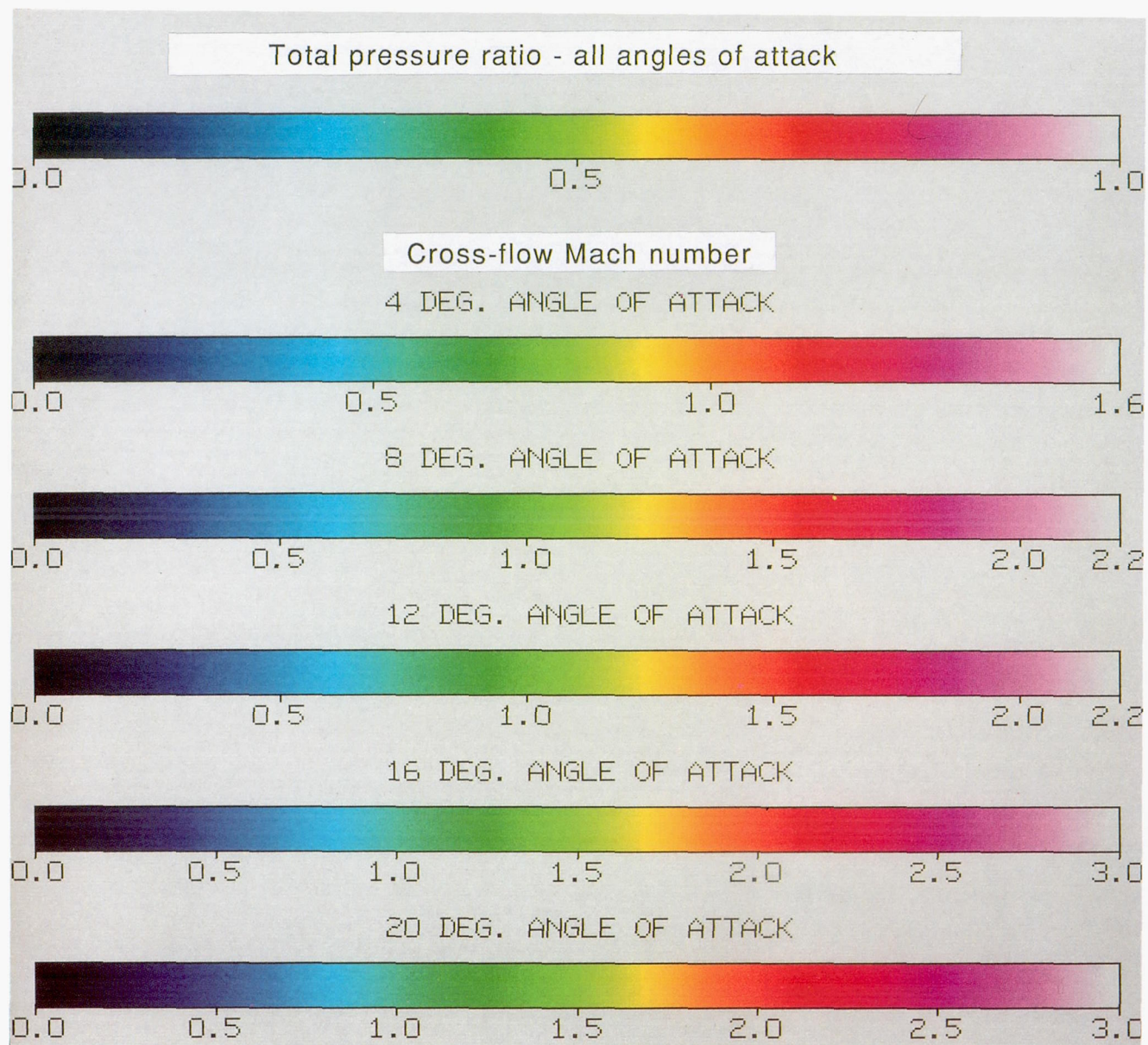Figure 26. Comparison of experimental and conical Navier-Stokes computational data for $\Lambda = 60°$, $\alpha = 8°$, and $M = 2.8$.
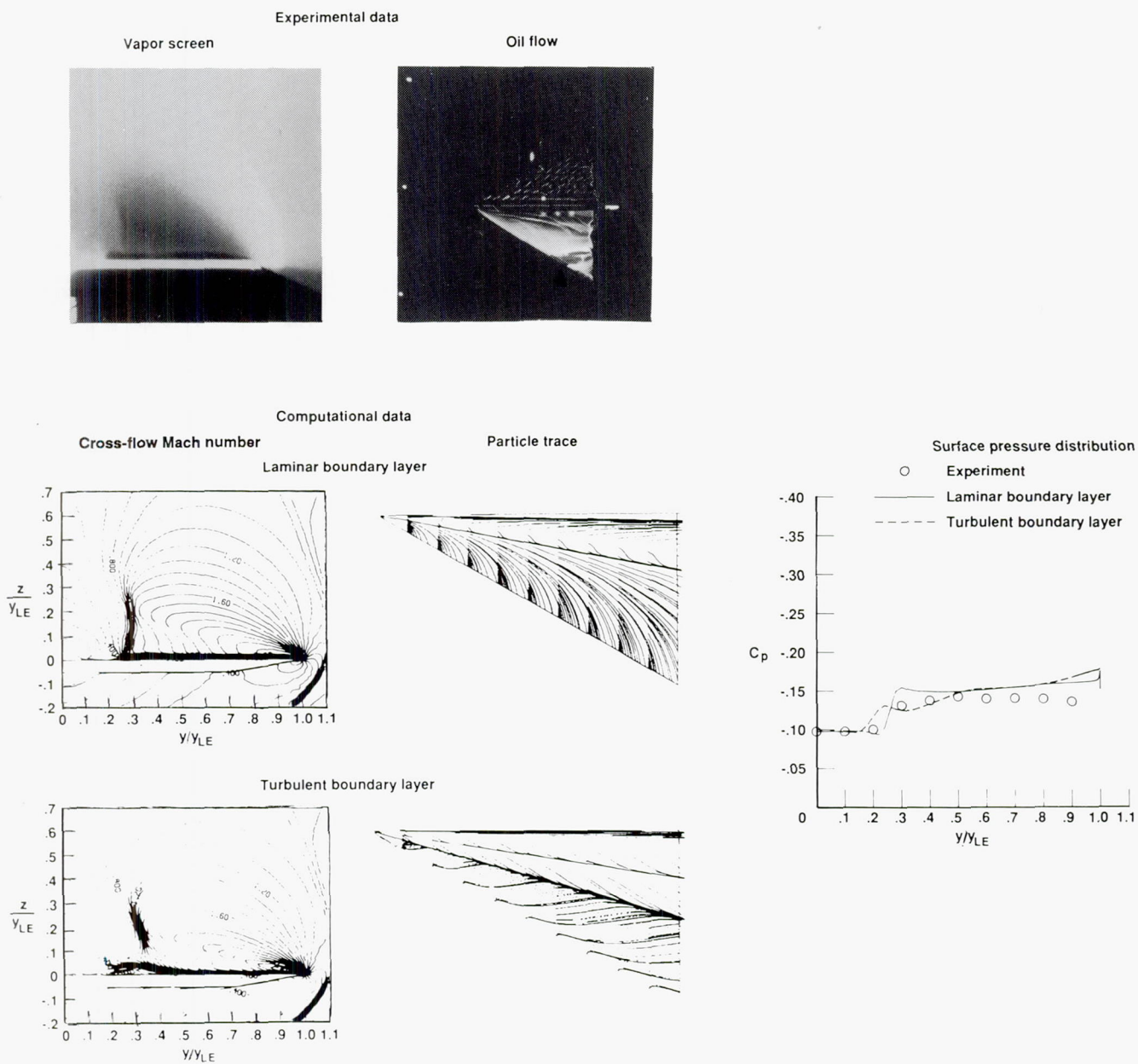
Figure 27. Comparison of experimental and conical Navier-Stokes computational data for $\Lambda = 60°$, $\alpha = 16°$, and $M = 2.8$.
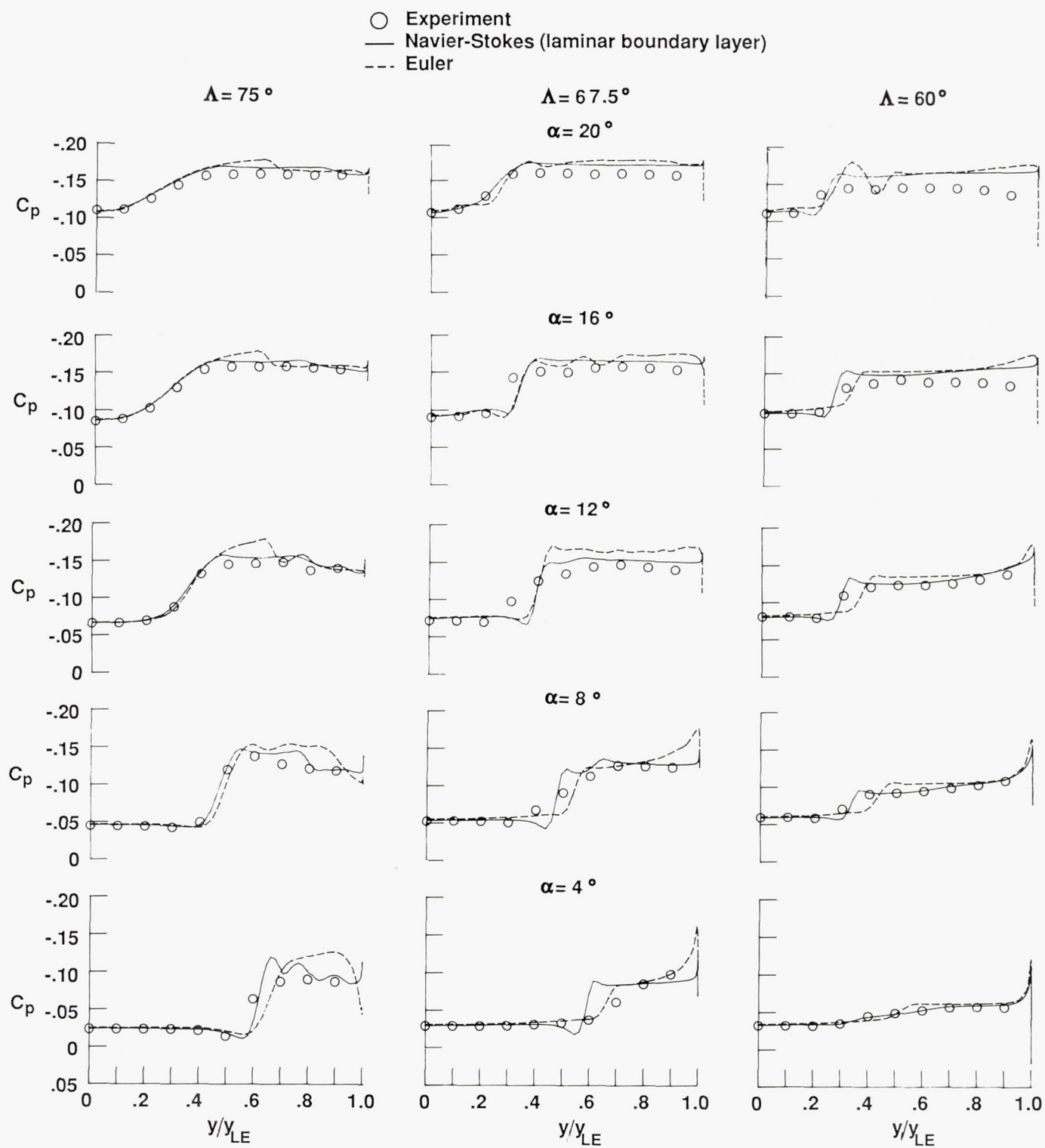
Figure 28. Comparison of experimental, conical laminar Navier-Stokes, and conical Euler computational surface pressure distributions for the 15 test cases.

α = 4° 8° 12° 16° 20°

Experiment - Vapor-screen photographs

Navier-Stokes (Laminar boundary layer)
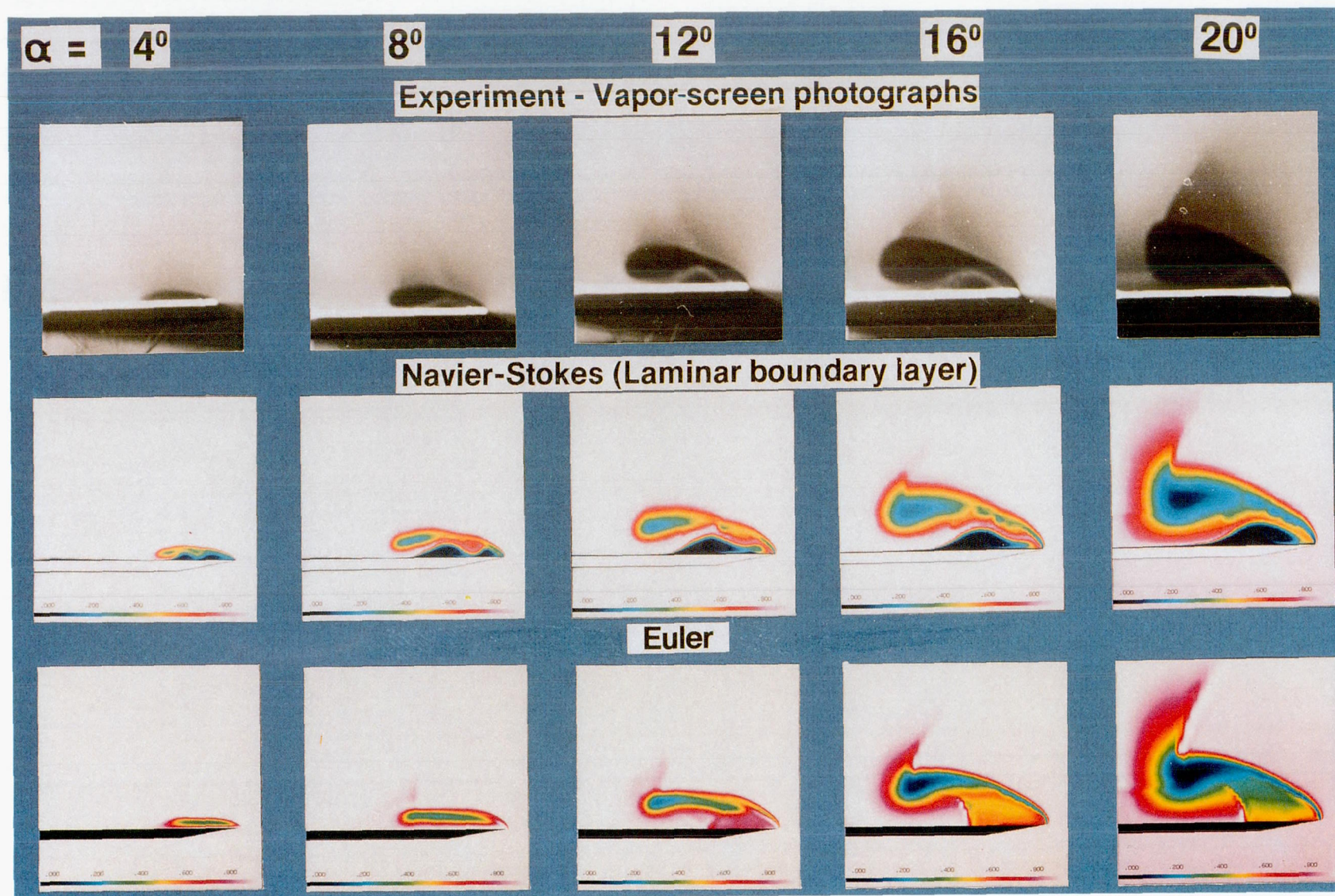
Euler

(a) Total pressure ratio.

Figure 29. Vapor-screen photographs and conical laminar Navier-Stokes and conical Euler color contours for the 75° delta wing at $M = 2.8$ and $\alpha = 4°$, 8°, 12°, 16°, and 20°.

(b) Cross-flow Mach number.

Figure 29. Continued.
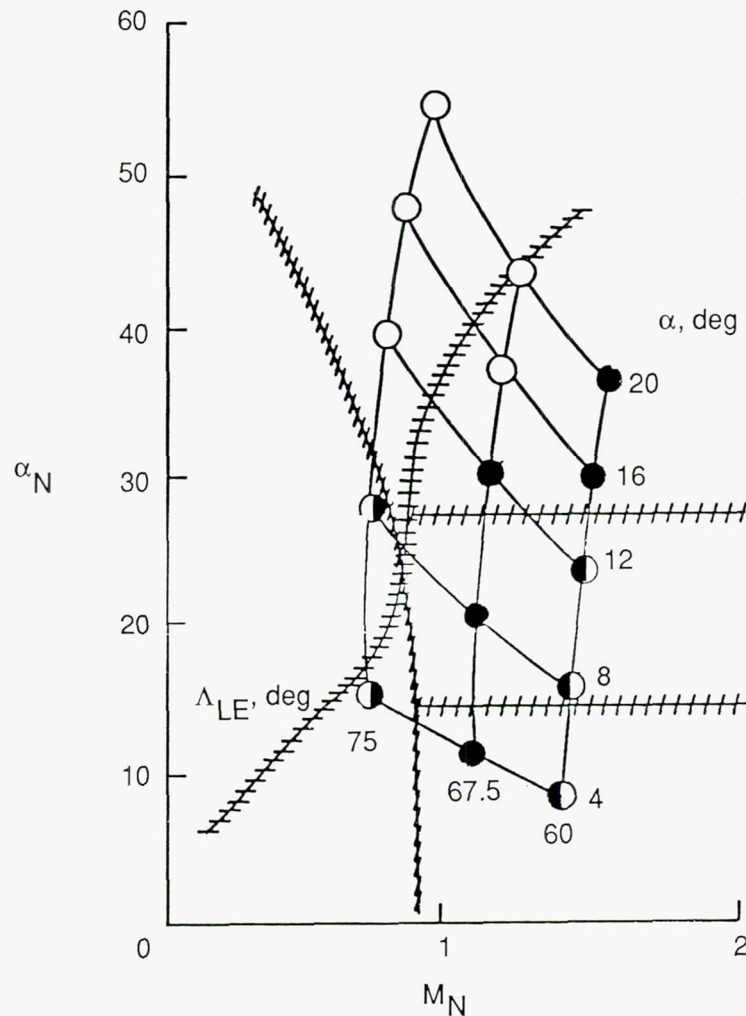
Total pressure ratio - all angles of attack

0.0   0.5   1.0

Cross-flow Mach number

4 DEG. ANGLE OF ATTACK

0.0   0.5   1.0   1.6

8 DEG. ANGLE OF ATTACK

0.0   0.5   1.0   1.5   1.9

12 DEG. ANGLE OF ATTACK

0.0   0.5   1.0   1.5   2.0   2.4

16 DEG. ANGLE OF ATTACK

0.0   0.5   1.0   1.5   2.0   2.5

20 DEG. ANGLE OF ATTACK

0.0   0.5   1.0   1.5   2.0   2.5   2.9

(c) Color bar definitions.

Figure 29. Concluded.
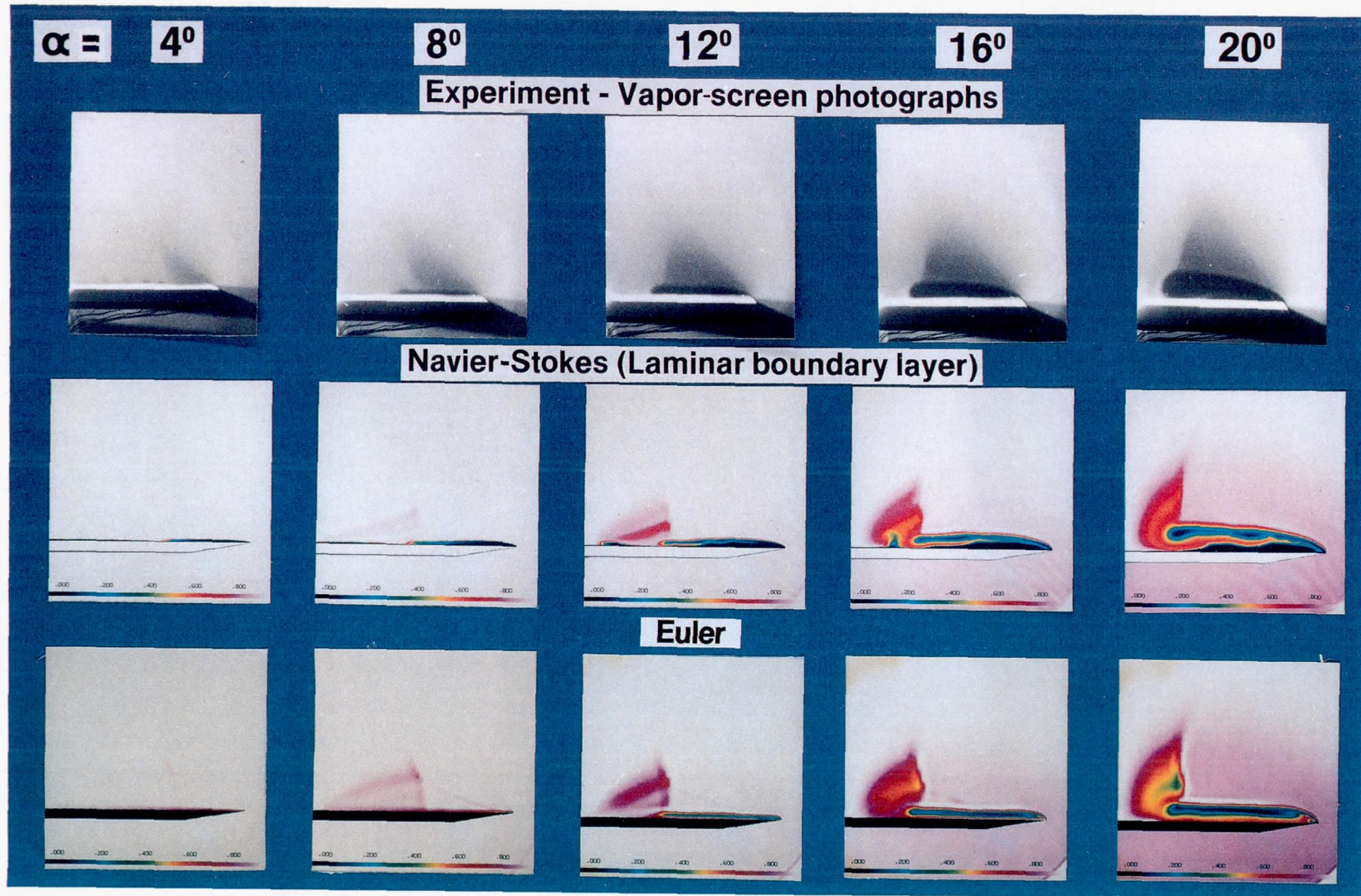
(a) Total pressure ratio.

Figure 30. Vapor-screen photographs and conical laminar Navier-Stokes and conical Euler color contours for the 67.5° delta wing at $M = 2.8$ and $\alpha = 4°$, 8°, 12°, 16°, and 20°.

α = 4⁰   8⁰   12⁰   16⁰   20⁰

Experiment - Vapor-screen photographs

Navier-Stokes (Laminar boundary layer)
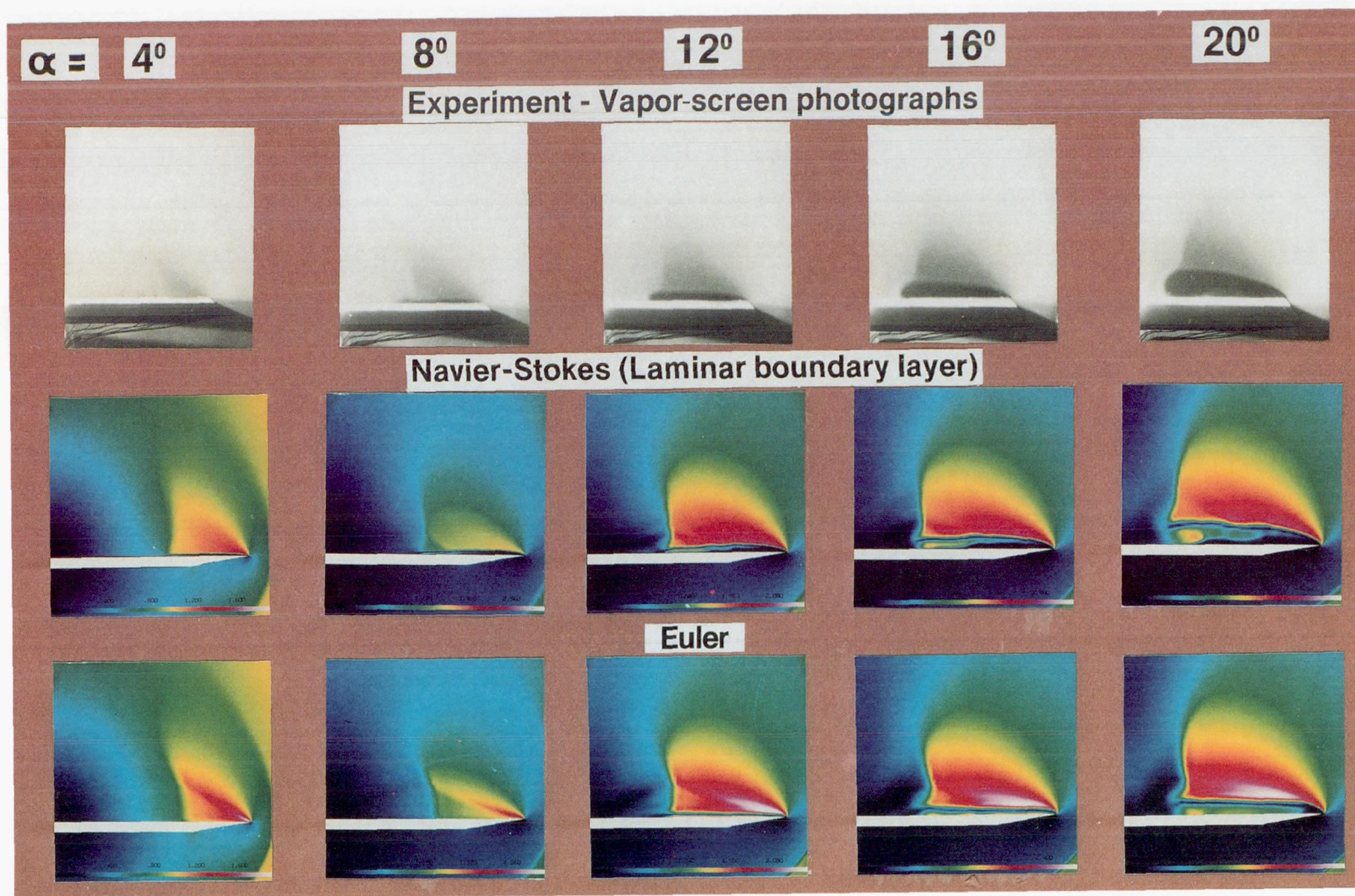
Euler

(b) Cross-flow Mach number.

Figure 30. Continued.

(c) Color bar definitions.

Figure 30. Concluded.
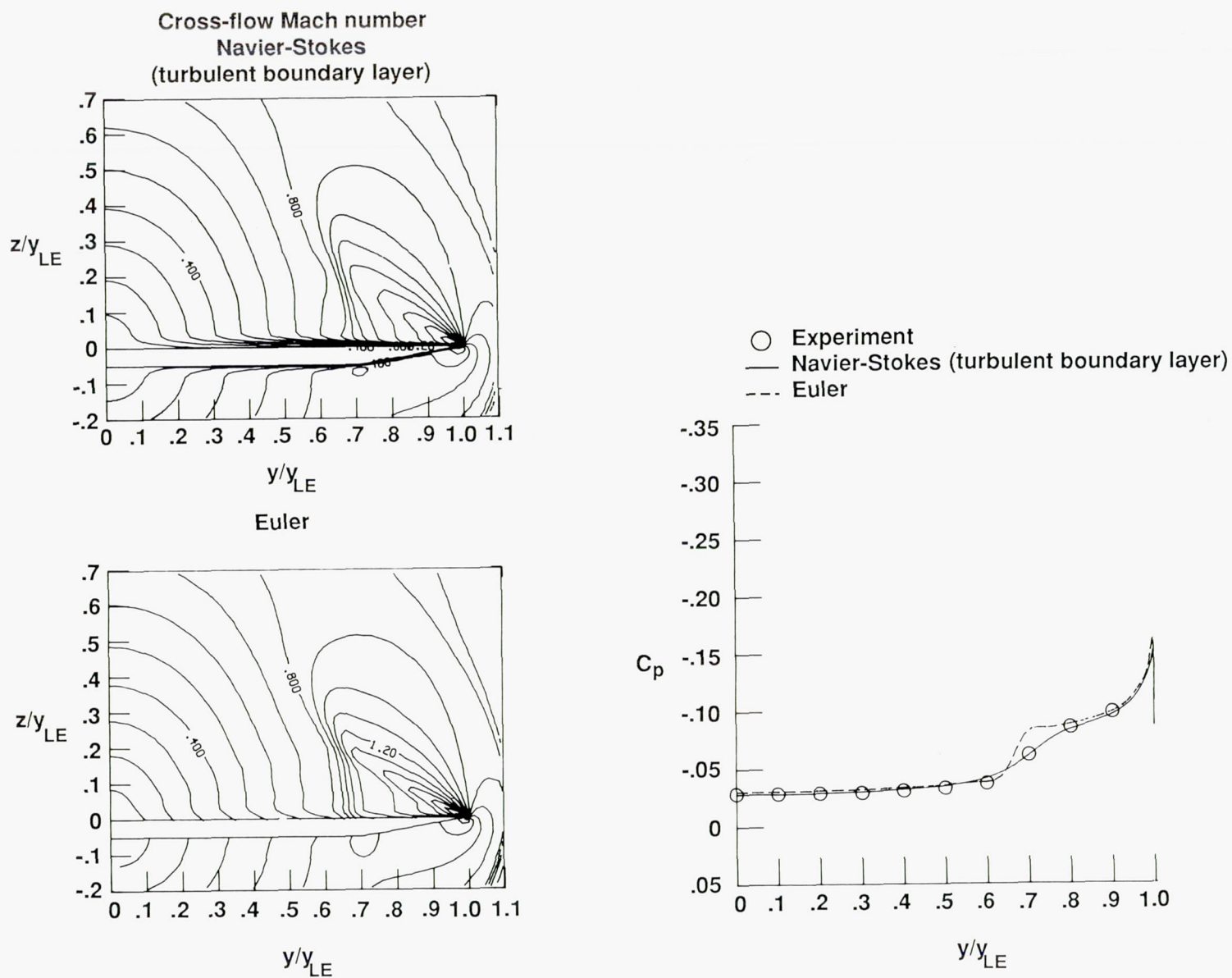
Figure 31. Comparison of experimental data and conical laminar Navier-Stokes and conical Euler computational data for $\Lambda = 67.5°$, $\alpha = 4°$, and $M = 2.8$.
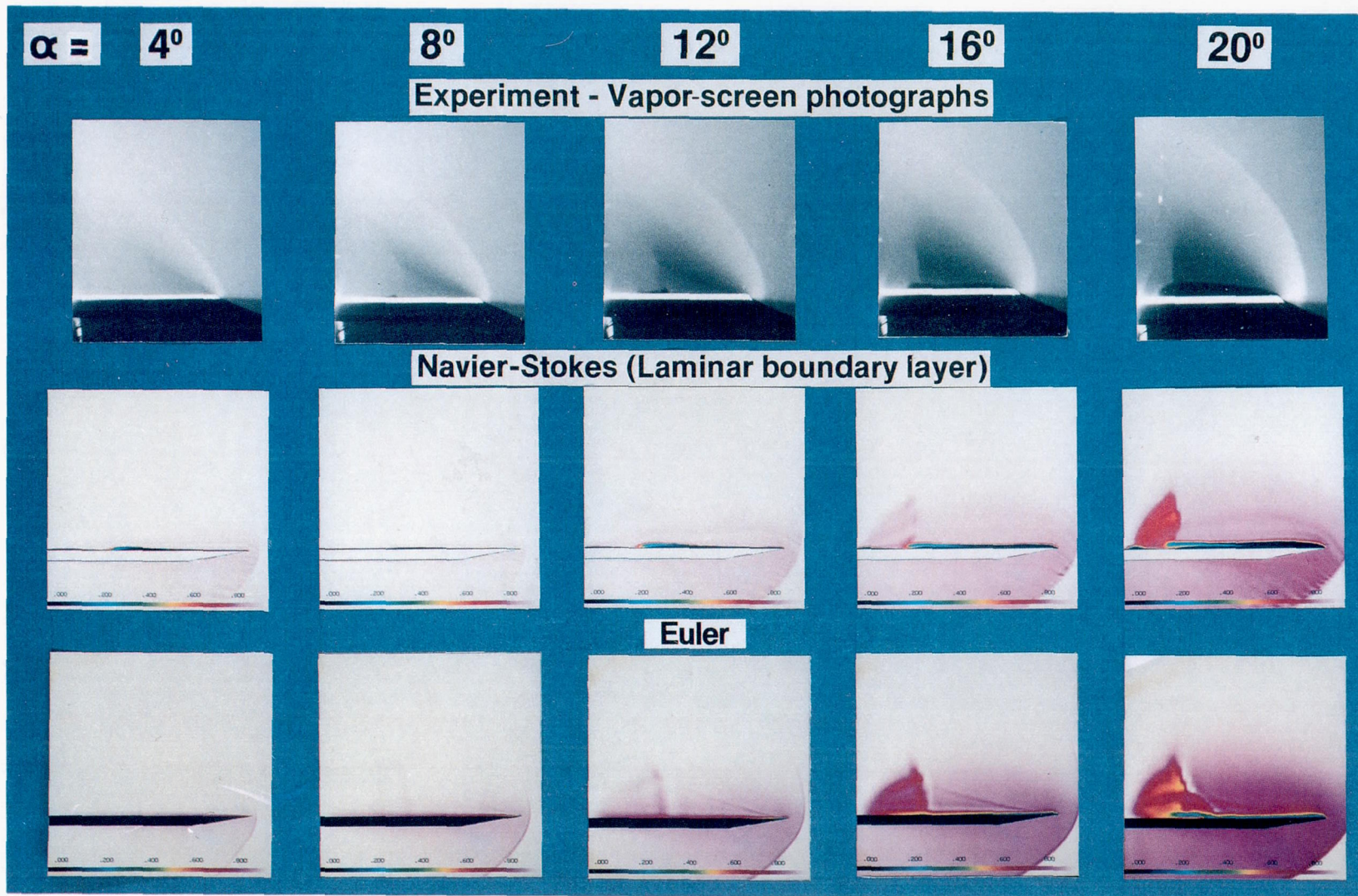
(a) Total pressure ratio.

Figure 32. Vapor-screen photographs and conical laminar Navier-Stokes and conical Euler color contours for the 60° delta wing at $M = 2.8$ and $\alpha = 4°$, 8°, 12°, 16°, and 20°.
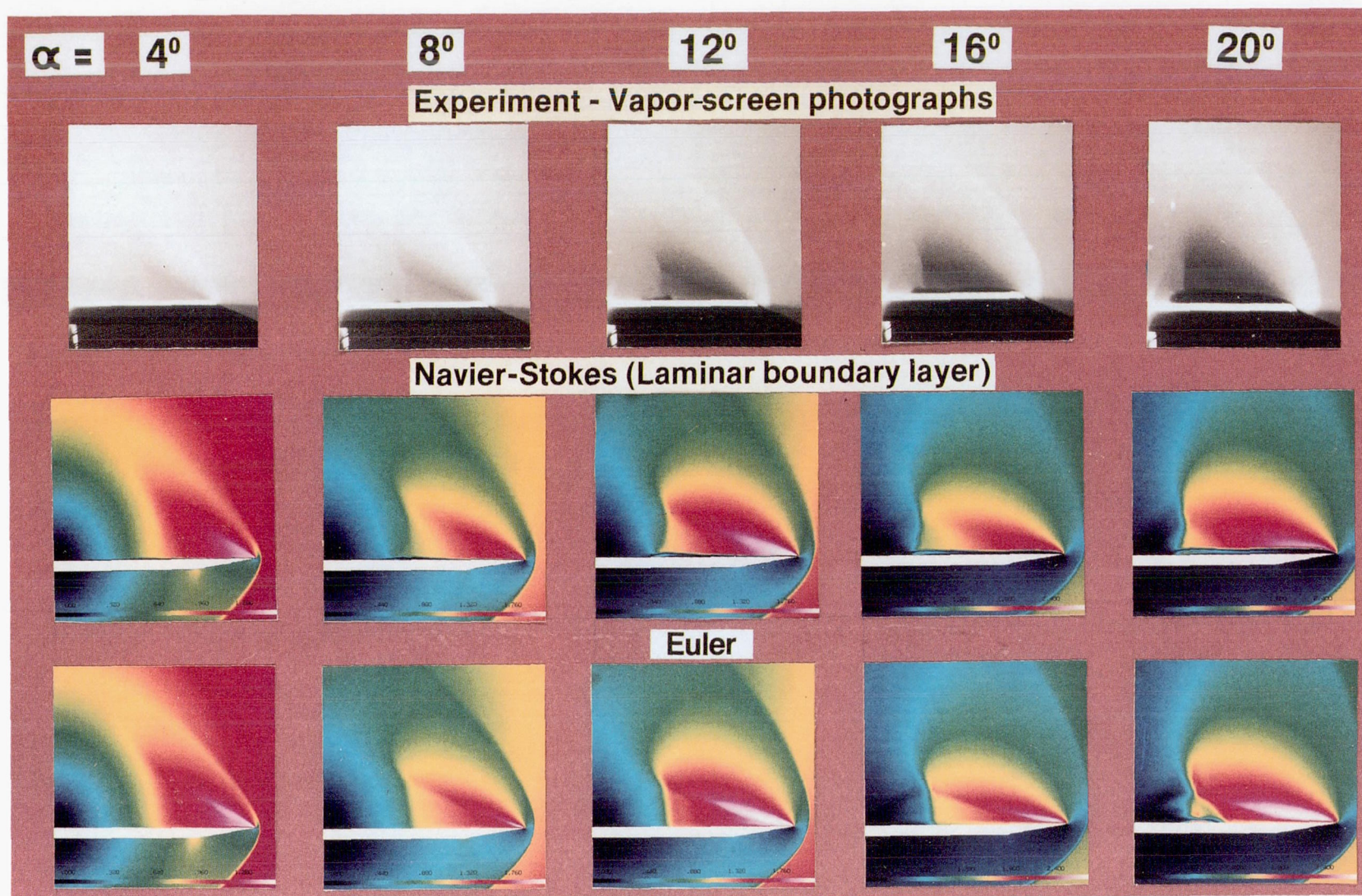
(b) Cross-flow Mach number.

Figure 32. Continued.

Total pressure ratio - all angles of attack

0.0   0.5   1.0

Cross-flow Mach number

4 DEG. ANGLE OF ATTACK

0.0   0.5   1.0   1.6

8 DEG. ANGLE OF ATTACK

0.0   0.5   1.0   1.5   2.0   2.2

12 DEG. ANGLE OF ATTACK

0.0   0.5   1.0   1.5   2.0   2.2

16 DEG. ANGLE OF ATTACK

0.0   0.5   1.0   1.5   2.0   2.5   3.0

20 DEG. ANGLE OF ATTACK

0.0   0.5   1.0   1.5   2.0   2.5   3.0

(c) Color bar definitions.

Figure 32. Concluded.

(a) Influence of boundary-layer model.

Figure 33. Summary of experimental, laminar Navier-Stokes, and turbulent Navier-Stokes data for the 15 test cases.
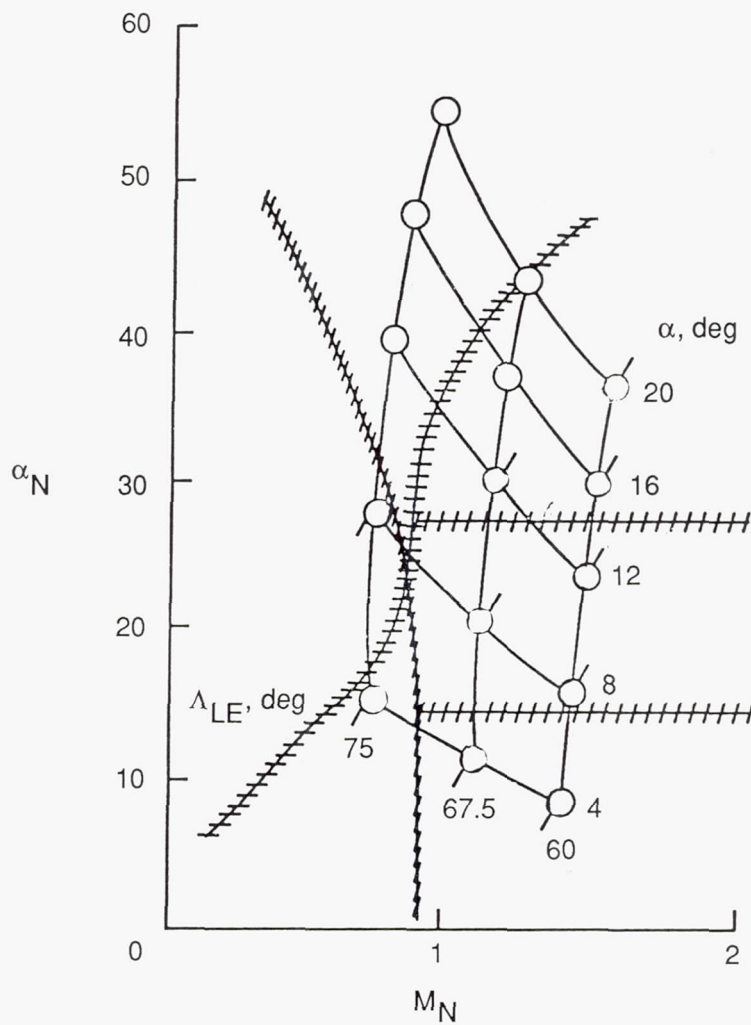
(b) Comparison with experiment.

Figure 33. Concluded.
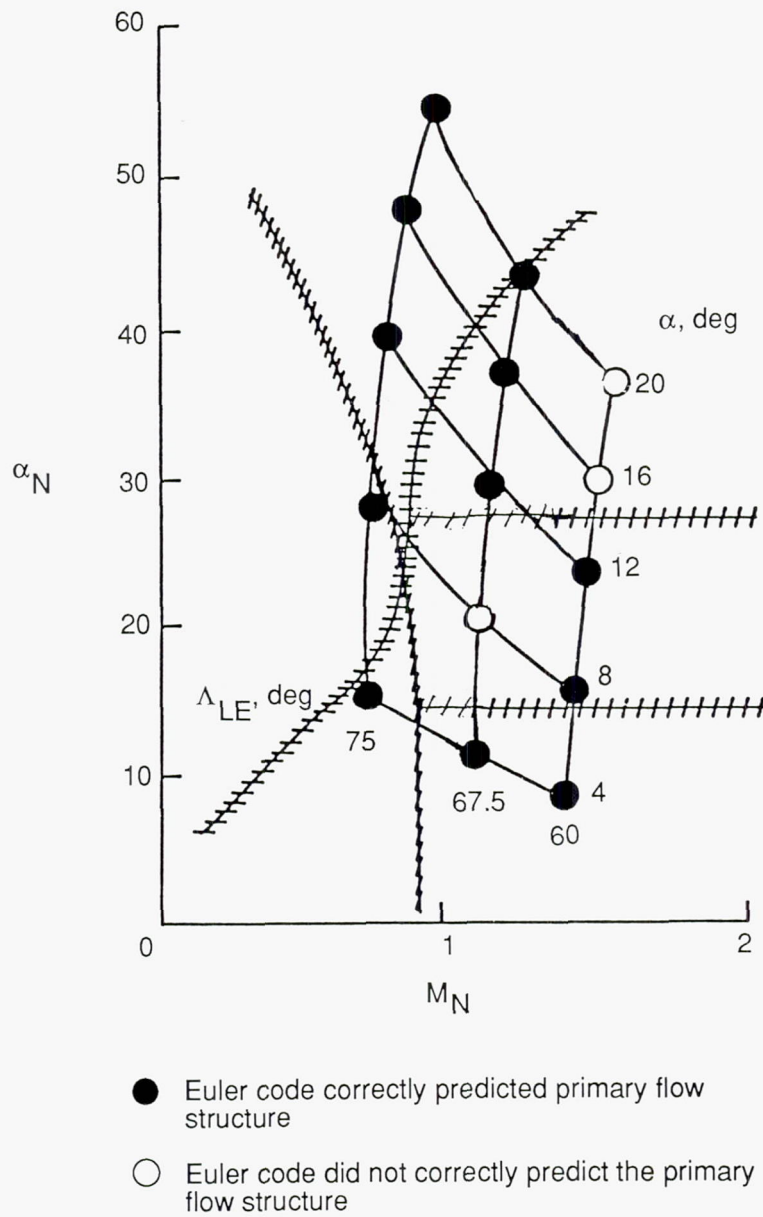
Figure 34. Summary of the experimental and Euler data for the 15 test cases.

Conditions where the Navier-Stokes and Euler codes are equivalent in prediction of primary flow structure
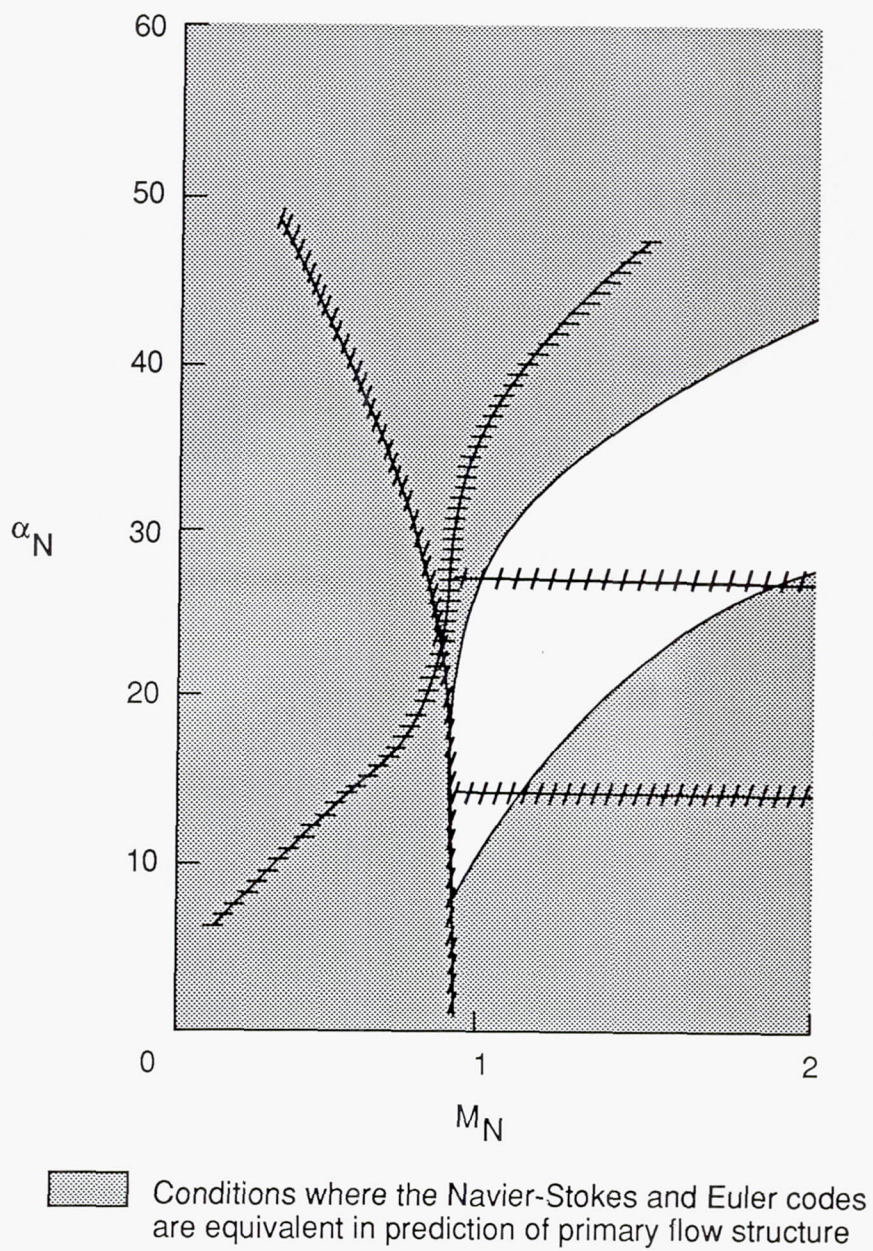
Figure 35. Summary of conditions at which the Navier-Stokes and Euler codes should be applied in supersonic wing design.
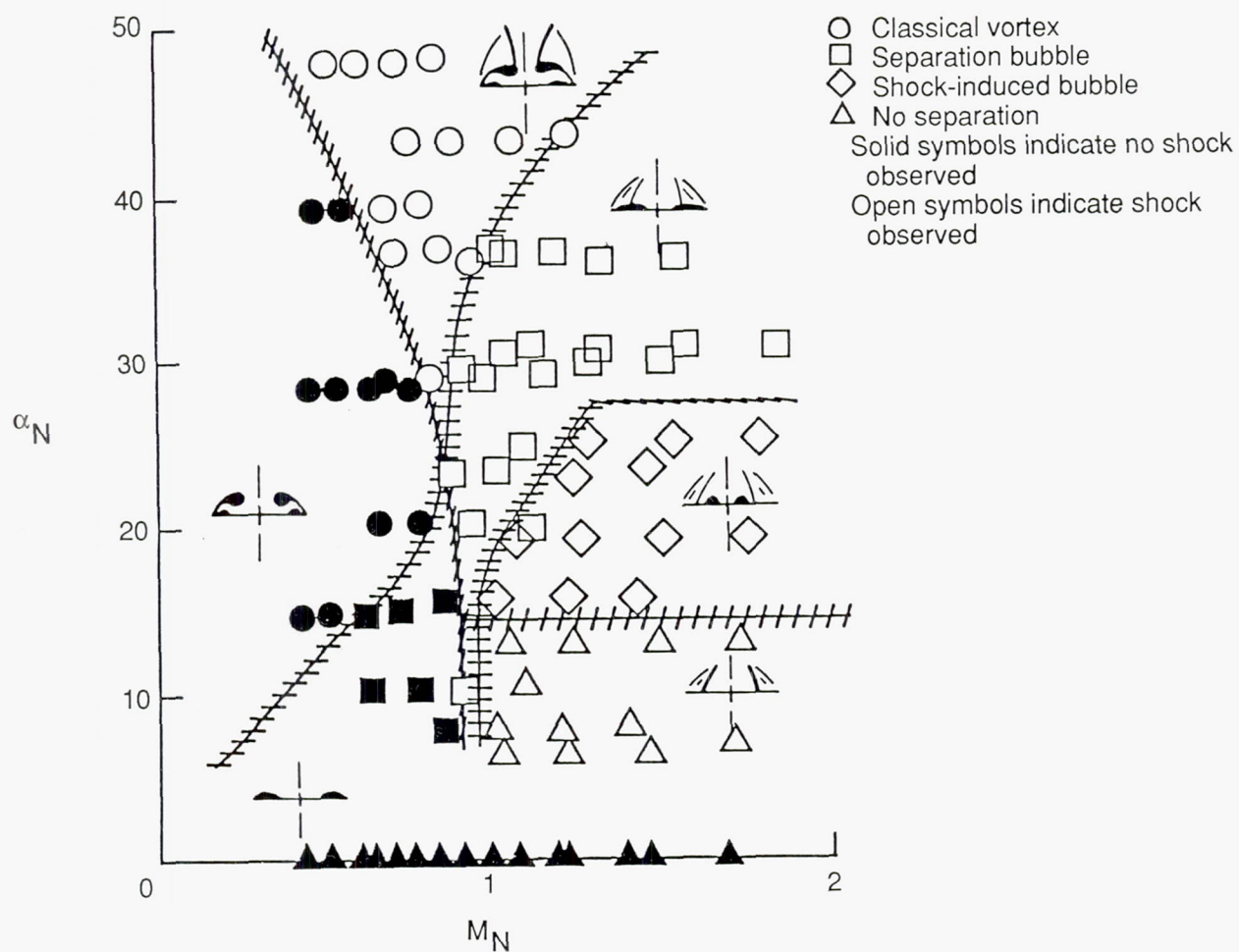
Figure 36. Reclassification of the flow chart of α_N versus M_N.
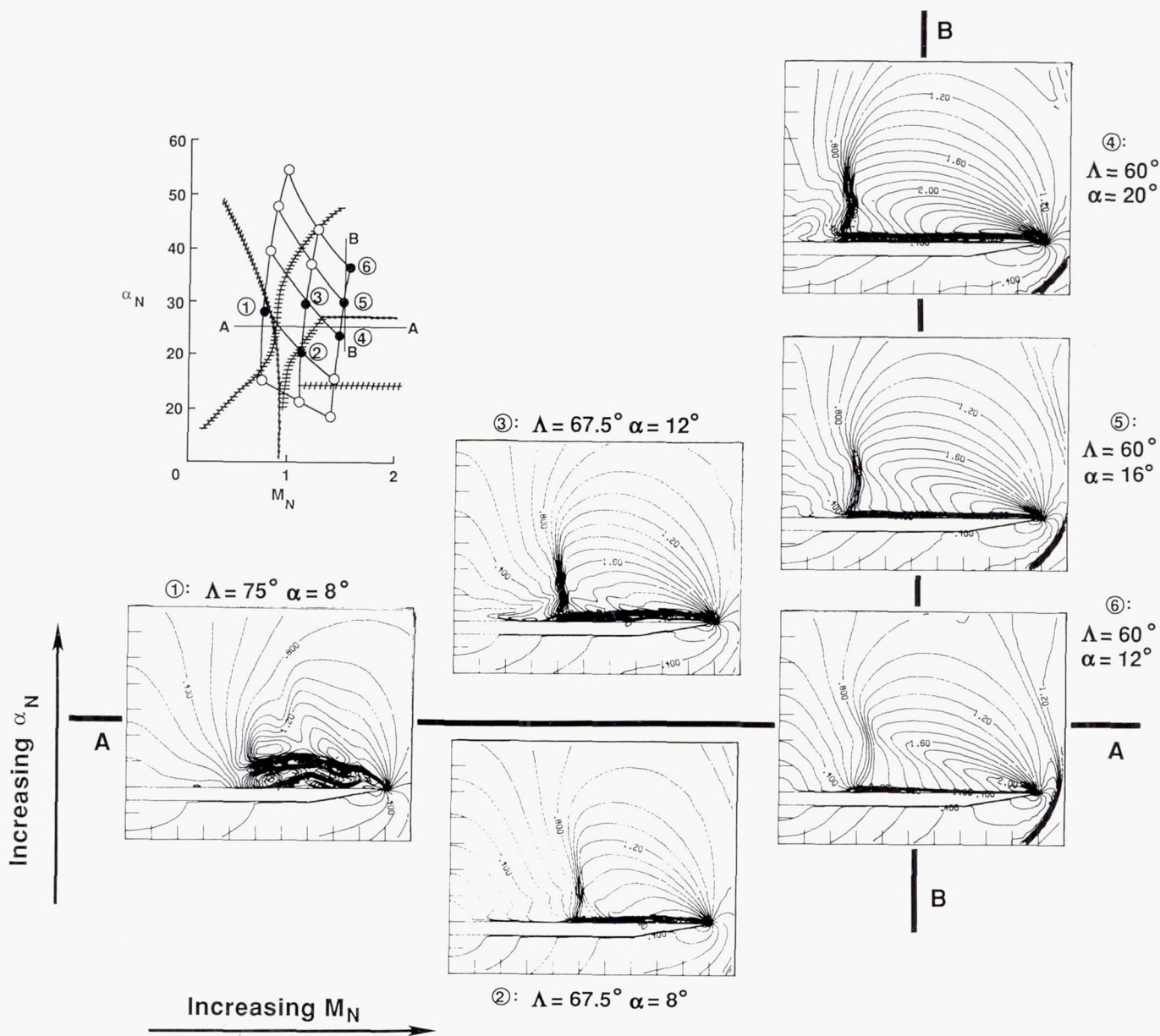
Figure 37. Computational data illustrating the transition between separated and attached flows along lines of constant α_N and constant M_N.

Appendix A

Turbulence Model

The turbulence model used in the Navier-Stokes code is the Baldwin-Lomax model, which is an algebraic eddy viscosity model. Modifications to the model, as proposed by Degani and Schiff (ref. 23) are incorporated to account for the large regions of cross-flow separation. These modifications deal with the parameter $F(s)$, which determines the length scales and thus the eddy viscosity. In the regions of large cross-flow separation, the function $F(s)$ typically exhibits two local maxima along a ray normal to the body. The first maximum is associated with a boundary layer. The second maximum is associated with the primary vortex core and is typically larger than the first maximum. If the second value is selected, then the outer eddy viscosity is much too large and distorts the primary and secondary flow patterns.

In the present investigation, a further problem was identified with the selection of F_{max} that is related to secondary separation. Around the location of a separation point for a secondary vortex, the boundary layer and vortical feeding sheet become merged. Away from the separation point, the boundary layer becomes better defined as the feeding sheet grows and moves away from the surface. However, the profile of the boundary layer is such that the maximum associated with the boundary layer is not defined. Thus F_{max} is determined by the feeding sheet, as illustrated in figure A1. The contour data show the locations of F_{max} in the flow field. The line plot beneath the contour data illustrates the rise of F_{max} in the region of secondary separation. The F_{max} parameter is seen to be significantly greater than the maximum associated with the boundary layer in the nonseparated regions such as near the centerline. The net result is too large a value for the outer eddy viscosity.

To determine the effect of this higher than normal eddy viscosity, a slightly finer grid (151×95) was employed. This grid had more points within the region of primary and secondary separation than did the original grid (151×75). The finer grid solution yielded a very similar solution. The problem of F_{max} being defined by the feeding sheet was reduced although not eliminated. Essentially, because of the greater number of cells defining the boundary layer, the boundary-layer profile emerged closer to the separation point than was the case for the original solution. The net result was a smaller eddy viscosity, which yielded a slightly stronger secondary vortex. However, the primary vortex core or secondary separation locations did not change.

Another approach was to not allow F_{max} to vary more than 20 percent from grid cell to grid cell. In the regions where F_{max} did significantly increase, F_{max} was set equal to the previous cell value. This approach totally eliminated the problem associated with the feeding sheet. Again, the net effect was a smaller outer eddy viscosity, resulting in a slightly stronger secondary vortex. However, there was no influence on the primary vortex core and secondary separation locations.

Another aspect of the turbulence model was associated with those cases where boundary-layer model affected the type of primary flow structure (i.e., attached flow or separated flow). Experimentally the models had a transition strip located 0.2 in. behind and parallel to the leading edge. The purpose of the strip was to ensure fully turbulent flow for attached flow cases. However, the flow could be expected to be laminar up to the transition strip, possibly up to some point inboard of the strip. Therefore, several solutions were obtained where the turbulence model was only activated from the centerline to the point of the transition strip (97 percent of semispan) and two more inboard locations (95 percent and 70 percent of semispan). The case examined was for $\Lambda = 67.5°$, $\alpha = 8°$, and $M = 2.8$. The results showed that limiting the turbulence model as such did not influence the overall flow structure. The flow was still attached at the leading edge with shock-induced separation occurring inboard. One explanation for this observation is that the shock-induced separation produces a change in local flow angularity at the leading edge.
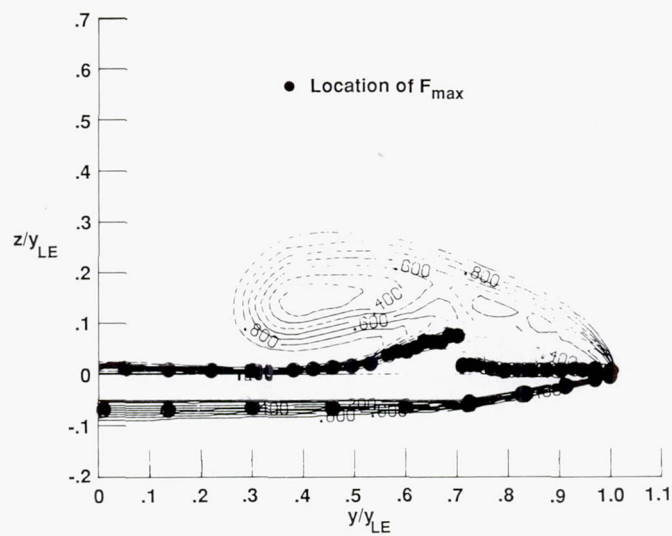
(a) Total pressure ratio contours with location of $F_{\max}$.
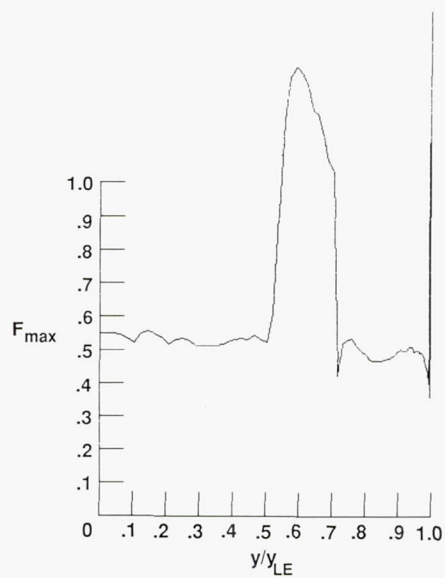
(b) Spanwise distribution of $F_{\max}$.

Figure A1. The location and value of the turbulence model function $F_{\max}$ for $\Lambda = 75°$, $\alpha = 12°$, and $M = 2.8$.

Appendix B

Three-Dimensional and Conical Navier-Stokes Solutions for the 67.5° and 60° Delta Wings

Presented in this appendix are the computational data from the three-dimensional and conical Navier-Stokes solutions for the 67.5° and 60° delta wings at $\alpha = 8°$. Solutions with a laminar- and a turbulent-boundary-layer condition are presented. The computational data are presented here in the form of total Mach number contours, particle trace data and surface pressure data. A discussion of the different formats of computational data presentation is given in the main text.

Computational data from the three-dimensional laminar Navier-Stokes solution for the 67.5° delta wing at $\alpha = 8°$ are presented in figure B1. Main flow structures are labeled in the figure with the notation given on page 2. The computed flow structure is that of a primary vortex separating at the leading edge with the core lying close to the surface of the wing. The particle trace data of figure B1(b) also show the formation of a secondary vortex beneath the thin primary vortex. The nondimensional size (i.e., y/y_{LE} versus z/y_{LE}) of the vortex decreases slightly as the trailing edge is approached. Note that the local Reynolds number increases as the trailing edge is approached with a trailing-edge Reynolds number of 2.41×10^6.

Computational data from conical laminar Navier-Stokes solutions obtained at Reynolds numbers of 0.5×10^6, 1.0×10^6, and 2.4×10^6 for the 67.5° delta wing at $\alpha = 8°$ are presented in figure B2. The conical computed flow structures are essentially the same as those of the corresponding three-dimensional solution. As was observed in the corresponding three-dimensional solution, the conical solutions illustrate a decrease in the nondimensional size of the primary vortex as Reynolds number increases.

Computational data from the three-dimensional turbulent Navier-Stokes solution for the 67.5° delta wing at $\alpha = 8°$ are presented in figure B3. In contrast to the corresponding laminar solution, the flow structure is that of attached flow at the leading edge with a cross-flow shock and shock-induced separation occurring inboard of the leading edge. These flow structures appear to be insensitive to local Reynolds number, which increases as the trailing edge is approached. The particle trace data of figure B3(b) also show the formation just inboard of the leading edge of a separation bubble that is not evident in the contour data. This type of flow structure was observed by Seshadri and Narayan (ref. 34) for shock-induced

separated flows. The flow structure is a localized separation occurring at the leading edge, as the flow inboard appears to be unaffected by the presence of the flow structure.

Computational data from conical turbulent Navier-Stokes solutions obtained at Reynolds numbers of 0.5×10^6, 1.0×10^6, and 2.4×10^6 for the 67.5° delta wing at $\alpha = 8°$ are presented in figure B4. As was observed in the corresponding three-dimensional solution, the conical solutions predict attached flow at the leading edge with shock-induced separation that appears to be insensitive to Reynolds number. The localized leading-edge separation noted in the three-dimensional solution (see fig. B3(b)) is only predicted in the $Re = 2.41 \times 10^6$ conical solution, as seen in figure B4(b).

Computational data from the three-dimensional laminar Navier-Stokes solution for the 60° delta wing at $\alpha = 8°$ are presented in figure B5. The computed flow structure is that of attached flow at the leading edge with a very weak cross-flow shock occurring inboard of the leading edge. The data of figure B5(a) and (b) also indicate smooth separation from the surface of the wing to form a very thin vortex whose core lies close to the surface of the wing. The vortex arises from separation that occurs outboard of the cross-flow shock. The surface pressure data of figure B5(c) show that the inboard edge of the primary vortex moves slightly outboard as the trailing edge is approached. The particle trace data of figure B5(b) also show localized, leading-edge separation.
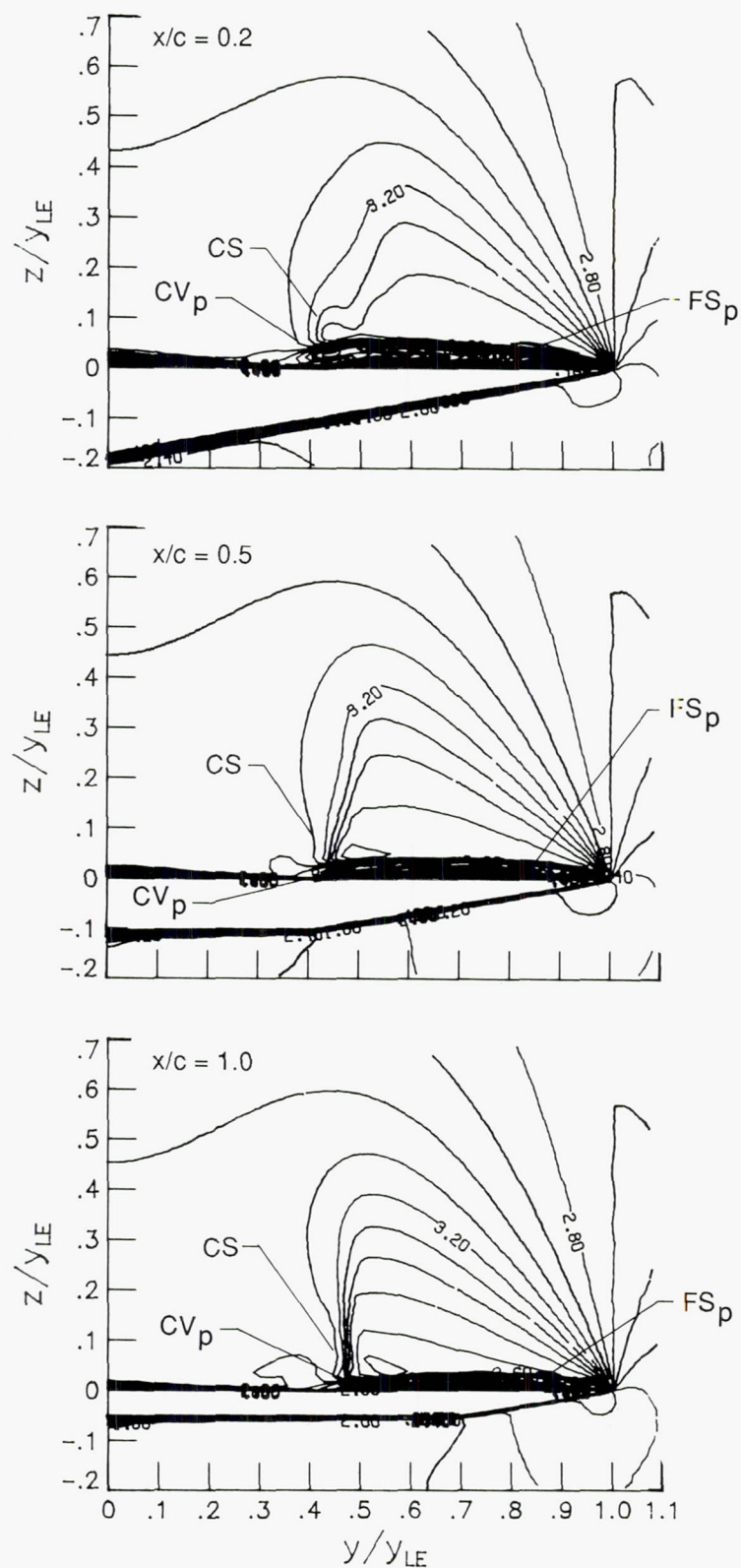
Computational data from conical laminar Navier-Stokes solutions obtained at Reynolds numbers of 0.5×10^6, 1.0×10^6, and 1.73×10^6 for the 60° delta wing at $\alpha = 8°$ are presented in figure B6. As was observed in the corresponding three-dimensional solution, the conical solutions predict attached flow at the leading edge with a smooth separation occurring inboard. The inboard edge of the vortex moves outboard with increasing Reynolds number as was observed in the corresponding three-dimensional solution. However, the particle trace data of figure B6(b) also show the formation of a secondary vortex beneath the smoothly separated vortex for the $Re = 1.73 \times 10^6$ case. This secondary vortex did not appear in the corresponding three-dimensional solution. As noted for the turbulent boundary-layer solutions for the 67.5° wing at $\alpha = 8°$, the localized leading-edge separation noted in the three-dimensional solution (see fig. B5(b)) is only predicted for the higher Reynolds number case (i.e., $Re = 1.73 \times 10^6$) as seen in figure B6(b).

Computational data from the three-dimensional turbulent Navier-Stokes solution for the 60° delta wing at $\alpha = 8°$ are presented in figure B7.

Similar to the corresponding laminar solution, the flow structure is that of attached flow at the leading edge. However, the three-dimensional turbulent Navier-Stokes solution does not predict a smooth separation, as the turbulent boundary-layer flow is more resistant to separation. Instead, the three-dimensional turbulent Navier-Stokes solution predicts shock-induced separation where the separation point occurs directly beneath or just inboard of the point at which the cross-flow shock impinges on the surface of the wing. In contrast, the three-dimensional laminar Navier-Stokes solution predicted a smooth separation where the separa-

tion point occurs outboard of the cross-flow shock. The data of figure B7 show that the shock-induced separation is insensitive to local Reynolds number, which increases as the trailing edge is approached. The trailing-edge Reynolds number for this case is 1.73×10^6.

Computational data from conical laminar Navier-Stokes solutions obtained at Reynolds numbers of 0.5×10^6, 1.0×10^6, and 1.73×10^6 for the 60° delta wing at $\alpha = 8°$ are presented in figure B8. The conical computed flow structures and trends with Reynolds number are essentially the same as those of the corresponding three-dimensional solutions.

(a) Total Mach number.

Figure B1. Computational data from the three-dimensional laminar Navier-Stokes solution for $\Lambda = 67.5°$, $\alpha = 8°$, and $M = 2.8$.
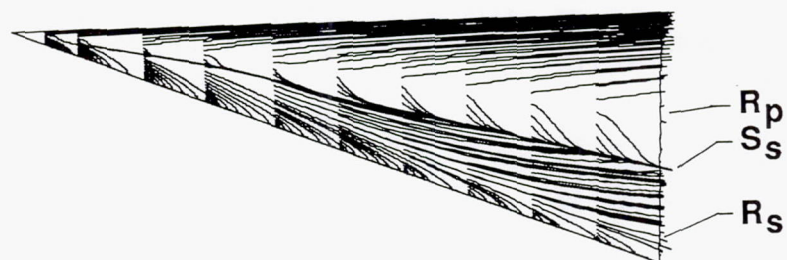
(b) Particle trace data.
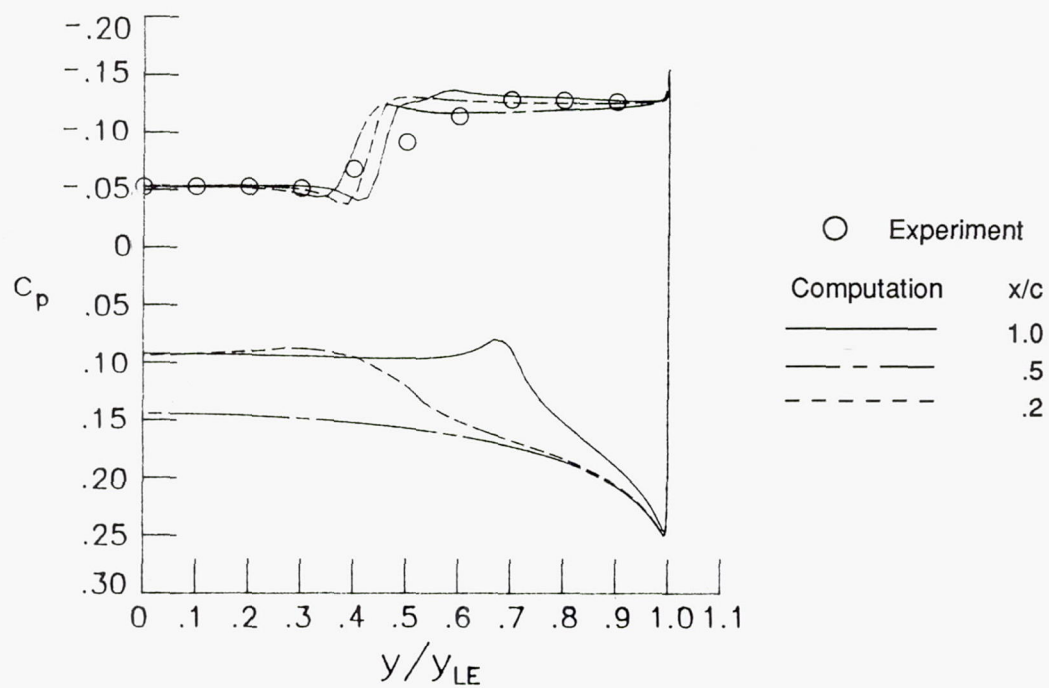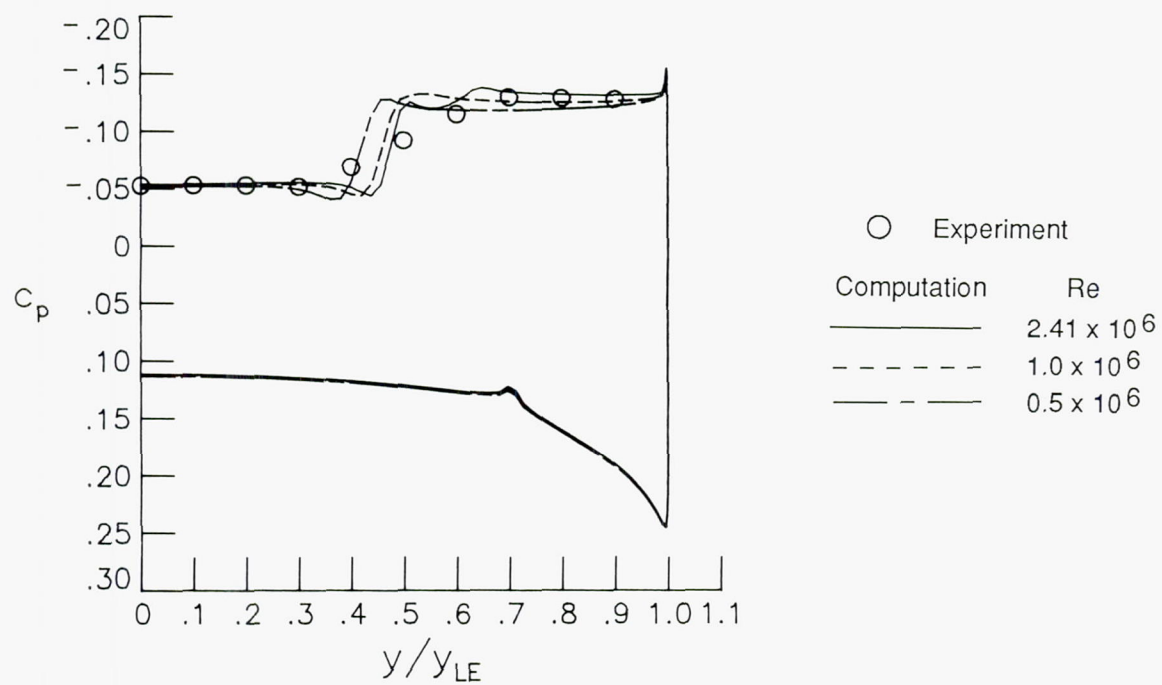

(c) Surface pressure distributions.

Figure B1. Concluded.
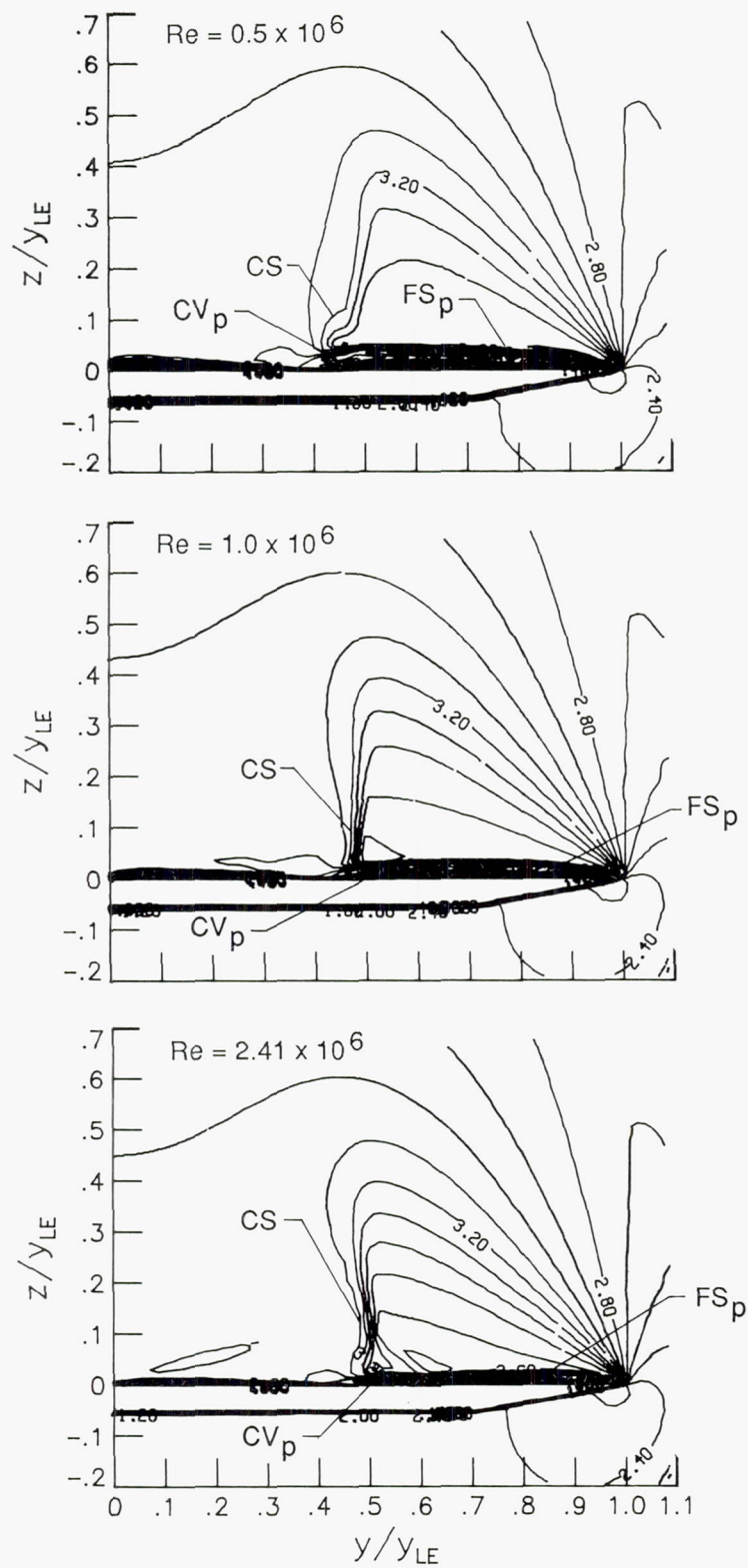
(a) Total Mach number.

Figure B2. Computational data from conical laminar Navier-Stokes solutions at various Reynolds numbers for $\Lambda = 67.5°$, $\alpha = 8°$, and $M = 2.8$.
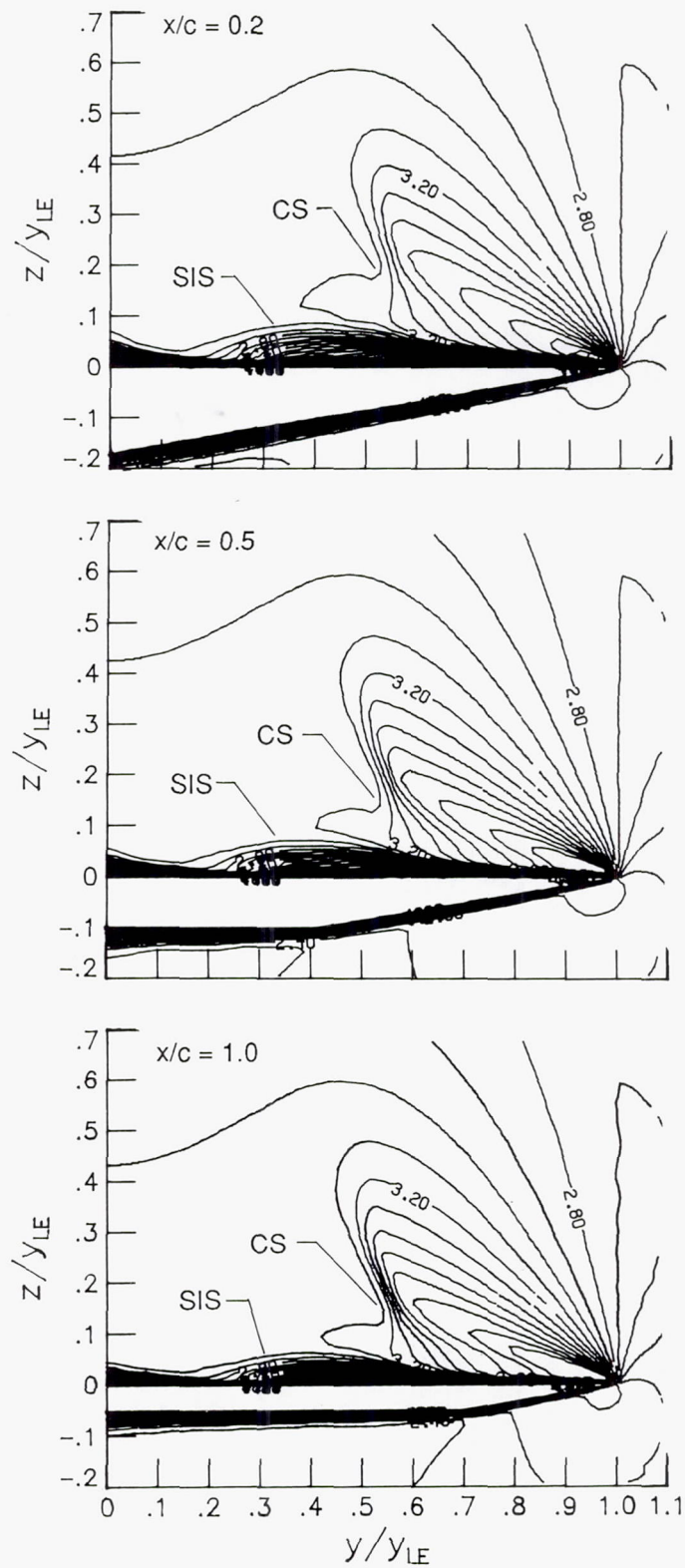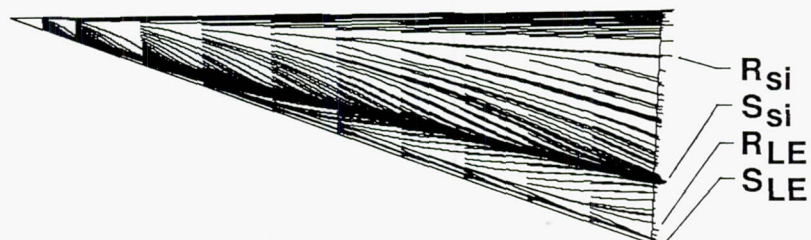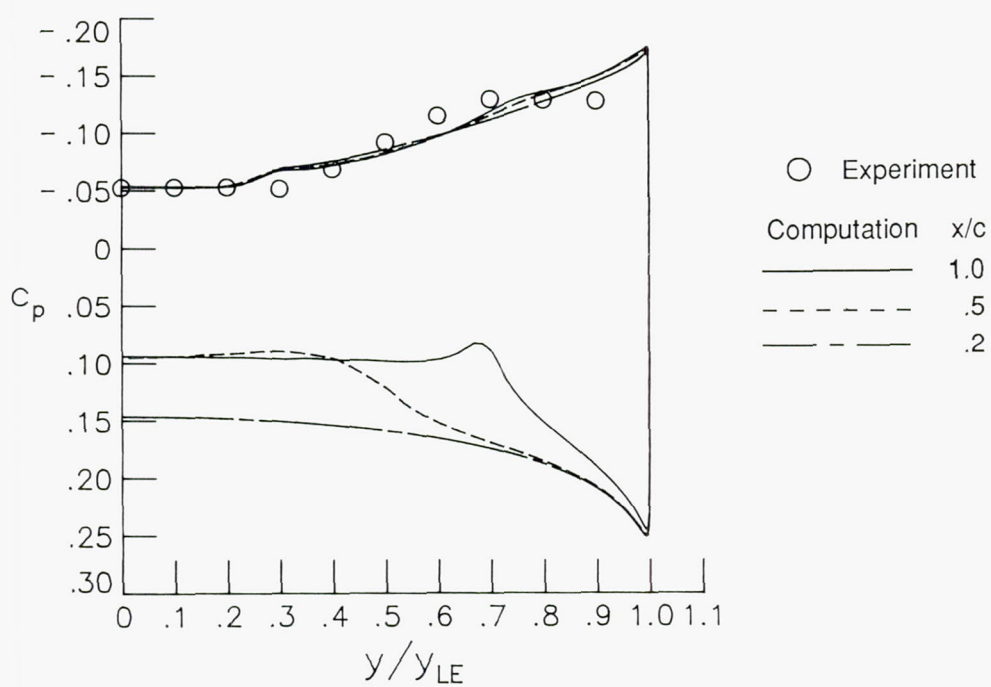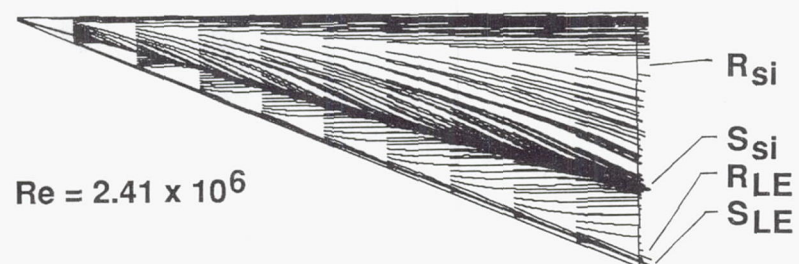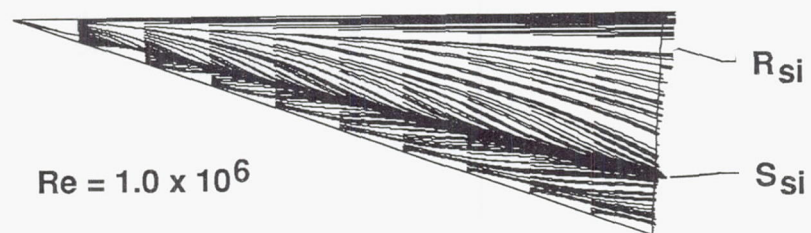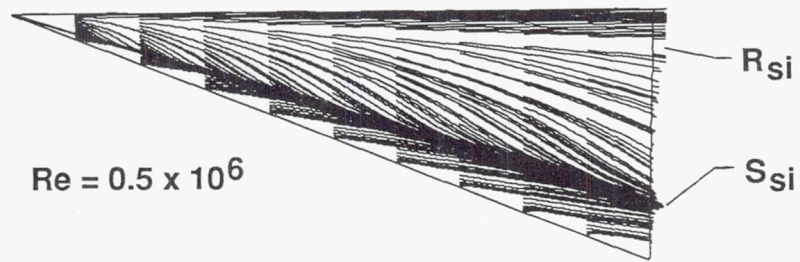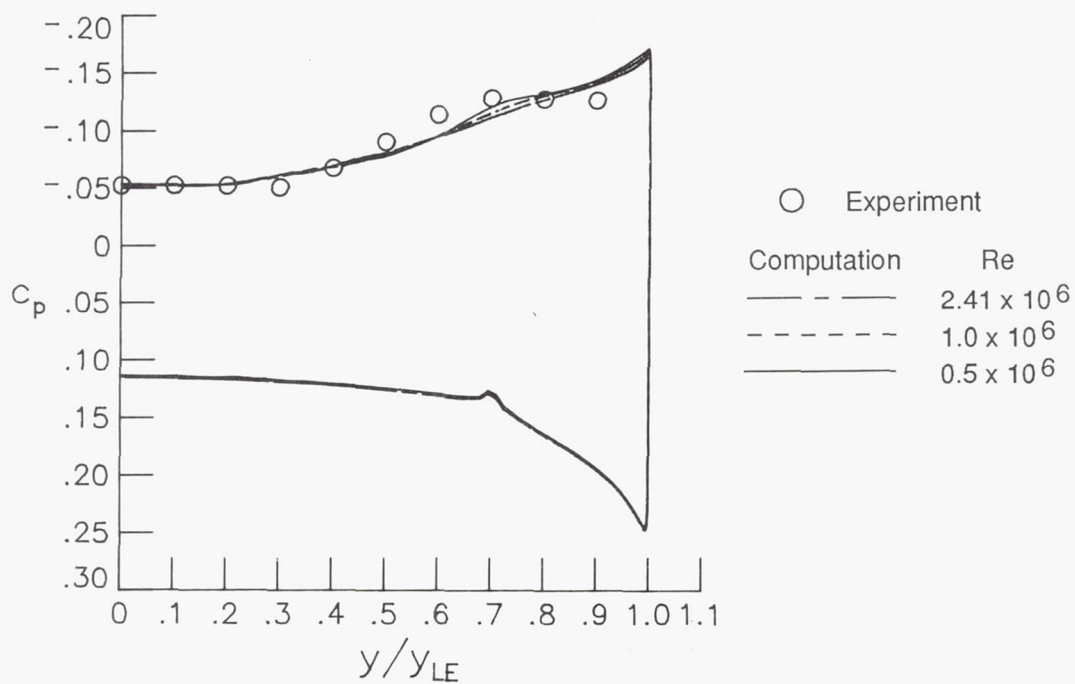
$\text{Re} = 0.5 \times 10^6$

R_p
S_s
R_s

$\text{Re} = 1.0 \times 10^6$

R_p
S_s
R_s

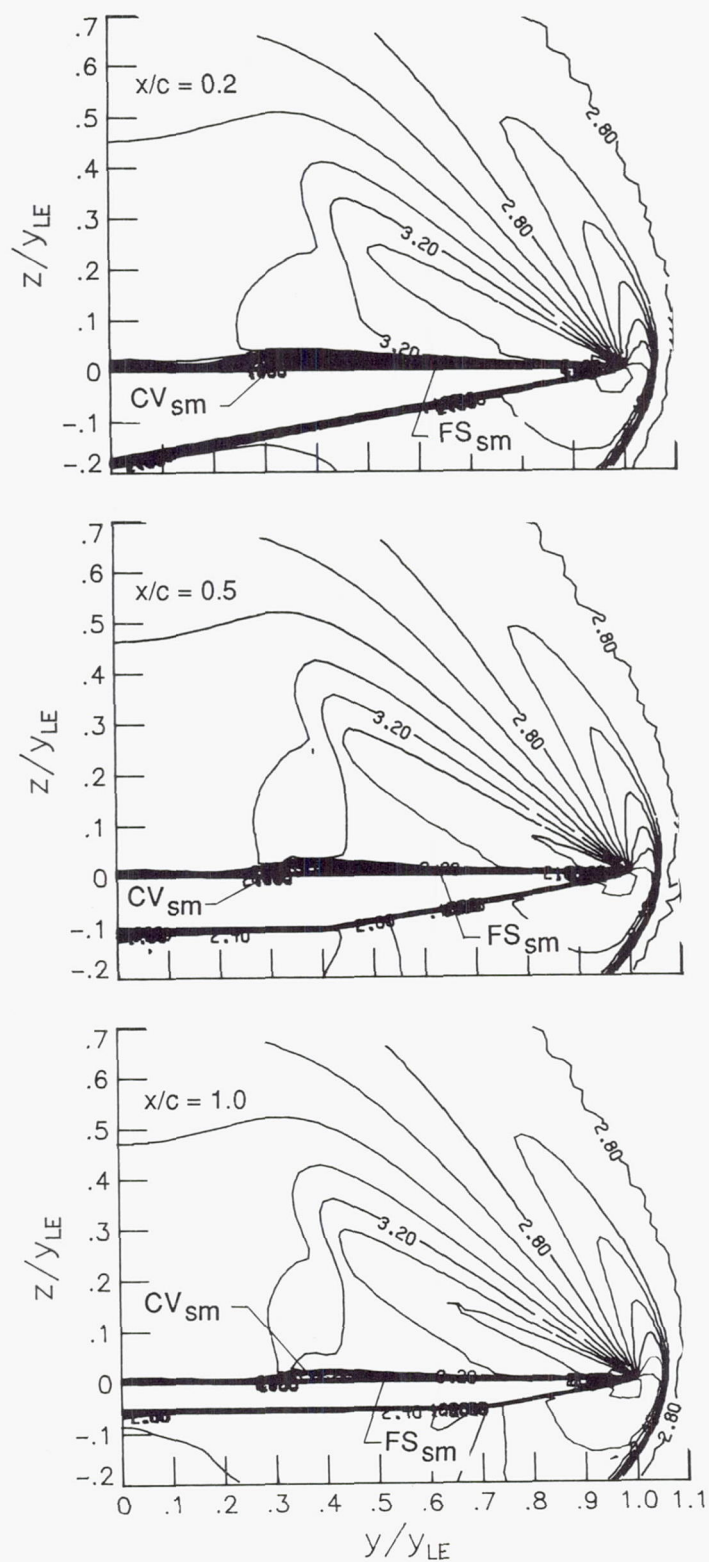$\text{Re} = 2.41 \times 10^6$

R_p
S_s
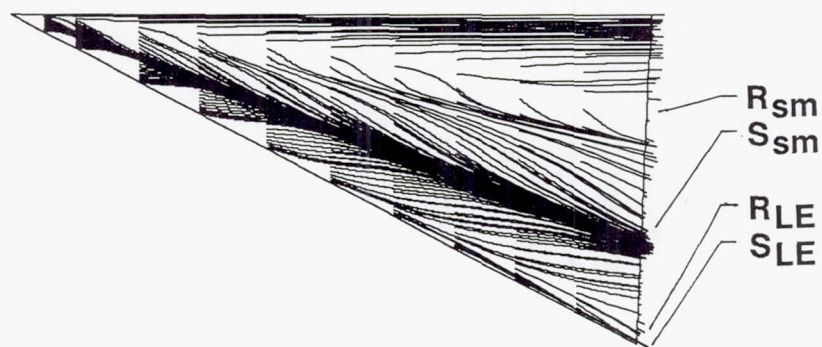R_s
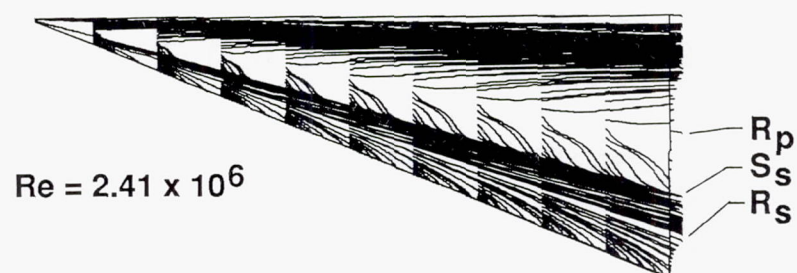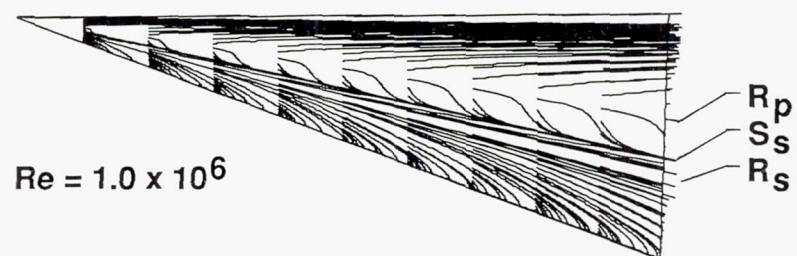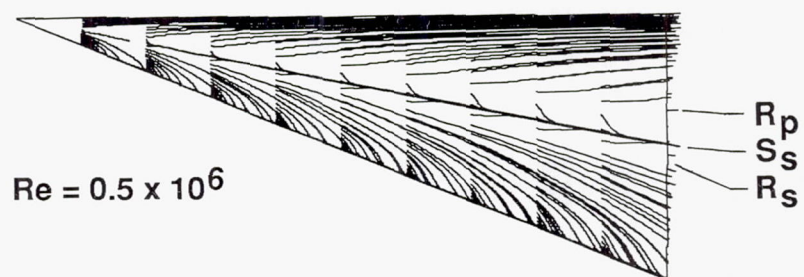
(b) Particle trace data.

Figure B2. Continued.

81

(c) Surface pressure distributions.

Figure B2. Concluded.

(a) Total Mach number contours.

Figure B3. Computational data for the three-dimensional turbulent Navier-Stokes solution for $\Lambda = 67.5°$, $\alpha = 8°$, and $M = 2.8$.

R_{si}
S_{si}
R_{LE}
S_{LE}

(b) Particle trace data.

○ Experiment

Computation	x/c
——————	1.0
− − − − −	.5
— · — · —	.2

(c) Surface pressure distributions.

Figure B3. Concluded.
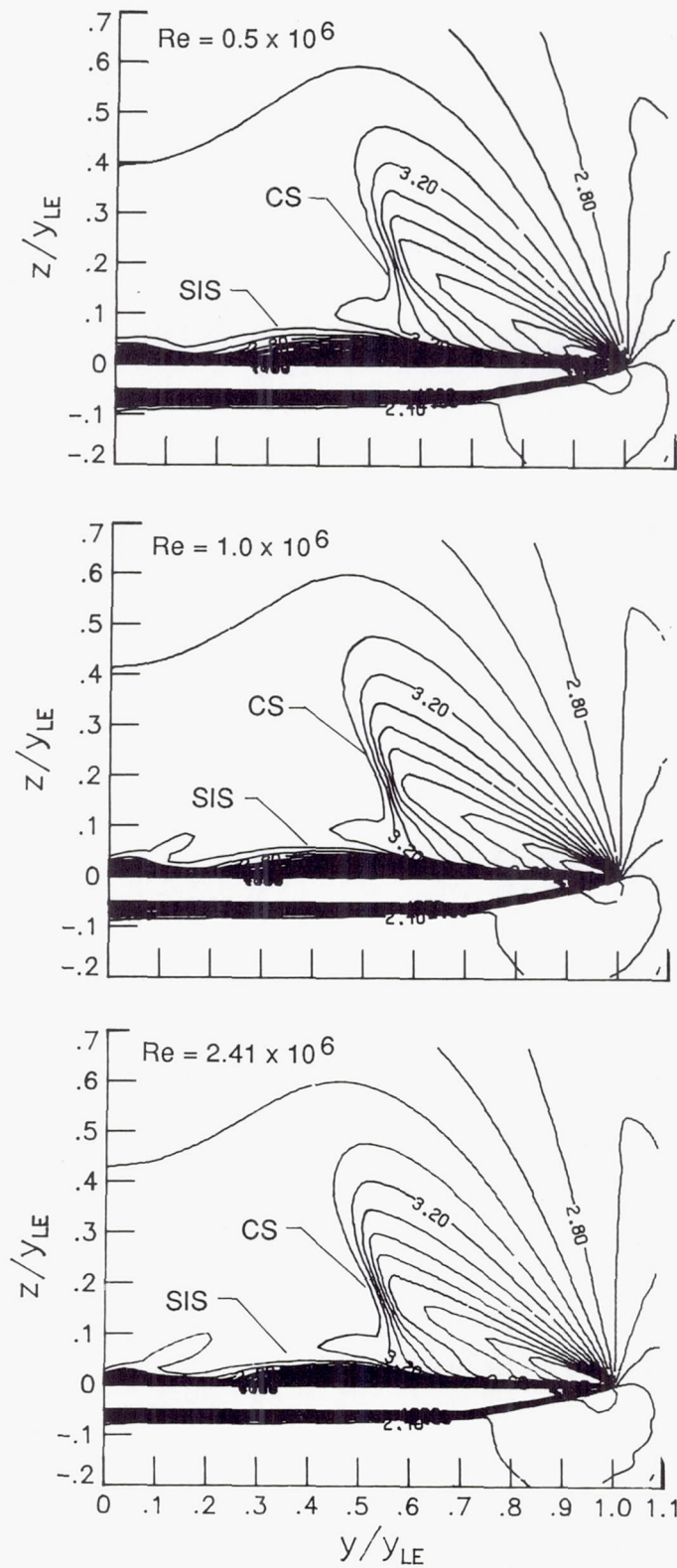
(a) Total Mach number contours.

Figure B4. Computational data from conical turbulent Navier-Stokes solutions for $\Lambda = 67.5°$, $\alpha = 8°$, and $M = 2.8$.

Re = 0.5 x 10^6 R$_{si}$ S$_{si}$

Re = 1.0 x 10^6 R$_{si}$ S$_{si}$

Re = 2.41 x 10^6 R$_{si}$ S$_{si}$ R$_{LE}$ S$_{LE}$

(b) Particle trace data.

Figure B4. Continued.
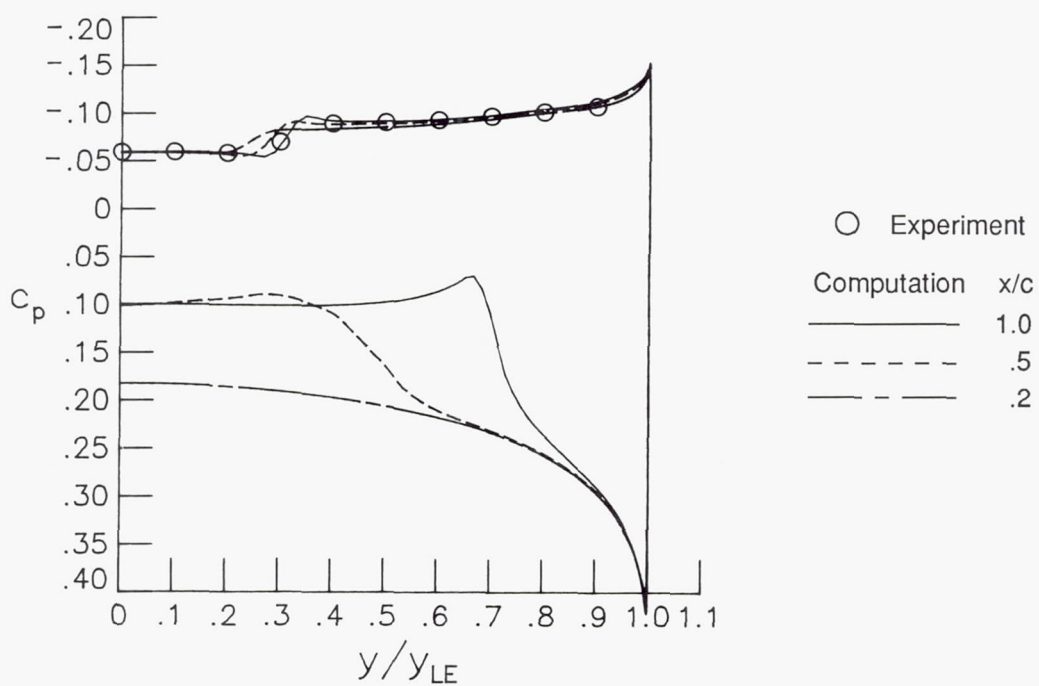
(c) Surface pressure distributions.

Figure B4. Concluded.

(a) Total Mach number contours.

Figure B5. Computational data for the three-dimensional laminar Navier-Stokes solution for $\Lambda = 60°$, $\alpha = 8°$, and $M = 2.8$.
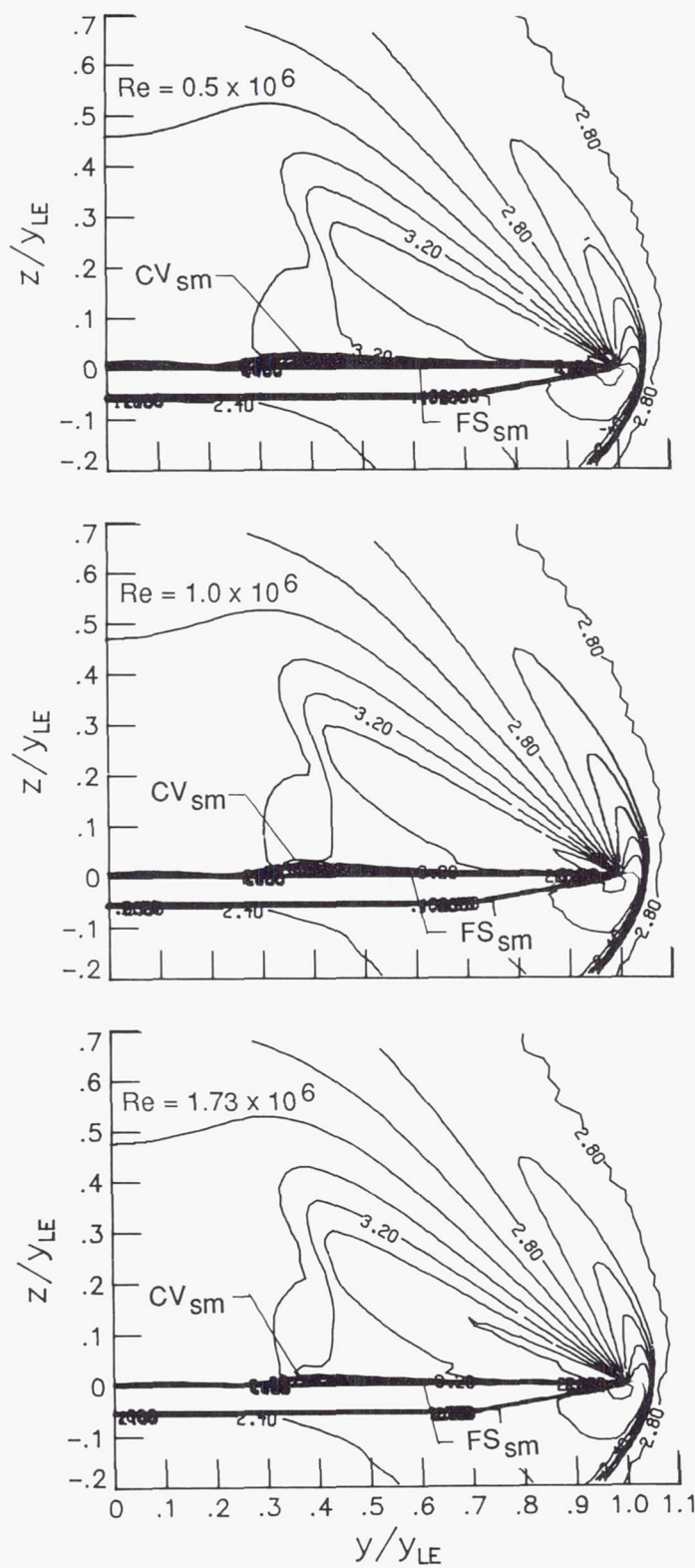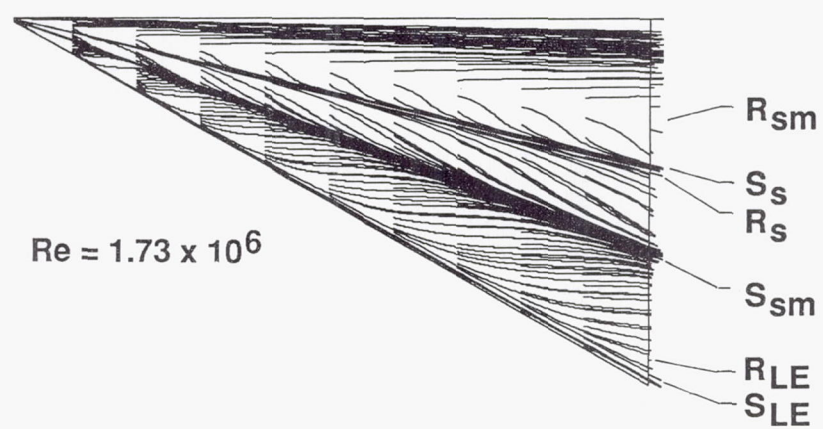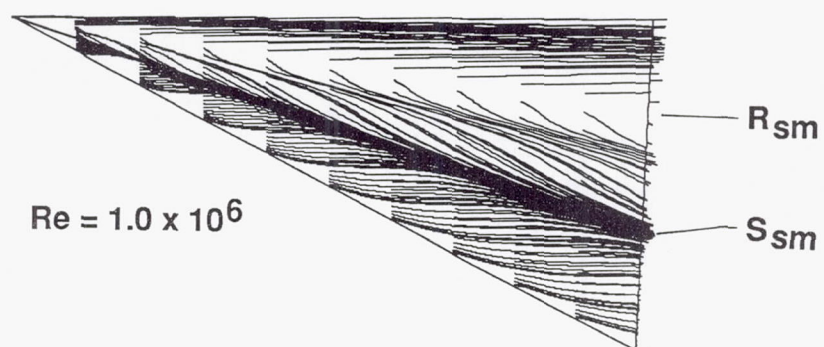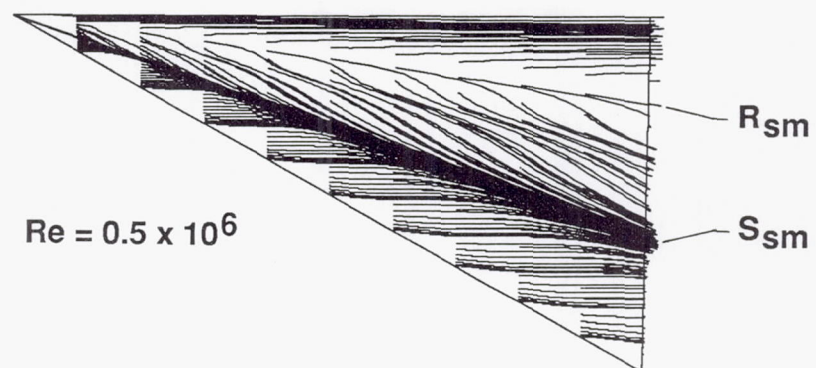
(b) Particle trace data.

(c) Surface pressure distribution.

Figure B5. Concluded.
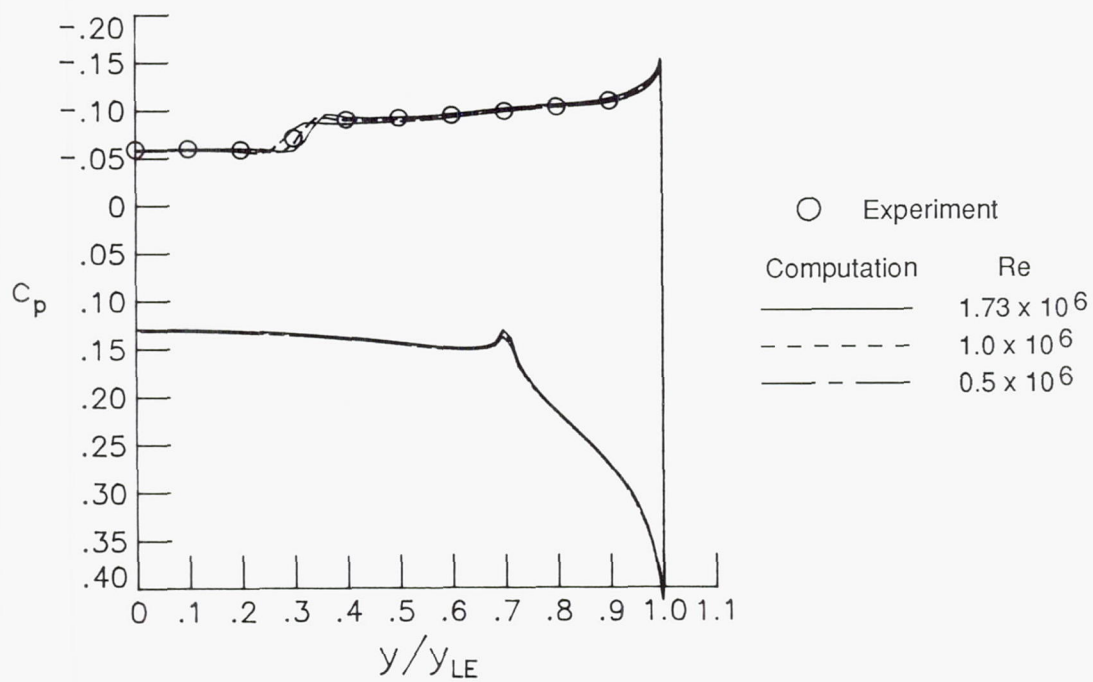
(a) Total Mach number contours.

Figure B6. Computational data from conical laminar Navier-Stokes solutions for $\Lambda = 60°$, $\alpha = 8°$, and $M = 2.8$.

$Re = 0.5 \times 10^6$

R_{sm}

S_{sm}

$Re = 1.0 \times 10^6$

R_{sm}

S_{sm}

$Re = 1.73 \times 10^6$

R_{sm}

S_s
R_s

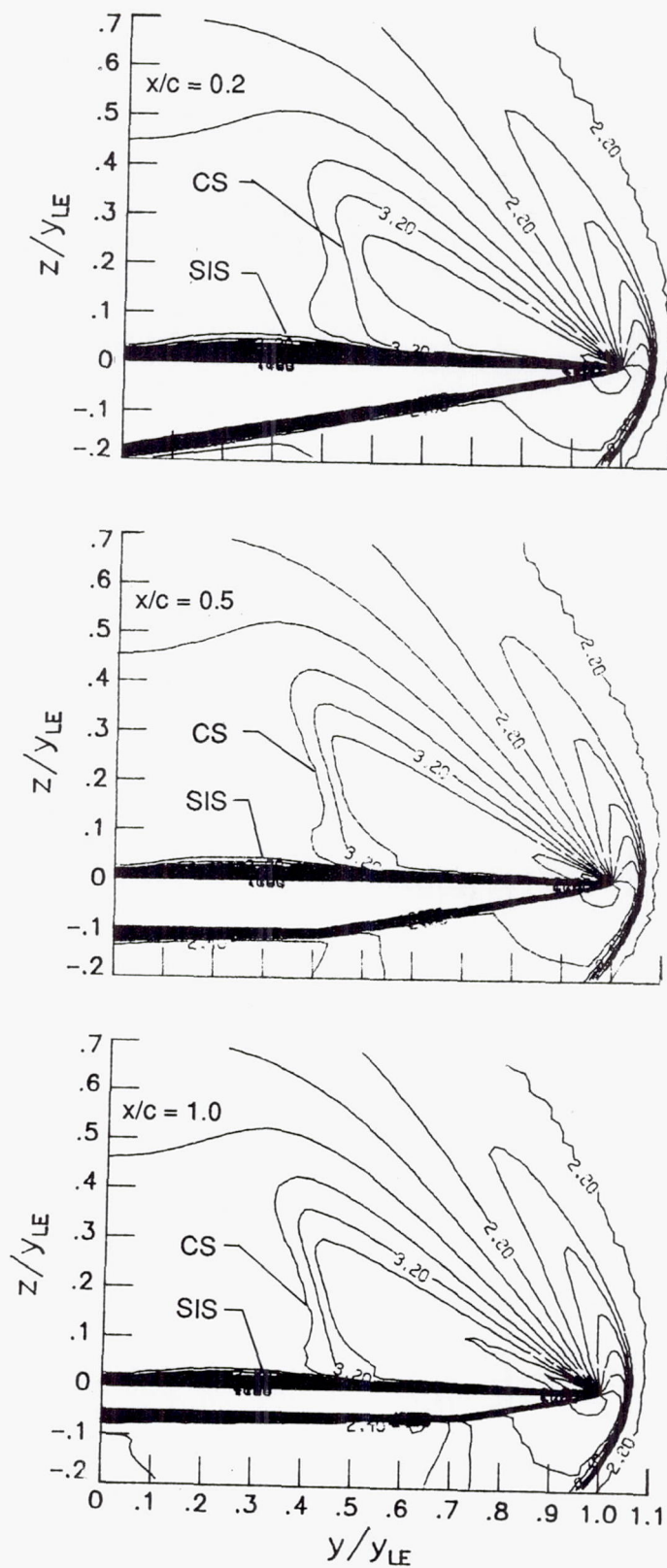S_{sm}

R_{LE}
S_{LE}

(b) Particle trace data.

Figure B6. Continued.

(c) Surface pressure distribution.

Figure B6. Concluded.

(a) Total Mach number contours.

Figure B7. Computational data for the three-dimensional turbulent Navier-Stokes solution for $\Lambda = 60°$, $\alpha = 8°$, and $M = 2.8$.

(b) Particle trace data.
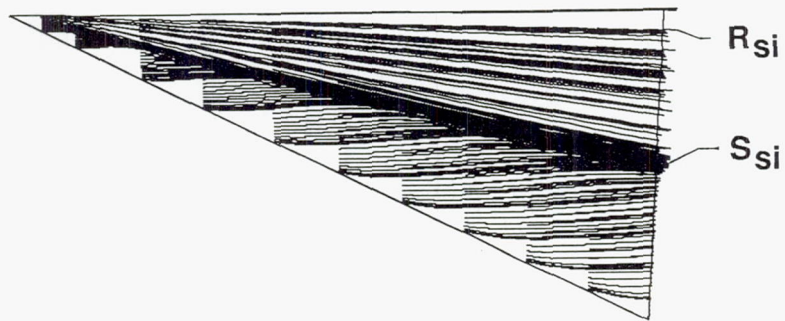

(c) Surface pressure distributions.

Figure B7. Concluded.
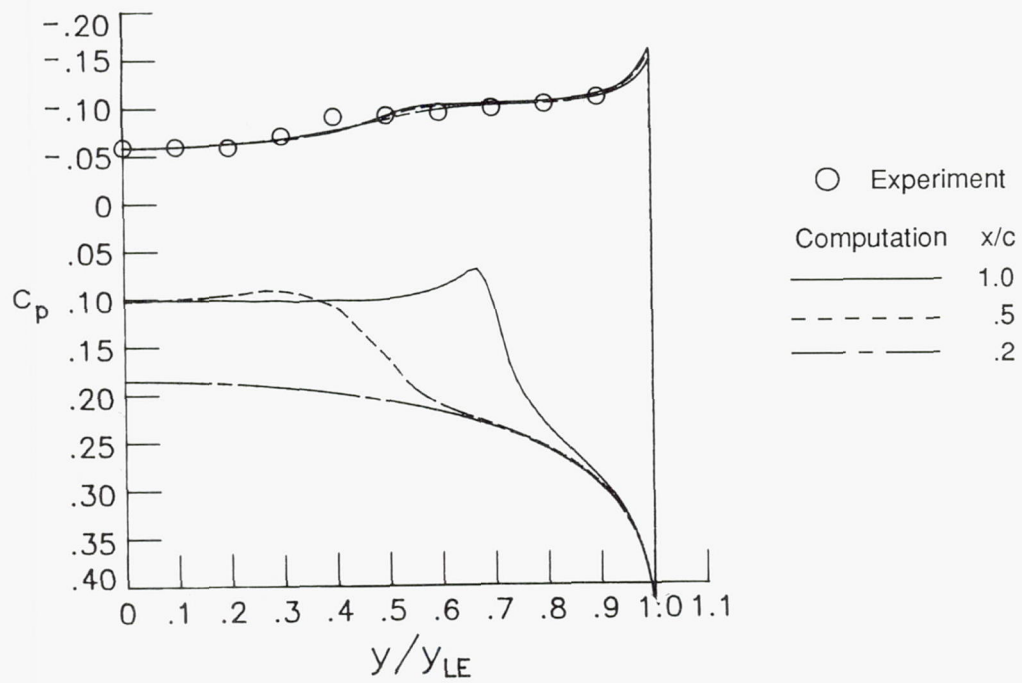
(a) Total Mach number contours.

Figure B8. Computational data from conical turbulent Navier-Stokes solutions for $\Lambda = 60°$, $\alpha = 8°$, and $M = 2.8$.

$Re = 0.5 \times 10^6$
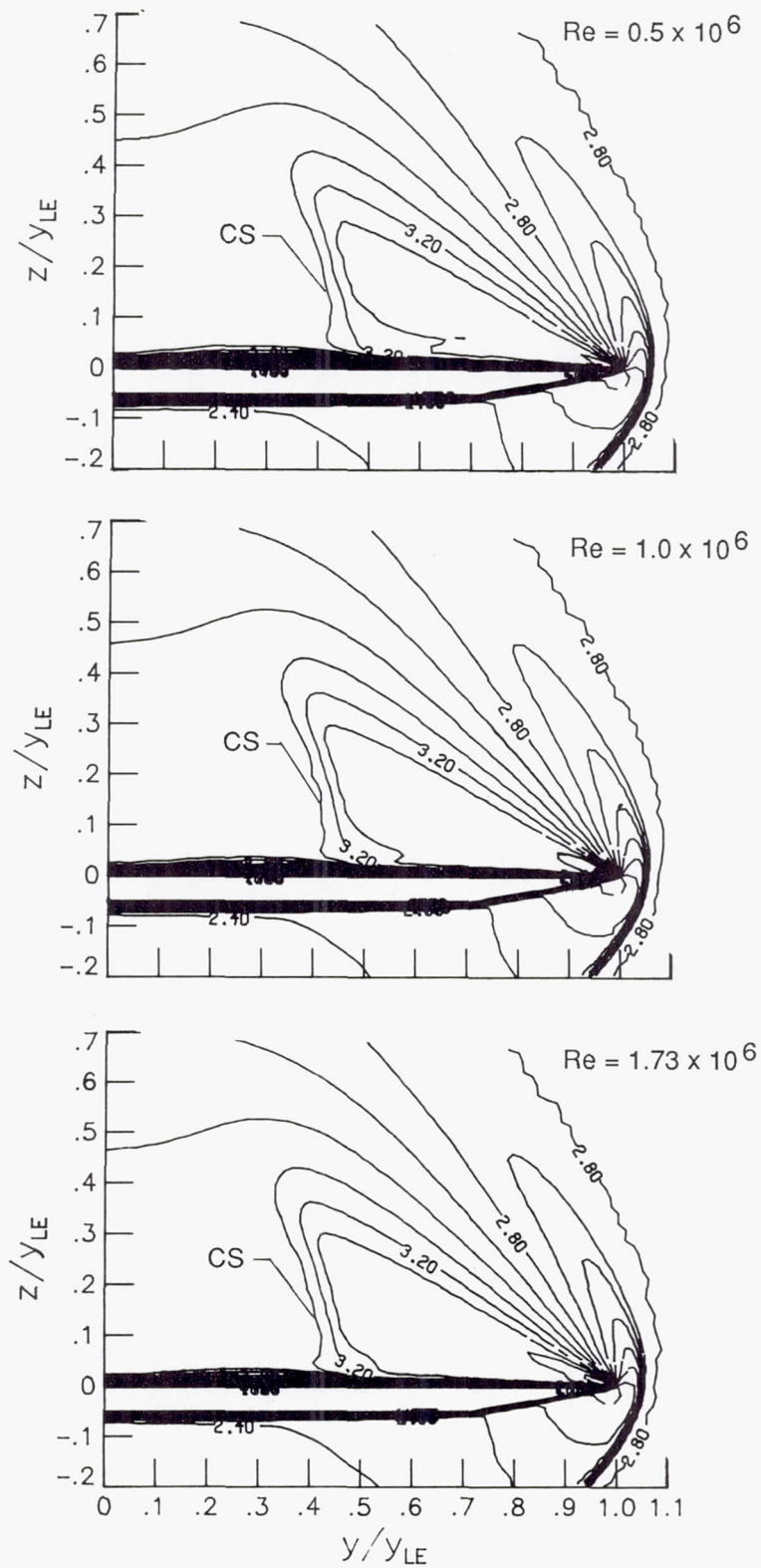
R_{si}

S_{si}

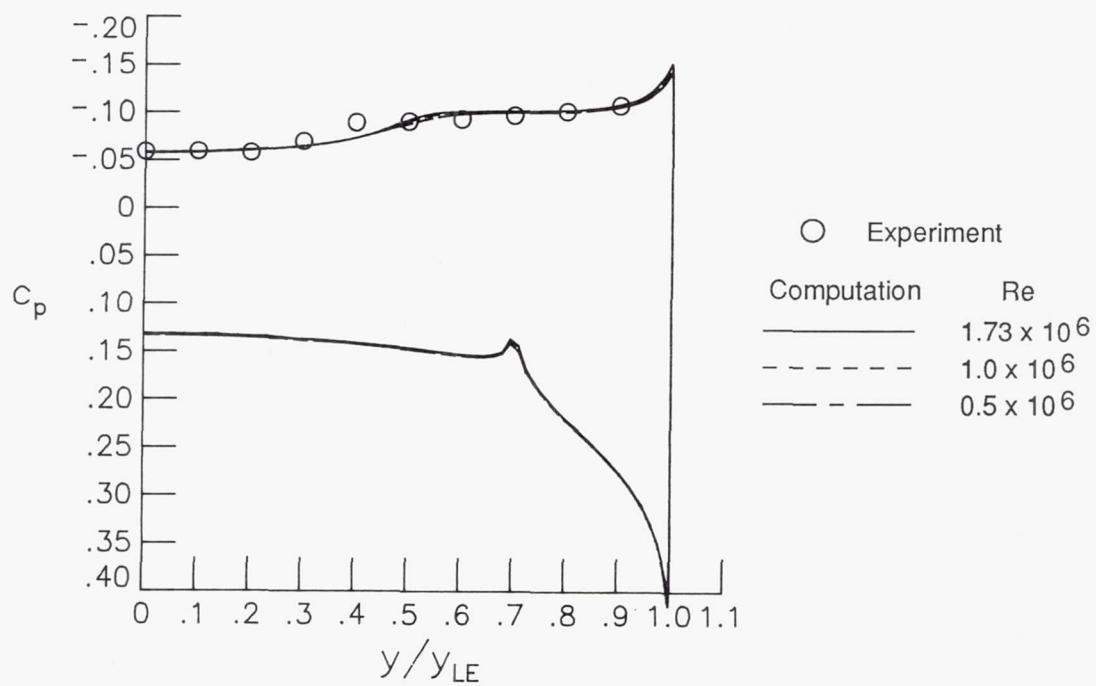$Re = 1.0 \times 10^6$

R_{si}

S_{si}

$Re = 1.73 \times 10^6$

R_{si}

S_{si}
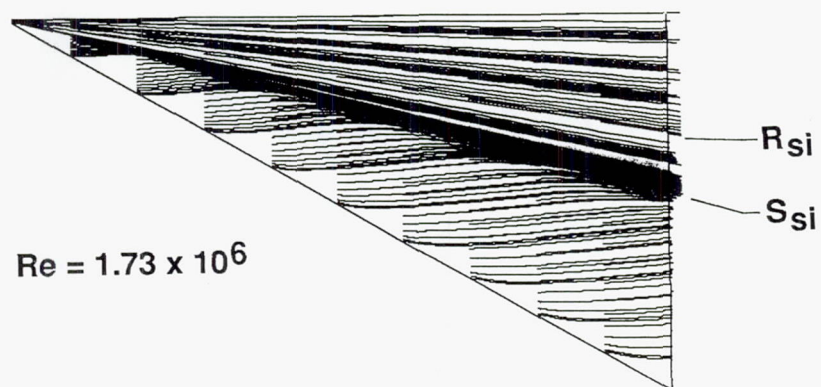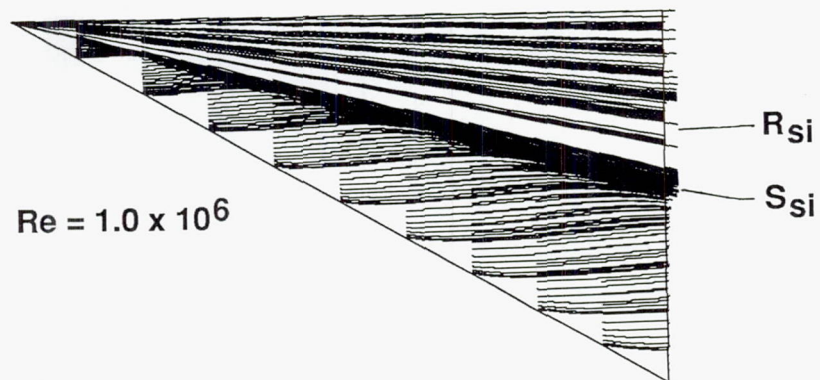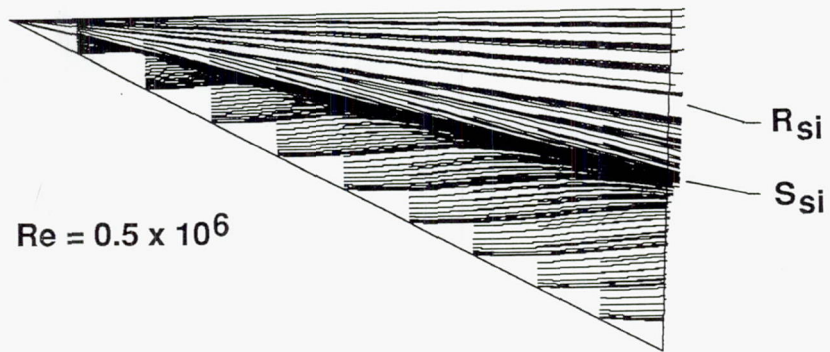
(b) Particle trace data.

Figure B8. Continued.

(c) Surface pressure distributions.

Figure B8. Concluded.

References

1. Brown, Clinton E.; McLean, F. E.; and Klunker, E. B.: Theoretical and Experimental Studies of Cambered and Twisted Wings Optimized for Flight at Supersonic Speeds. *Advances in Aeronautical Sciences*, Volume 3, Macmillan Co., 1962, pp. 415–430.

2. Pittman, James L.; Miller, David S.; and Mason, William H.: *Supersonic, Nonlinear, Attached-Flow Wing Design for High Lift With Experimental Validation.* NASA TP-2336, 1984.

3. Lan, C. Edward; and Chang, Jen-Fu: *VORCAM—A Computer Program for Calculating Vortex Lift Effect of Cambered Wings by the Suction Analogy.* NASA CR-165800, 1981.

4. Thomas, James L.; and Newsome, Richard W.: Navier-Stokes Computations of Lee-Side Flows Over Delta Wings. AIAA-86-1049, May 1986.

5. Murman, Earll M.; Powell, Kenneth G.; Miller, David S.; and Wood, Richard M.: Comparison of Computations and Experimental Data for Leading Edge Vortices—Effects of Yaw and Vortex Flaps. AIAA-86-0439, Jan. 1986.

6. Arlinger, Bert G.: Computation of Supersonic Flow Including Leading-Edge Vortex Flows Using Marching Euler Technique. *Numerical Methods in Fluid Mechanics II*, Koichi Oshima, ed., Japan Soc. of Computational Fluid Dynamics, 1986, pp. 1–11.

7. Murman, Earll M.; Rizzi, Arthur; and Powell, Kenneth G.: High Resolution Solutions of the Euler Equations for Vortex Flows. *Progress and Supercomputing in Computational Fluid Dynamics*, Earll M. Murman and Saul S. Abarbanel, eds., Birkhäuser Boston, Inc., 1985, pp. 93–113.

8. Rizzi, Arthur; and Eriksson, Lars-Erik: Computation of Inviscid Incompressible Flow With Rotation. *J. Fluid Mech.*, vol. 153, Apr. 1985, pp. 275–312.

9. Buter, Thomas A.; and Rizzetta, Donald P.: Steady Supersonic Navier-Stokes Solutions of a 75° Delta Wing. *Vortex Flow Aerodynamics, Volume I*, James F. Campbell, Russell F. Osborn, and Jerome T. Foughner, Jr., eds., NASA CP-2416, 1986, pp. 331–339.

10. Fujii, Kozo; and Kutler, Paul: Numerical Simulation of the Viscous Flow Fields Over Three-Dimensional Complicated Geometries. AIAA-84-1550, June 1984.

11. Rizzetta, Donald P.; and Shang, Joseph S.: Numerical Simulation of Leading-Edge Vortex Flows. AIAA-84-1544, June 1984.

12. Stanbrook, A.; and Squire, L. C.: Possible Types of Flow at Swept Leading Edges. *Aeronaut. Q.*, vol. XV, pt. 1, Feb. 1964, pp. 72–82.

13. Whitehead, Allen H., Jr.; Hefner, Jerry N.; and Rao, D. M.: Lee-Surface Vortex Effects Over Configurations in Hypersonic Flow. AIAA Paper No. 72–77, Jan. 1972.

14. Szodruch, Joachim; and Ganzer, Uwe: On the Lee-Side Flow Over Delta Wings at High Angle of Attack. *High Angle of Attack Aerodynamics*, AGARD-CP-247, Jan. 1979, pp. 21-1–21-7.

15. Miller, David S.; and Wood, Richard M.: *Lee-Side Flow Over Delta Wings at Supersonic Speeds.* NASA TP-2430, 1985.

16. Braslow, Albert L.; and Knox, Eugene C.: *Simplified Method for Determination of Critical Height of Distributed Roughness Particles for Boundary-Layer Transition at Mach Numbers From 0 to 5.* NACA TN 4363, 1958.

17. Vatsa, Veer N.; Thomas, James L.; and Wedan, Bruce W.: Navier-Stokes Computations of Prolate Spheroid at Angle of Attack. *J. Aircr.*, vol. 26, no. 11, Nov. 1989, pp. 986–993.

18. Roe, P. L.: Characteristic-Based Schemes for the Euler Equations. *Annual Review of Fluid Mechanics, Volume 18*, Milton van Dyke, J. V. Wehausen, and John L. Lumley, eds., Annual Reviews Inc., 1986, pp. 337–365.

19. Anderson, W. Kyle; Thomas, James L.; and Van Leer, Bram: Comparison of Finite Volume Flux Vector Splittings for the Euler Equations. *AIAA J.*, vol. 24, no. 9, Sept. 1986, pp. 1453–1460.

20. Van Leer, Bram; Thomas, James L.; Roe, Philip L.; and Newsome, Richard W.: A Comparison of Numerical Flux Formulas for the Euler and Navier-Stokes Equations. *A Collection of Technical Papers—AIAA 8th Computational Fluid Dynamics Conference, 1987*, pp. 36–41. (Available as AIAA-87-1104.)

21. Thomas, J. L.; Taylor, S. L.; and Anderson, W. K.: Navier-Stokes Computations of Vortical Flows Over Low Aspect Ratio Wings. AIAA-87-0207, Jan. 1987.

22. Baldwin, Barrett; and Lomax, Harvard: Thin-Layer Approximation and Algebraic Model for Separated Turbulent Flows. AIAA Paper 78-257, Jan. 1978.

23. Degani, David; and Schiff, Lewis B.: Computation of Supersonic Viscous Flows Around Pointed Bodies at Large Incidence. AIAA-83-0034, Jan. 1983.

24. Newsome, Richard W.; and Adams, Mary S.: Numerical Simulation of Vortical Flow Over an Elliptical-Body Missile at High Angles of Attack. AIAA-86-0559, Jan. 1986.

25. Powell, Kenneth G.; Murman, Earll, M.; Perez, Eric S.; and Baron, Judson R.: Total Pressure Loss in Vortical Solutions of the Conical Euler Equations. *AIAA J.*, vol. 25, no. 3, Mar. 1987, pp. 360–368.

26. Powell, Kenneth G.; and Murman, Earll M.: A Comparison of Experimental and Numerical Results for Delta Wings With Vortex Flaps. *A Collection of Technical Papers—AIAA 4th Applied Aerodynamics Conference, June 1986*, pp. 411–424. (Available as AIAA-86-1840.)

27. Powell, Kenneth Grant: *Vortical Solutions of the Conical Euler Equations.* D. Sc. Thesis, Massachusetts Inst. of Technology, July 1987.

28. Wood, Richard M.; and Watson, Carolyn B.: *Study of Lee-Side Flows Over Conically Cambered Delta Wings at Supersonic Speeds.* NASA TP-2660, 1987.

29. Sorenson, Reese L.: *A Computer Program To Generate Two-Dimensional Grids About Airfoils and Other Shapes by the Use of Poisson's Equation.* NASA TM-81198, 1980.

30. Steger, J. L.; and Sorenson, R. L.: Automatic Mesh-Point Clustering Near a Boundary in Grid Generation With Elliptic Partial Differential Equations. *J. Comput. Phys.*, vol. 33, no. 3, Dec. 1979, pp. 405–410.

31. Blottner, F. G.: Variable Grid Scheme Applied to Turbulent Boundary Layers. *Comput. Methods Appl. Mech. & Eng.*, vol. 4, no. 2, Sept. 1974, pp. 179–194.

32. Szodruch, Joachim: *Lee Side Flow for Slender Delta Wings of Finite Thickness.* NASA TM-75753, 1980.

33. Peake, David J.; and Tobak, Murray: *Three-Dimensional Interactions and Vortical Flows With Emphasis on High Speeds.* NASA TM-81169, 1980.

34. Seshadri, S. N.; and Narayan, K. Y.: *Lee-Surface Flow Over Delta Wings at Supersonic Speeds.* TM AE 8610, National Aeronautical Lab. (Bangalore, India), Sept. 1986.

35. Pate, S. R.: *Experimental and Analytical Investigation of Boundary-Layer Transition on Swept Wings at Mach Numbers 2.5 to 5.* AEDC-TR-67-186, U.S. Air Force, Oct. 1967. (Available from DTIC as AD 821 305.)

36. Stallings, Robert L., Jr.; and Lamb, Milton: *Effects of Roughness Size on the Position of Boundary-Layer Transition and on the Aerodynamic Characteristics of a 55° Swept Delta Wing at Supersonic Speeds.* NASA TP-1027, 1977.

37. Squire, L. C.: Flow Regimes Over Delta Wings at Supersonic and Hypersonic Speeds. *Aeronaut. Q.*, vol. 27, pt. 1, Feb. 1976, pp. 1–14.

NASA

National Aeronautics and
Space Administration

Report Documentation Page

1. Report No. NASA TP-3035	2. Government Accession No.	3. Recipient's Catalog No.
4. Title and Subtitle Navier-Stokes and Euler Solutions for Lee-Side Flows Over Supersonic Delta Wings *A Correlation With Experiment*		5. Report Date December 1990
		6. Performing Organization Code
7. Author(s) S. Naomi McMillin, James L. Thomas, and Earll M. Murman		8. Performing Organization Report No. L-16751
9. Performing Organization Name and Address NASA Langley Research Center Hampton, VA 23665-5225		10. Work Unit No. 505-61-71-01
		11. Contract or Grant No.
12. Sponsoring Agency Name and Address National Aeronautics and Space Administration Washington, DC 20546-0001		13. Type of Report and Period Covered Technical Paper
		14. Sponsoring Agency Code

15. Supplementary Notes

S. Naomi McMillin and James L. Thomas: Langley Research Center, Hampton, Virginia.
Earll M. Murman: Massachusetts Institute of Technology, Cambridge, Massachusetts.

16. Abstract

An Euler flow solver and a thin-layer Navier-Stokes flow solver have been used to numerically simulate the supersonic experimentally observed lee-side flow fields over delta wings. Three delta wings with 75°, 67.5°, and 60° leading-edge sweeps were computed over an angle-of-attack range of 4° to 20° at a Mach number of 2.8. The Euler code and Navier-Stokes code predict equally well the primary flow structure where the flow is expected to be separated or attached at the leading edge based on the Stanbrook-Squire boundary. The Navier-Stokes code is also capable of predicting the secondary flow features. For those flow conditions where the Euler code did not predict the correct type of primary flow structure, the Navier-Stokes code illustrated that the flow structure is sensitive to boundary-layer model. In general, the laminar Navier-Stokes solutions agreed better with the experimental data, especially for the lower sweep delta wings. The computational results and a detailed reexamination of the experimental data resulted in a refinement of the flow classifications with the separation bubble with the shock flow field as the intermediate flow pattern between separated and attached flows.

17. Key Words (Suggested by Authors(s)) Conical and three-dimensional Navier-Stokes solutions Conical Euler solution Supersonic delta wings Vortical flows Lee-side flows Shock-induced separation	18. Distribution Statement Unclassified—Unlimited Subject Category 02	
19. Security Classif. (of this report) Unclassified	20. Security Classif. (of this page) Unclassified	21. No. of Pages 102	22. Price A06